This article was downloaded by:[Northwestern University]
On: 15 October 2007
Access Details: [subscription number 764700504]
Publisher: Taylor & Francis
Informa Ltd Registered in England and Wales Registered Number: 1072954
Registered office: Mortimer House, 37-41 Mortimer Street, London W1T 3JH, UK

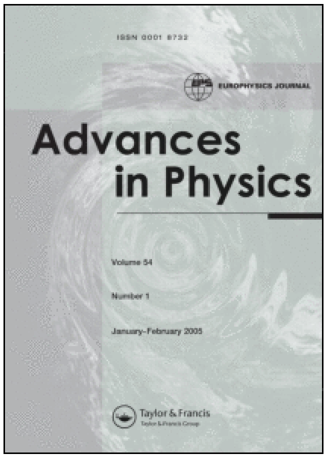

Advances in Physics

Publication details, including instructions for authors and subscription information:
http://www.informaworld.com/smpp/title~content=t713736250

A dynamical systems approach to mixing and segregation of granular materials in tumblers

Steven W. Meier [a]; Richard M. Lueptow [b]; Julio M. Ottino [ab]
[a] Department of Chemical and Biological Engineering, Northwestern University, Evanston, Illinois 60208, USA
[b] Department of Mechanical Engineering, Northwestern University, Evanston, Illinois 60208, USA

Online Publication Date: 01 September 2007
To cite this Article: Meier, Steven W., Lueptow, Richard M. and Ottino, Julio M. (2007) 'A dynamical systems approach to mixing and segregation of granular materials in tumblers', Advances in Physics, 56:5, 757 - 827
To link to this article: DOI: 10.1080/00018730701611677
URL: http://dx.doi.org/10.1080/00018730701611677

PLEASE SCROLL DOWN FOR ARTICLE

Full terms and conditions of use: http://www.informaworld.com/terms-and-conditions-of-access.pdf

This article maybe used for research, teaching and private study purposes. Any substantial or systematic reproduction, re-distribution, re-selling, loan or sub-licensing, systematic supply or distribution in any form to anyone is expressly forbidden.

The publisher does not give any warranty express or implied or make any representation that the contents will be complete or accurate or up to date. The accuracy of any instructions, formulae and drug doses should be independently verified with primary sources. The publisher shall not be liable for any loss, actions, claims, proceedings, demand or costs or damages whatsoever or howsoever caused arising directly or indirectly in connection with or arising out of the use of this material.

Advances in Physics,
Vol. 56, No. 5, September–October 2007, 757–827

A dynamical systems approach to mixing and segregation of granular materials in tumblers

STEVEN W. MEIER†, RICHARD M. LUEPTOW‡
and JULIO M. OTTINO*†‡

†Department of Chemical and Biological Engineering, Northwestern University, Evanston, Illinois 60208, USA
‡Department of Mechanical Engineering, Northwestern University, Evanston, Illinois 60208, USA

(*Received 23 January 2007; in final form 3 August 2007*)

The physics of granular matter is one of the big questions in science. Granular matter serves as a prototype of collective systems far from equilibrium and fundamental questions remain. At the same time, an understanding of granular matter has tremendous practical importance. Among practical problems, granular mixing and its interplay with segregation is arguably at the top of the list in terms of impact. Granular mixing in three-dimensional systems is complicated, as flow induces segregation by particle size or density. Several approaches and points of view for analysis are possible in principle, ranging from continuum to discrete. Flow and segregation in three-dimensional systems is seemingly complicated; however, to a reasonable approximation, all of the dynamics takes place in a thin flowing surface layer. This observation, coupled with key experimental results, leads to a simple, compact and extensible continuum-based dynamical systems framework applicable to time-periodic flow in quasi-two-dimensional tumblers and three-dimensional systems (such as spheres and cubes) rotated about one or more axes of rotation. The case of time-periodic systems, in its simplest version, can be viewed as a mapping of a domain into itself. The placement of periodic points can be investigated using symmetry concepts; the character of the periodic points and associated manifolds provides a skeleton for the flow and a template for segregation processes occurring in the flow.

Keywords: Chaos; Granular matter; Mixing; Segregation; Dynamical systems; Granular flow

Contents

---

*Corresponding author. Email: jm-ottino@northwestern.edu

Advances in Physics
ISSN 0001–8732 print/ISSN 1460–6976 online
http://www.tandf.co.uk/journals
DOI: 10.1080/00018730701611677

1. Introduction

The 125th anniversary issue of *Science* identified the flow of granular material as the subject of one of the 125 big questions in science [1]. Granular flows are important in many disciplines ranging from the planetary sciences to geophysics to industrial processing. Geological features on Mars [2–4], Io (one of Jupiter's moons) [5] and the asteroid Eros [6] appear to be the result of granular flow. In geophysics, avalanches and mudslides are a common natural hazard that result in costly damage to property and loss of life [7]. In industry, the processing of ores and polymers, pharmaceutical manufacturing and many aspects of food processing depend on understanding, often gained after years of laborious trial and error experimentation, of the behaviour of granular flows [8].

Granular matter, and granular flow in particular, is an example of a collective system far from equilibrium [9–13]. Granular matter may be considered one of the simplest examples of a complex system, that is a system composed of many individual parts where the study of a single element, in this case a particle, and how it interacts with another particle does not provide insight into macroscale behaviour, such as the segregation patterns that appear in systems composed of two different types of granular particles.

The mixing and segregation of granular matter is so pervasive in industry and natural processes that one would think that a suitable theoretical framework would have been developed long ago. However, in comparison with the mixing of liquids, the flow and mixing of granular materials is poorly understood and such a framework is lacking at the present time [14]. An important complicating factor is the tendency for materials to segregate as a result of differences in particle properties, such as density or size [15–29]. Processes intended to cause mixing of material actually may cause granular material to completely separate or 'demix' because of particle properties. It appears, however, that there is a sufficient body of experimental and computational modelling results so that a framework is emerging.

1.1. *Organization*

The focus of this article is a continuum framework for granular flow that can be used to examine granular mixing and how it competes with segregation in surface-dominated flows generated in partially filled containers rotated in one or more directions in combinations of steady and time-varying modes. In section 1, we consider first a few of the salient aspects of continuum descriptions before moving into the definition of terms that serve to specify the systems covered. In terms of the *interstitial medium*, we consider *dry granular systems* (DGSs) and *liquid granular systems* (LGSs); in terms of the polydispersity of the *particles* themselves we consider D-systems (where particles vary in density) and S-systems (where particles vary in size). We next consider the *containers* in which the granular matter is housed, *flow regimes* and *modes of operation*, where we define the dimensionality of the granular flow: 2d (two-dimensional) and 3d (three-dimensional). (A brief remark about notation is warranted here. Upper case D refers to density as in D-systems and appears also describes a medium as in DGS. Dimensionality is denoted by lower case d as in 2d, two-dimensional.) The section ends with a discussion of modelling approaches and a note on what kinds of systems fall outside the scope of this review. We then move into the common modes of segregation such as radial segregation in quasi-2d systems and axial segregation in long rotating cylinders. All of this constitutes a long preface to argue for the benefits of continuum models to frame and model problems involving competition between mixing and segregation. In section 2, we cover experimental results that are essential to set up the theoretical framework. We review results for the variation of the velocity profile with depth in the flowing layer and the dependence of the surface layer velocity on the length of the layer in 3d systems as well as flow–wall effects. This is followed by details of the 2d continuum model and visualization of flow structure in terms of Poincaré sections in time-periodic flows in section 3. The presentation then focuses, in section 4, on constitutive models for segregation, an interpenetrating continua model involving flow, diffusion and segregation, and implementation details, followed by applications to various systems. The continuum model is extended to 3d systems in section 5, while section 6 is devoted to dynamical systems tools that serve to identify the placement of key flow structures in 3d geometries when subjected to a succession of time-periodic actions. The article concludes with several examples of the application of the framework and a summary of open problems and areas for further study, such as coarsening problems in two dimensions.

1.2. *Granular matter and the continuum viewpoint*

Granular matter seems tailor-made for discrete viewpoint descriptions, from idealized cellular automata (CA) calculations to detailed particle dynamics (PD) simulations. However, as we argue, continuum descriptions are remarkably useful as well. PD methods come close to the ideal of a first-principles bottom-up approach. The motion of each particle is governed by Newton's laws; the goal is to compute the evolution of linear and angular momentum of every particle by using appropriate contact force models; macroscopic behaviour emerges by averaging over a large number of particles. Recent simulations are capable of handling as many particles as an actual, albeit small-scale, experiment, 10^4–10^5 or so, and progress in this area will undoubtedly continue. Such a degree of faithfulness comes at a price. Although 'exact' in principle, PD simulations require considerable thought in the choice of contact force models and precise physical properties (Young's modulus, restitution coefficients, Poisson's ratio, etc.). Thus, the result of a single simulation is as specific as a single experiment: prediction is gained, but understanding is not assured.

At the other extreme we have continuum descriptions. There is a rich tradition of applying continuum-like descriptions to granular flows. In fact, granular flows have been used as the starting point of manifestly discrete problems such as traffic flows [30]. There are, however, several obstacles for the appropriateness of using a continuum description to describe granular flows [12]. One is the relevance of intermediate scales (mesoscales) as manifested in jamming and stress chains. Nevertheless, there is now emerging evidence that continuum-based descriptions, with constitutive relations derived either from first-principles or supported by particle dynamics simulations, may form the basis of a general expandable and coherent framework for the description of a variety of flow phenomena of granular materials. As we demonstrate in this article, a simple continuum description provides a relatively self-contained framework, much like those in specialized branches of fluid mechanics, that allows for the modelling of competing processes of mixing and segregation.

Two extremes, the quasi-static regime and the rapid granular flow regime, have been studied the most. The quasi-static regime is dominated by frictional stresses, where each particle has long enduring contacts with multiple particles [31–33]. This regime is the subject of the well-established field of soil mechanics and has been applied to processing problems such as hopper flows [33] and, more recently, pebble-bed nuclear reactors [34]. Janssen's analysis of pressure in a silo is an early example of the continuum view of quasi-static granular material (see [20, 35–37]). At the other end of the spectrum are rapid granular flows where particles only interact through brief binary collisions much like the behaviour of molecules in gases [31, 38, 39]. Studies in this area of 'dilute granular gases' have benefited from analogies with the kinetic theory of gases [31, 38, 39]. In between the extremes of quasi-static flows and rapid flows is a broad range of flows. In this review, we consider situations where a portion of the granular matter flows in a fluid-like manner [31]. In these systems, the particle number density is much higher than that in a granular gas. Particles may have multiple simultaneous contacts, but the collisions are short in duration, so the dynamics are closer to that observed in the granular gas state than that of the quasi-static regime.

The continuum approach is appropriate for standard fluid mechanics because the length scale of flows is typically much larger than the characteristic dimension of the molecules and mean free paths [40–43]. Properties such as density, concentration and velocity can be assigned to a point, field descriptions are appropriate, gradients can be computed and so on. Transport properties can be calculated, often based on statistical mechanics, and the separation of length and time scales makes it possible to feed these parameters into continuum descriptions of flows. This area is one of the most evolved in physics and a sophisticated mathematical machinery has been developed to deal with various specific regimes in fluid dynamics, such as slow interialess flows, frictionless flows and so on.

The application of the continuum viewpoint to granular materials is difficult because the relevant length scales are not immediately obvious [11, 43]. The ratio of the system size to particle size in granular flows is much smaller than the ratio of system size to molecular size in a typical fluid system, and for this reason the average values of properties of granular flows are 'lumpy' compared to the average values of properties of fluids [44]. However, when one considers properties that depend on particle-particle interactions, granular flows have an advantage over fluid systems. Molecule-molecule interactions in fluids are elastic, whereas particle-particle collisions in granular flows are inelastic. Because of inelasticity, the length scale of energy transport in granular materials does not extend beyond a few particle diameters [44], and changes in macroscopic quantities related to energy transport then occur over short distances. Thus, in the sense of properties due to particle-particle interactions, granular materials may be more suited for a continuum viewpoint than actual fluids such as gases and liquids. A possible difficulty is the presence of singularities such as shocks, an area that is well treated in standard fluid mechanics but less so in continuum descriptions of granular flows.

Haff [44] developed an early version of a continuum description for rapid granular flows and used the framework to work out simple prototype problems.

The continuum viewpoint for rapid granular flows has also been derived from microscopic models of individual particle collisions patterned in analogy with the kinetic theory of gases [31, 37, 38, 45]. One important concept resulting from this analogy is granular temperature, defined as the mean square value of the random fluctuation velocities about the mean velocity in a granular flow [46]. It is important to note that the granular temperature is superficially analogous to, but clearly different from, the thermodynamic temperature. When the driving force stops for a granular system, the granular temperature rapidly goes to zero as energy is dissipated due to friction and inelastic collisions.

A set of Navier–Stokes-like continuum equations can be derived based on the analogy with the kinetic theory of gases assuming that particles interact only through binary instantaneous collisions [31, 38, 47]. This is different from standard kinetic theory in that the energy equation accounts for dissipation. Constitutive relationships for stresses range from heuristic-inspired models to those based on sophisticated theory. An early constitutive relationship for the shear stress was first determined from experiment and dimensional analysis by Bagnold [48]. The stress due to interparticle collisions, τ_{c}, scales as $\rho_{\mathrm{p}} d_{\mathrm{p}}^2 \dot{\gamma}^2$, where ρ_{p} is the density of the particles, d_{p} is the diameter of the particles and $\dot{\gamma}$ is the shear rate. This scaling has been confirmed experimentally and computationally [38], although some details of Bagnold's experiment have recently been challenged [49]. In low-density granular gas systems, the Bagnold stress dominates the total stress contribution. However, Savage [47] points out that at higher densities with a large number of collisions, Coulombic frictional stresses (typically associated with the quasi-static regime) have a significant role as well. How to account for the relative contributions of frictional and collisional stresses in the intermediate regime of granular flows has been an active area of research [50–54]. One successful constitutive law for granular flow is based on a visco-plastic approach in which the shear stress is proportional to the normal stress through a friction law with rheological parameters based on experiments [51, 55]. Using this relation for the internal stress in the standard Navier–Stokes equations for a fluid, reasonable quantitative agreement can be achieved for the velocity and flowing layer depth of a granular heap flow in a channel [51]. Another area of active interest is in continuum models of avalanching flows. A model for thin avalanches was developed by Bouchaud *et al.* [56, 57]. This work was further modified by Boutreux *et al.* [58, 59] to account for thick avalanches. Recently, an order parameter method has been proposed to describe the transition between flowing and static granular material, such as in an avalanche [60–63].

In this work, we discuss the modelling of mixing and segregation of granular materials in rotating tumblers using a continuum dynamical systems framework built on a few basic assumptions. The fluid-like portion of the flows considered here are dense (but not jammed) and continuous. The continuum viewpoint used here includes both collisional and frictional stresses, as suggested above for intermediate regime granular flows. The primary interest is in flows in 3d geometries.

1.3. *Objectives and definitions*

The objective of this article is to present a summary of tools and results that lead to a self-contained description of granular mixing and segregation processes in surface-dominated flows, in particular in 3d systems. The problem can be simplified by noting that all of the important dynamics occur in a thin, rapidly flowing surface layer. This layer exchanges particles with a bed of particles in essentially solid body rotation with the tumbler. (There is, in fact, creeping motion in the bed near the interface with the flowing layer [64, 65] that we take to be negligible in comparison with the motion in the flowing layer.) An understanding of the dynamics of the layer (how it scales with tumbler geometry, particle size and type and rotation rate) leads to a complete, albeit simplified, description of the system.

1.3.1. Specification of mixture. We consider two classes of mixtures of particles (binary systems, unless indicated otherwise): S-systems, where particles vary by size but not density; and D-systems, where particles vary by density and not size. In practice there may be SD-systems, where particles differ in both size and density [66, 67]. Moreover, systems need not be binary (denoted as S_2 or D_2), consisting of only two classes of sizes or densities, but ternary (denoted S_3 and D_3) or even continuously distributed (denoted $S_{f(S)}$ and $D_{g(D)}$). Systems may be $SD_{f(S,D)}$, with particles varying in both size and density according to a distribution represented by $f(S, D)$.

1.3.2. Interstitial medium. We consider two classes of two-phase systems in the spectrum of possible three-phase systems shown in figure 1: DGSs and LGSs. In DGSs, the particles are surrounded by a gas such as air or are under vacuum.

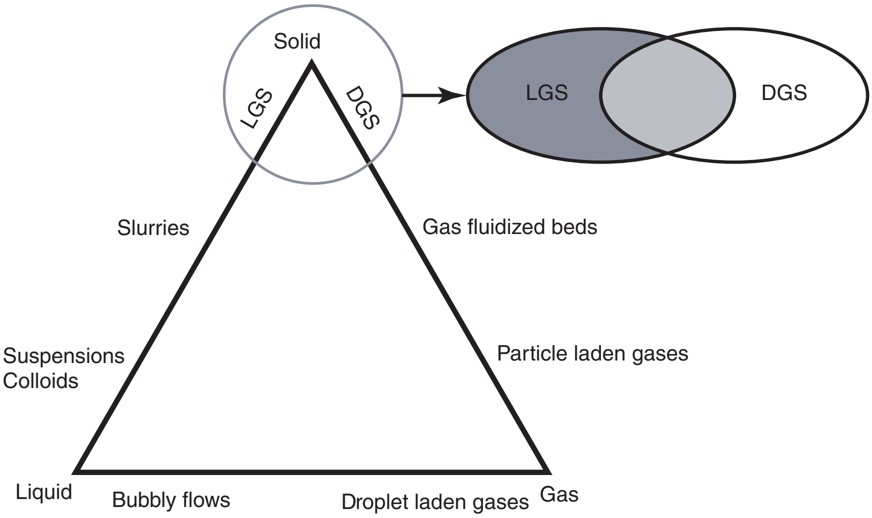

Figure 1. The types of two-phase granular systems of interest, DGSs and LGSs, in the spectrum of possible three-phase systems: DGSs consist of particles and a gas; LGSs consist of particles and a liquid. The particle size does not appear in this diagram, but it is crucially important to the relevant physics. The inset illustrates the region of overlap in the dynamics of LGSs and DGSs. The set denoted LGS represents all of the dynamical outcomes of experiments using LGSs; likewise the set DGS represents all of the dynamical outcomes of experiments using DGSs. The framework outlined in this article applies to cases for which the dynamical outputs of experiments using LGSs and DGSs are virtually undistinguishable.

In principle, lubrication forces play a role when a fluid is present, and this would suggest differences in the behaviour of systems when the interstitial fluid is air or a liquid (water). In practice, however, lubrication effects only become noticeable at length scales below the typical roughness of particles, so frictional effects dominate. Thus, when the particle size is $O(1\,\mathrm{mm})$ or larger, the physics in DGSs depend almost entirely on particle contacts, not on the gas surrounding the particles, unlike fluidized beds or particle-laden gases where particles are in contact with each other only infrequently. In LGSs the interstitial fluid is a liquid. When particles $O(1\,\mathrm{mm})$ or larger are fully immersed in a less-dense liquid (there is no gas phase), the physics are also dominated by particle contacts just as in DGSs, unlike slurries where the particles and liquid flow together or suspensions and colloids [68] where interparticle contact is infrequent. Physics that apply to both LGSs and DGSs are also discussed by Rajchenbach [69].

The Bagnold number provides a framework for determining whether the physics of a granular flow are dominated by particle collisions or fluid properties. The Bagnold number is defined as the ratio of stresses due to particle–particle collisions [48] to stresses due to lubrication forces of the interstitial fluid [70, 71]. When the Bagnold number is large, particle collisions dominate over lubrication.

When a small amount of liquid is mixed with a DGS resulting in a three-phase system, cohesion between particles due to surface tension becomes important [32, 72–74]. These are commonly referred to as ‘wet’ systems and are located in the middle region of the three-phase diagram in figure 1. ‘Wet’ systems have been the subject of reviews by Herminghaus [32] and Mitarai and Nori [72]. The physics of DGSs of fine powders (particle size $O(1\,\mu\mathrm{m})$ or smaller) also involve cohesive forces, in this case due to van der Waals attraction, as discussed in a review by Castellanos [75]. In general, the physics of cohesive systems can be characterized by the Bond number, the ratio of attractive interparticle forces to inertial forces [75].

Since LGSs and DGSs are dominated by particle contacts there is a broad region of operating space where they have nearly identical dynamical responses, shown schematically in the inset of figure 1 and, jumping ahead, by results, such as those in figure 20. At this point we should mention that studies of mixing and segregation in LGSs offer experimental advantages over DGSs in terms of being able to control the experiment and interpret the results. Humidity, electrostatic charging of particles and abrasion, problems that plague even the simplest experiments with DGSs, play little or no role in LGSs. Consider further that with suitable index-matched fluids and proper illumination one can visualize the interior of a granular bed [76] without recourse to expensive magnetic resonance imaging (MRI) [77–81] or X-ray instrumentation [82]. Also, owing to the immersion of the granular material in a liquid, cohesion forces due to moisture play no role and surface forces play less of a role [32, 72]. Moreover, one can control the role of body forces in LGSs by means of buoyancy. However, DGS experiments are more common because their setup is less complicated.

1.3.3. Systems used to generate motion. Granular flows can be classified into several canonical flow systems. The Groupement de Recherche Milieux Divisés (GDR MiDi) proposes six basic configurations of granular flows in two categories [83]. Confined flows include plane shear, annular shear and vertical chute flows.

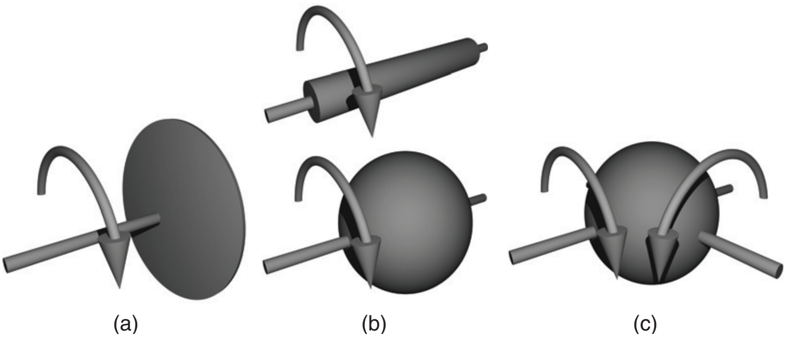

Figure 2. Classification of free surface flow granular systems in rotating tumblers: (a) quasi-2d; (b) 2d + 1; (c) 3d.

Surface flows include inclined plane flow, heap flow and flows in rotating drums. In this review, we discuss only surface flows, primarily those in rotating drums or tumblers, although many of the concepts described here can be extended beyond tumbling flows.

We consider three types of systems that can be used to generate surface flows in rotating tumblers, as shown in figure 2. Situations in which the tumbler thickness is only a few particle diameters, such as a cylinder with a diameter much larger than its axial thickness (figure 2(a)), are known as quasi-2d flows. This is a commonly studied system [18, 19, 84–91] because of the ease with which the flow can be measured or observed through a clear end wall, the simple tumbler drive mechanism and the relatively small volume of granular material required. The dimension in the axial direction is critical: too thin a tumbler results in ordered layering of monodisperse granular material [92] or crystallization [22, 93]; too wide results in the 2d + 1 case (figure 2(b)).

Flows in 3d tumblers (where the axial dimension is the same order or larger than the radial dimension [94]), such as long cylinders or spheres (figure 2(b)), are essentially 2d when the orientation of the instantaneous axis of rotation does not change. The flow in a 2d disc-like slice perpendicular to the axis of rotation at one axial position is similar in character to that at other axial positions. However, these systems need an additional spatial parameter to account for the position and variation of the 2d slices along the axis of rotation. For instance, in a spherical container, the flow in the circular disc-like slices is similar from one slice to another, but the radius of the slice varies with axial position. These cases are denoted 2d + 1 to indicate two coordinates and one parameter (or primarily 2d plus the additional axial dimension).

When all three dimensions are required to fully describe the flow, such as when there are two axes of rotation operated so that the orientation of the instantaneous axis of rotation changes in time, the flow is 3d (figure 2(c)). An example is when the axes are operated out of phase with each other (for instance, when there is rotation about one axis followed by rotation about the other axis).

1.3.4. Flow regimes. For surface flows in tumblers, the flow can be categorized as avalanching, rolling, cataracting or centrifuging [21], although variations in the classification scheme and naming conventions have been suggested [93, 95, 96]. Which flow regime occurs depends on the Froude number, the ratio of inertial forces to the gravitational force, $\mathrm{Fr} = \omega^2 R/g$, where ω is the rotational speed of the tumbler, R is the radius of the tumbler and g is the acceleration due to gravity [21]. Typically the Froude number is changed by varying the tumbler radius, R, or the rotation rate, ω. However, recent work has shown that the Froude number also characterizes the flow when g is varied [97]. The nature of various flow regimes and their dependence on the Froude number has been documented in detail [93, 95–97].

Figure 3 shows a circular cross section orthogonal to the axis of rotation of a tumbler operated in the four flow regimes. Figure 3(a) depicts the avalanching regime (also referred to as slumping [96]), which corresponds to approximately $\mathrm{Fr} < 10^{-5}$ in DGSs [97]. However, this regime has also been observed up to $\mathrm{Fr} = 10^{-3}$ depending on factors such as the fill fraction, particle friction coefficients and particle to tumbler size ratios [96]. The avalanching regime is characterized by intermittent avalanches of granular material at the surface. The granular material rotates as a solid body with the tumbler until it reaches the angle of marginal stability, β_m. At this angle, an avalanche occurs until the material settles at the static angle of repose, β_s. As described earlier, avalanche flows have been studied with continuum models [56–63]. However, mixing in avalanche flows in tumblers is typically studied computationally through the use of discrete models such as the wedge model [98, 99] and CA [100–105].

Figure 3(b) illustrates the rolling or continuous-flow regime, which corresponds to approximately $10^{-4} < \mathrm{Fr} < 10^{-2}$ in DGSs [95–97]. This is the flow regime considered in this review. It is characterized by a thin, rapidly flowing, flat surface layer that flows at an angle with respect to the horizontal, the dynamic angle of repose, β_d [20–22, 77, 93, 95], which is a function of particle properties including size [91] and surface roughness [106] as well as tumbler properties such as dimensions, end-wall effects [91, 107] and rotation rate [91, 93, 108, 109]. Particles enter this flowing layer on the upstream end from the fixed bed, which is in solid body rotation with the tumbler. Particles exit the layer on the downstream end of the layer, returning to the bed of solid body rotation. As the rotation rate is increased, the free surface becomes slightly 's'-shaped giving rise to what is sometimes referred to as the cascading regime in the range of $10^{-3} < \mathrm{Fr} < 10^{-1}$ for DGSs [96]. We include the cascading flow in the

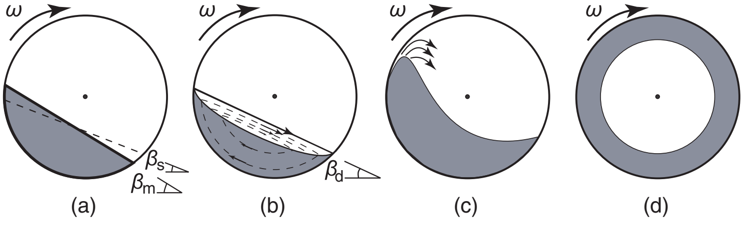

Figure 3. Illustration of flow regimes in tumblers: (a) avalanching; (b) rolling/continuous-flow/cascading; (c) cataracting; (d) centrifuging.

rolling regime category because the surface curvature is small and particles do not lose contact with one another. As Fr increases, the curvature of the surface becomes significant. For $\mathrm{Fr} > 10^{-1}$ but less than 1 in DGSs, the cataracting regime occurs [96]. Particles detach from the bed at the uphill side of the free surface and are thrown into the interstitial fluid medium inside the tumbler [21, 96], as shown schematically in figure 3(c). For $\mathrm{Fr} \geq 1$ in DGSs, the flow is centrifuging as shown in figure 3(d). In this regime, the granular material is centrifuged to the outer boundary of the tumbler and it remains in solid body rotation with the tumbler.

For flow regimes in LGSs, buoyancy forces may alter the range of Froude numbers for each flow regime. This is because the effect of the gravitational force is proportional to the density difference between the particles and the interstitial fluid. A Froude number for LGSs that could account for buoyancy is $\omega^2 R\rho_\mathrm{p}/g(\rho_\mathrm{p} - \rho_\mathrm{f})$, where ρ_p is the density of the particles and ρ_f is the density of the interstitial fluid. However, to our knowledge, this has not been considered. Klein and White proposed a different dimensionless parameter, $\mathrm{G} = g[(\rho_\mathrm{p} - \rho)/\mu\omega^3]^{1/2}$, where μ is the viscosity of the interstitial fluid, that incorporates fluid properties [110]. However, this number does not take into account the tumbler dimensions, which clearly play a role. The particle size or shape and the ratio of particle size to the tumbler dimensions also play roles in the specific Froude number for transition between flow regimes [95, 96]. For instance, the dynamic angle of repose, the static angle of repose and the angle of marginal stability depend on particle properties such as roughness [106] and shape [104]. As a result, the Froude number for transition from avalanching to rolling flow depends to some extent on size and type of particle [95, 96]. The extent to which the tumbler is filled with particles, or fill fraction, also affects the flow transition [96].

1.3.5. Time-periodic flow. Flows may also depend on time as a parameter. One example is a half-full time-periodically rotated quasi-2d circular cylinder. The rotation rate can be expressed mathematically as $\omega(t) = \omega(t + T)$ (figure 4(a)), where T is the period. The notation for this situation is 2d + T. The 2d indicates that the system used to generate the flow is quasi-two-dimensional, and the T indicates that the flow is time periodic. Since the velocity in the flowing layer depends on the rotation rate, the velocity is time periodic with period T.

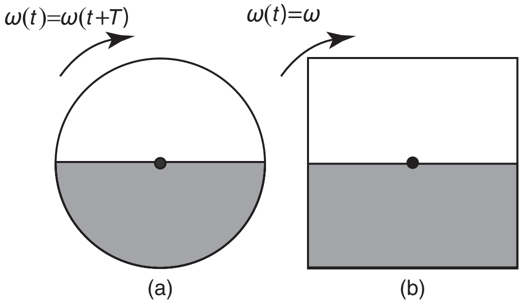

Figure 4. (a) Time-periodic rotation of a quasi-2d tumbler with a circular cross section. (b) Constant rotation of a quasi-2d tumbler with a square cross section.

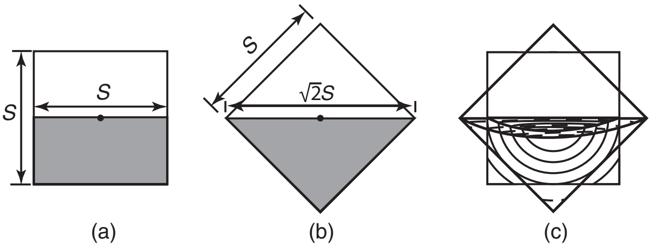

Figure 5. Half-full square. (a) The flowing layer length is at a minimum when it is parallel to a tumbler wall. (b) The flowing layer length is at a maximum when it is along the diagonal. (c) The time-periodic orientation of the tumbler and flowing layer results in the intersection of the streamlines in the flowing layer for the two different orientations.

2d + T flow can also occur in a polygonal tumbler, for example a half-full quasi-2d tumbler with a square cross-section rotated at a constant rate, ω (figure 4(b)). Here time is introduced as a parameter through the time-periodic orientation of the tumbler geometry. In the case of the tumbler with a square cross section, the flowing layer length is at a minimum when the free surface of the flowing layer is parallel to a tumbler wall (when the tumbler is in the square orientation shown in figure 5(a)). The flowing layer length is at its maximum when the flowing layer is along the diagonal (the tumbler is in the diamond configuration shown in figure 5(b)) [19]. As shown later, the velocity in the flowing layer is directly proportional to the length of the flowing layer. The flow field is then time periodic reaching a maximum every time the flow is along the diagonal of the square, which corresponds to every one-quarter revolution. It can also be shown that the streamlines computed for the two orientations intersect, as shown in figure 5(c), which is required for chaotic advection in 2d + T flows [88]. Clearly all non-circular tumbler geometries (ellipses, triangles, pentagons, etc.) generate similar periodicity [111]. A combination of time-periodic rotation and non-circular geometry is also possible.

Similar to the quasi-2d case, long circular cylinders can be rotated time periodically. This type of system is denoted by 2d + 1 + T where the ‘one’ indicates a spatial parameter, the dimension along the axis of rotation (the transverse direction). Another 2d + 1 + T system would be a long cylinder with a square cross section rotated at a constant rotation rate.

When multiple axes of rotation are used, as shown in figure 6, the flow can become 3d + T. Consider, for example, flow in a half-full spherical tumbler rotated about two axes of rotation (orthogonal to each other intersecting at the centre of the sphere), as shown in figure 6(a). The rotation rate for the x_1-axis is given by $\omega_1(t) = \omega_1(t + T_1)$, where T_1 is the period. The rotation rate could be sinusoidal, saw-tooth or stepwise in time. The rotation rate for the x_3-axis is $\omega_3(t) = \omega_3(t + T_3)$ where T_3 is the period. As shown in figure 6, the rotation around the x_1-axis is counterclockwise and the rotation around the x_3-axis is clockwise ($\omega_1 > 0$ and $\omega_3 < 0$). An example of 3d + T flow is the two-axis protocol (sometimes referred to as the biaxial protocol [112]) in which the rotation rates on the x_1- and x_3-axes are stepwise. First, the tumbler rotates about the x_1-axis for a period of time. Next, the tumbler rotates about the x_3-axis for a period of time. Then the process repeats.

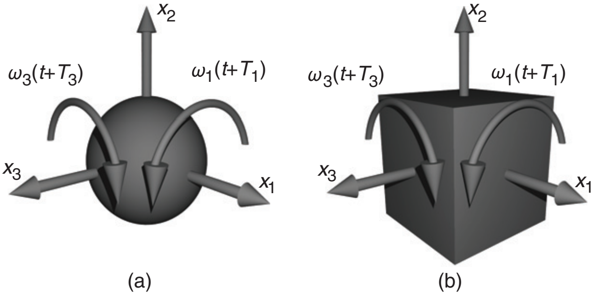

Figure 6. (a) Time-periodic operation of a spherical tumbler on two axes, x_1 and x_3. (b) Time-periodic operation of a cubical tumbler. In both (a) and (b), gravity is along x_2.

The flow is 3d + T when $\omega_1(t) \neq k\omega_3(t)$ for all t, where k is a constant and at least one rotation rate is time periodic while the other is constant or time periodic. If $\omega_1(t) = k\omega_3(t)$, then the flow is 2d + 1 when the rotation rates are constant, and it is 2d + 1+T when the rotation rates are time periodic. For these cases, the instantaneous axis of rotation is invariant with respect to the direction of gravity. Finally, the flow can be 3d and not time periodic if $\omega_1(t) \neq k\omega_3(t)$ and the rotation rate on at least one of the axes of rotation is neither constant nor time periodic (for example, a randomly varying rotation rate).

In 3d + T flows, the tumbler geometry can also introduce additional time periodicity in the same way tumbler geometry affects 2d + T flows, as shown in figures 4(b) and 5. A simple example of a 3d + T flow with a tumbler geometry that induces time-periodicity to the flow is illustrated in figure 6(b). In this case, there are two time scales for time periodicity, one due to the time-periodic rotation about the axes and the other due to the rotational orientation of the tumbler.

1.3.6. The connected flowing layer. The continuum framework outlined in this article is applicable to flows in the rolling or continuous-flow regime when the flowing layer is connected. Two aspects are important, as shown in figure 7(a): (1) the 2d slice or plane of cross-sectional flow; and (2) the flow surface itself. First, we restrict our attention to containers for which the plane of cross-sectional flow is convex (spheres, ellipsoids, cubes, double cones, etc.). A general example is illustrated in figure 7(b). A tumbler cross section is convex when a line between any two points at the boundary of the tumbler is wholly contained within the tumbler. In convex containers, the free surface of the flowing layer will always be connected, regardless of the rotational orientation of the tumbler. Tumblers with dimples or baffles can sometimes be analysed using the continuum model for fill fractions that keep the free surface connected during rotation. However, we do not consider situations where the dimple or baffle is large enough so that the flowing layer is split, forming two or more disconnected simultaneous flowing layers at some point during the rotation, as illustrated by figure 7(c). Second, we consider only tumblers in which the flow surface is connected for all cross-sectional planes of flow. Thus, 3d concave tumblers may be allowed depending on the orientation of the axis of rotation. For example, a dumbbell shape is allowed if the axis of rotation is along the long axis (figure 7(d)). However, the case in figure 7(e) lies outside the present framework.

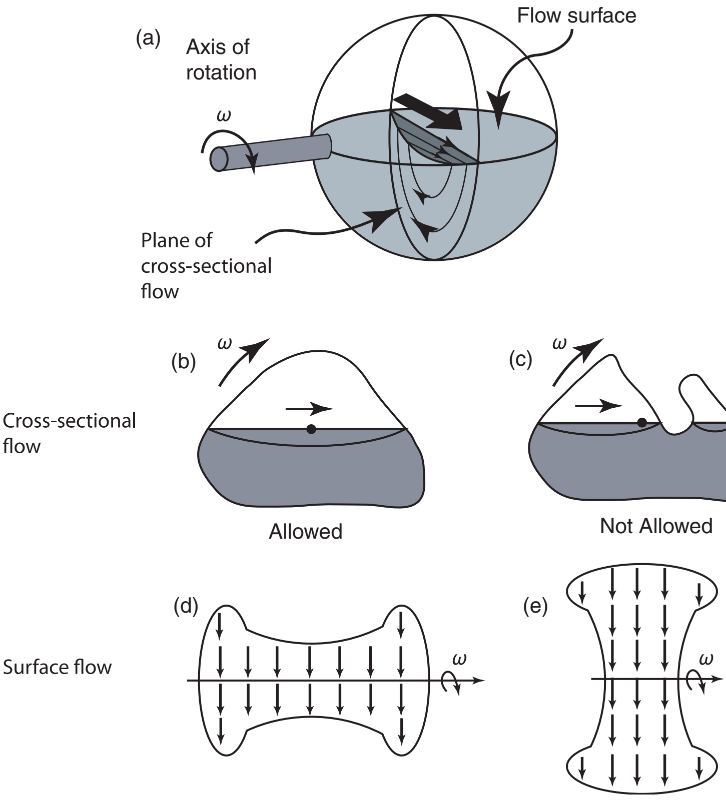

Figure 7. Two aspects of the flow are important. The 2d slice or plane of cross-sectional flow shown in (a) must be connected. Thus, the cross section in (b) is allowed. However, if it is disconnected by the tumbler geometry as shown in (c), the continuum framework as described cannot be applied. In three dimensions, the application of the continuum framework depends on the orientation of the tumbler. While the surface flow for the orientation of a concave tumbler shown from the top in (d) is allowed, the orientation shown in (e) is not allowed.

1.3.7. Coordinate systems. Two coordinate systems are needed: one to describe the motion and rotation of the container itself and the other to describe the motion of the granular material within the container. The coordinate system for the container is x_1, x_2, x_3 with rotation $\boldsymbol{\omega} = (\omega_1, \omega_2, \omega_3)$ as shown in figure 6. Here $\omega_1 > 0$ and $\omega_3 < 0$ in keeping with the convention established for quasi-2d flows [18, 19, 86, 88]. The coordinate system for the granular matter within the tumbler is x, y, z. Its origin is at the centre of the free surface of the flowing layer. This position is defined as the point halfway between the end walls in the transverse direction (parallel to the axis of rotation) and, in the direction of flow at this transverse location, halfway between the upstream and downstream tumbler walls, as shown in figure 8 for the example of a cylindrical tumbler. The position vector is $\boldsymbol{x} = (x, y, z)$ with y pointing outwards normal to the free surface. The velocity vector in the flowing layer is $\boldsymbol{u} = (u_x, u_y, u_z)$. The thickness of the thin lens-shaped flowing layer is $\delta(x, z)$. The local depth-averaged streamwise velocity in the flowing layer is given by $\bar{\boldsymbol{u}}_x(x, z) = 1/\delta(x, z) \int_{-\delta(x,z)}^{0} u_x(x, y, z)\, \mathrm{d}y$. The velocity vector in the fixed bed is $\boldsymbol{v} = (v_x, v_y, v_z)$. For the

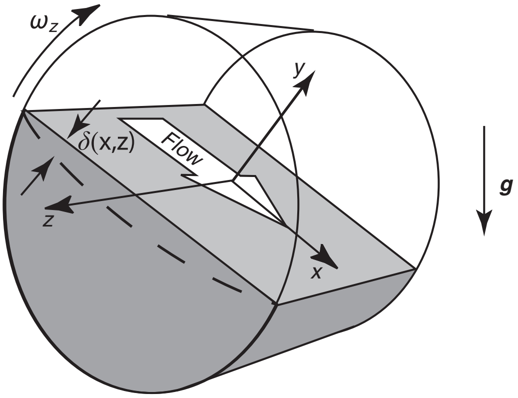

Figure 8. Illustration of the free surface coordinates in a cylindrical tumbler with its axis of rotation aligned with the z direction. Material flows on the free surface in the positive x direction when the rotation is clockwise with respect to the z-axis.

example of a half-full cylinder illustrated in figure 8, the x_3-axis for the container coincides with the z-axis for the granular flow and $\omega = (0, 0, \omega_3) = (0, 0, \omega_z)$ with $\omega_3 = \omega_z < 0$. With rotation only with respect to the z-axis, no flow occurs in the z direction, so $\boldsymbol{u} = (u_x, u_y, 0)$. The velocity in the fixed bed is then $\boldsymbol{v} = (v_x, v_y, 0)$. In most cases, we consider the simplest situation, a half-full tumbler such as that shown in figure 8. Fill fractions deviating from half full can be considered with a few caveats that are explained later.

1.3.8. Radial segregation. S- and D-systems, both LGSs and DGSs, subject to flow often segregate leading to results that on first viewing appear to be baffling. Segregation occurs in free surface flows such as those on heaps and in tumblers by the percolation of small particles through interstices between large particles (S-systems) or due to buoyancy differences between light and heavy particles (D-systems) [15, 113–121]. Consider segregation for S_2- or D_2-systems in a quasi-2d tumbler. Small or heavy particles drift downwards in the flowing layer displacing larger or lighter particles upwards. In the downstream portion of the flowing layer, the particles leave the flowing layer at the interface with the fixed bed. Since small or heavy particles have drifted to the bottom of the flowing layer by percolation or buoyancy, they leave the flowing layer first at positions relatively close to the midlength of the flowing layer. This traps the small or heavy particles in the fixed bed near the middle of the tumbler. Large or light particles that have drifted upwards in the flowing layer travel further towards the periphery of the tumbler before entering the fixed bed. Thus, they end up closer to the periphery of the tumbler than the small or heavy particles. This process is amplified each time the particles pass through the flowing layer, which leads to small or heavy particles segregating near the centre with large or light particles near the periphery of the tumbler, as shown in figure 9(a). The resulting radial segregation can occur quite quickly, often in one or two tumbler rotations.

Another example of segregation in S-systems is the 'Brazil nut effect' in vibrating and shaking systems [16, 122] (named after the phenomenon where the large nuts end up at the top of a can of mixed nuts). When a mixture of large and small particles of the same density is shaken, the large particles rise to the top as the small particles percolate through the void spaces between the large particles. This phenomenon and its variations and exceptions (as density differences come to play) have generated much interest in recent years (see, for example, [24–29, 123, 124]).

Although the radial segregation pattern in figure 9(a) is typical for S_2- and D_2-systems, other segregation patterns that deviate from the classical radial core pattern are possible. For certain particle types, size and density combinations, particle-to-tumbler size ratios, fill fractions and rotation rates, radial streaks of segregated particles are observed, as shown in figure 9(b), instead of a semicircular core [19, 66, 67, 125–128]. The reason that a particular combination of parameters results in streaking rather than radial segregation is not completely clear, although it appears to be a result of different streamwise velocities in the flowing layer for different particle types. For example, if small particles flow faster than large particles, a typical case, they outrun the large particles reaching the periphery of the tumbler before they segregate to the bottom of the flowing layer. After they reach the fixed bed, the larger particles catch up with them. The process is reinforced when these particles enter the flowing layer again. For S-systems, this occurs when the tumbler is filled just above half full [19, 126, 127], as is the case in figure 9(b). Streaking has also been observed in half-full tumblers, a case for which a continuum model has been proposed [125]. Analogous segregation patterns occur in the case of heap flows of S-systems, but are related to the particle surface roughness [103, 104, 129]. 'Sharp segregation patterns' in which particles segregate into two large distinct regions are analogous to the radial core pattern in tumblers. 'Stratification patterns' in which particles segregate into layers are analogous to the streak pattern in tumblers. The sharp segregation pattern is typically observed when the large particles are as smooth or smoother than the small particles. When the large particles are rougher than the small particles, the stratification pattern is observed [103, 104, 129].

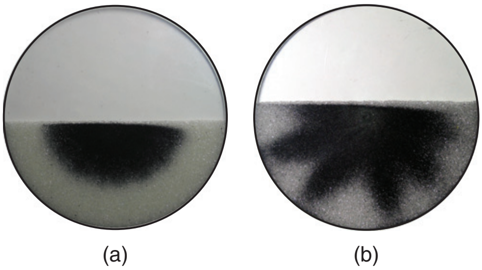
(a) (b)

Figure 9. (a) Radial core segregation for a S_2-DGS in a 48%-full quasi-2d circular tumbler. (b) Radial streaking segregation for an identical S_2-DGS in a 58%-full quasi-2d circular tumbler. In both cases, large clear glass particles are 1.11 mm. Small black painted glass particles are 0.35 mm. The tumbler is made of acrylic and has a diameter of 200 mm and a thickness of 6 mm.

Radial segregation in SD-systems can become more complicated depending on the relative size and density differences of the particles [66, 67, 78, 120, 130]. When percolation and buoyancy work together (the small particles are also the heavy ones), either a radially segregated core or radial streaks are observed, depending on the ratio of the particle sizes [66, 67]. However, when percolation and buoyancy work in opposite directions (the small particles are light), segregation can be diminished [66, 67, 120, 130]. In some cases, double segregation, a radial core of small particles with a thin layer of small particles at the periphery of the tumbler, can occur. The key factor is the ratio of the diameters and the masses of the two particle types [66]. Double segregation has also been found to occur for S-systems depending on the particle sizes, tumbler size and particle roughness [114, 120, 131].

1.3.9. Axial segregation. In $2d+1$ systems, particles of different sizes quickly segregate radially and subsequently form axial bands [132, 133] as shown in figure 10(a). The bands are generally rich in one particle type, but not necessarily pure. The bands may extend through the entire fixed bed or there can be a radial core of particles of

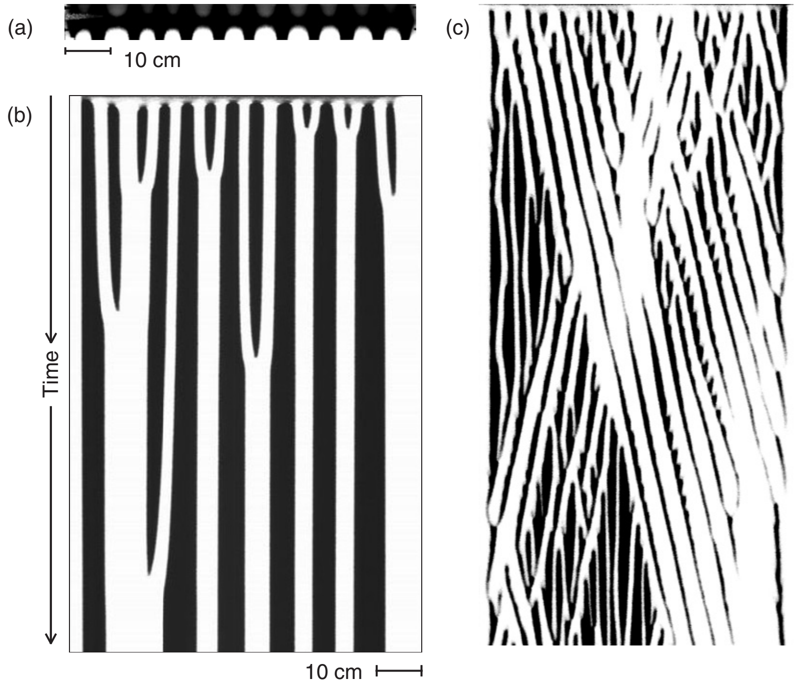

Figure 10. Axial size segregation in long cylinders. (a) Image of an experimental run cropped to coincide with the top view of the granular bed for a S_2-LGS containing a 2:1 mixture of 0.88 mm clear glass particles and 0.27 mm black painted glass particles. The acrylic tumbler has a diameter of 63.5 mm and a length of 750 mm. Small particles (dark) form a radial core running along the axis with axial bands between bands of larger particles (white and gray). (b) Space–time plot for a total of 2000 revolutions showing band dynamics including coarsening. Reprinted with permission from [143]. © 2005 American Physical Society. (c) Phenomena such as travelling waves can also be observed in space–time plots, in this case a S_2-DGS. Reprinted with permission from [142]. © 2003 American Physical Society.

the other particle type. Axial segregation occurs much more slowly than radial segregation, typically in $O(100)$ rotations of the tumbler. The formation of axial bands is puzzling and most explanations for this phenomenon are based on differences in the angles of repose of the two different particle types or of phases of mixed or pure particle types [133–135].

Hill and Kakalios showed that axial segregation is indeed a function of the difference between the dynamic angles of repose of the mixed and segregated phases [136]. The dynamic angle of repose is a function of rotation rate. When the rotation rate is set so that the segregated phases have a lower angle of repose than the mixed phase, axial segregation occurs. When the rotation rate is set so that the dynamic angles of repose are equal, axial segregation does not occur. However, the radially segregated core persists, as observed through MRI [79]. MRI measurements also show that axial variations in particle concentration persist within the bed suggesting that axial segregation is not driven exclusively by differences in the dynamic angles of repose at the free surface. In fact, differences in the dynamic angle of repose can result in an instability of the radially segregated core [137], perhaps related to inertially dominated deformation of the core due to differences in momentum between the large and small particles [138]. A proposed continuum model of axial segregation based on concentrations of the two particle types suggests that axial segregation is driven by concentration fluctuations, analogous to spinodal decomposition [139].

Often, over longer time scales, $O(1000)$ rotations, the bands coarsen as shown in the space–time plot in figure 10(b). Under other operating conditions, bands may form and then disintegrate or move along the axis of the cylinder as travelling waves [140–143], as shown in figure 10(c). Aranson *et al*. proposed a continuum model that describes both the early phase of segregation, such as travelling waves, and long-term coarsening [144, 145]. Recently, band formation and coarsening has been simulated using particle dynamics [146]. In the simulations, particle size differences alone led to axial segregation after radial segregation.

Segregation in fully 3d tumblers is only now being explored. These systems include spherical tumblers and conical tumblers operated as either 2d + 1, 3d or 3d + T. Band formation has been shown to occur under a variety of conditions in spherical tumblers [147]. Processes occurring in industrial 3d tumblers are often designed so that the granular flow is time dependent, a common case in practice, but also the least well understood. Thus, many aspects of time-dependent mixing and segregation of granular matter are being addressed [126, 127, 148–151].

1.4. *Continuum models and discrete models*

The focus of this article is a continuum framework for surface flows in tumblers, but it is important to delineate where continuum models fit into the larger picture of computational models. The most frequently studied surface flows in tumblers have been in quasi-2d circular tumblers. They have been studied computationally through both continuum-based models [18, 19, 86, 88, 111, 125, 152, 153] and through discrete models. Our current understanding of these systems has evolved from the complementary use of these two techniques [154] along with a large number of experiments. Both modelling approaches have provided insight into the nature of surface flows; however, they each have certain caveats and limitations. In some cases, continuum models are the most appropriate method of attack, while discrete models should be used in others.

At one end of the spectrum of discrete models, one can consider CA approaches in which simple rules govern the motion of particles between neighbouring cells of a grid [155]. Even though CA models do not directly model the physics of particle interaction, they have been used successfully to analyse certain aspects of granular flows in tumblers [101, 105, 156–58] including mixing and segregation.

At the other end of the discrete model spectrum, particle dynamics [74, 159–162] is the tool of choice in cases where particle–particle interactions such as cohesion are important for the description of the flow [74]. In addition to cohesive particles, particle dynamics can also be used to model the flow when other surface properties such as roughness are important [106]. For instance, simulations of axial segregation in $2d+1$ cylinders (figure 10) have been developed [146, 163–167]. In this case, particle dynamics simulations are the appropriate tools because particle properties (in this case differences in the angle of repose due to the surface roughness of large and small particles) dominate the flow.

When the flowing layer is not singly connected throughout operation of the tumbler, particle dynamics simulations may also be more appropriate than continuum models. For example, systems driven by blades and paddles do not have continuous flowing layers and, consequently, are better suited to particle dynamics simulations [168]. Other industrial tumblers such as the double-cone mixer, V-blender and tote blender have also been studied with particle dynamics simulations [169–171].

Continuum models are faster computationally than particle dynamics models. In particle dynamic simulations, processor time increases linearly with the number of particles [172]. While only several hundred particles are needed to simulate a 2d case, of the order of 100 times more particles may be needed to effectively model the 3d case. If a 2d particle dynamics simulation takes 1 day, a 3d simulation could take 100 days. As computational speed increases, this method will most likely become increasingly popular.

However, computational cost is not the only basis by which to judge the relative merits of continuum models versus particle dynamics simulations. The choice of simulation tool, continuum or discrete, is a function of the system of interest. Where long-range interactions between particles and interactions of particles with the system are important (such as an interaction with a paddle or blade), discrete methods may be best. Where particle interactions are less important, continuum models present a better opportunity for efficient study. If the goal is to study the impact of system parameters such as geometry and rotational forcing on a granular surface flow, then continuum models can provide a wealth of information.

2. Surface flow

Experiments have revealed important aspects of surface flows that can be translated into key assumptions that feed into a continuum model. From a continuum viewpoint, the flow in tumblers can be described kinematically with minimal information about the dynamics that actually create the flow. Granular systems in tumblers are dominated by surface flows, and this represents a considerable simplification. The primary assumption is that any flow in a tumbler operating in the rolling regime for either DGSs or LGSs can be divided into two distinct regions: one thin, lens-like region at the surface in which the particles flow downhill and a larger region below the flowing layer in which the particles undergo essentially solid body rotation. All mixing and segregation occurs in the thin flowing layer at the surface, and only very slow rearrangements of particles occur below the flowing layer [64, 65, 173]. Segregation based on particle type can be modelled constitutively, as discussed later. Thus, understanding the dynamics of the flowing layer leads to insight into the dynamics of mixing and segregation for the entire system. Two key aspects of the velocity in the flowing layer are needed for the continuum model: (1) the dependence of the streamwise velocity on the depth in the flowing layer and (2) the dependence of the streamwise surface velocity at the midlength of the flowing layer on the length of the flowing layer. These two aspects are described in detail below.

2.1. *Surface layer velocity: variation with depth*

Consider first the dependence of the velocity with depth in the flowing layer, which has been measured using several different techniques [77, 91]. Perhaps the most complete measurements are those of Jain *et al.* using particle tracking velocimetry (PTV) to measure the velocity profile for both DGSs and LGSs [71, 174]. They used a quasi-2d circular tumbler filled with monodisperse spherical chrome steel particles fully submerged in several different liquids as well as air. The study covered a range of Froude numbers, bead sizes, fluid densities and fluid viscosities. Figure 11 shows that, regardless of interstitial fluid, there is an approximately linear variation of streamwise velocity with depth resulting in an approximately constant shear rate in the upper three-quarters of the flowing layer. Near the bottom of the flowing layer, the velocity profile deviates from a linear profile, approaching zero

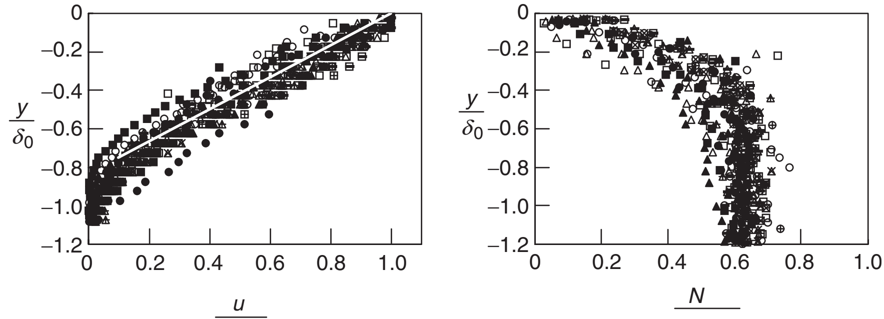

Figure 11. Left: Streamwise velocity variation with depth at $x = 0$ for 27 cases, both DGSs and LGSs. Velocity is normalized by the velocity at the free surface, u_{surf}. Right: Normalized number density profiles scaled by $N_{\text{theory}} = A/d_{\text{p}}^2$, the number of particles of diameter, d_{p} that could fit in a square bin of area A for square packing. Results for three Froude numbers (from 3.9×10^{-5} to 4.0×10^{-4}) and interstitial fluids including air, water and glycerine–water mixtures. Reprinted with permission from [71]. © 2004 Cambridge University Press.

logarithmically near the fixed bed, regardless of the interstitial fluid. We note that in the case of heap flows and inclined plane flows, in which the length of the flowing layer is not constrained like it is in a tumbler, the velocity profile follows non-linear Bagnold scaling with depth [51, 55, 83]. The linear scaling in the case of a tumbler seems to be a result of the constraint on the length of the flowing layer by the tumbler geometry.

The scaled number density for a variety of DGSs and LGSs at varying Froude numbers is approximately constant except in the upper one-third of the layer, as shown in figure 11. The surprising similarity in the dynamics of DGSs and LGSs indicates that the physics of the flow is not strongly altered by the interstitial fluid, even though the Bagnold number is 100 times larger for DGSs than LGSs [71]. Thus, the overlap region between the two systems shown schematically in the inset of figure 1 is quite large in the case of tumbled systems.

2.2. *Surface layer velocity: variation with flowing layer length*

The second aspect of the surface layer velocity involves the dependence of the velocity in the flowing layer on the tumbler geometry. To examine this, the streamwise surface velocity at the midlength of the flowing layer ($x = 0$), u_{surf}, was measured for several 3d tumblers [175] including the traditional cylindrical tumbler geometry, a double cone tumbler and a spherical tumbler [175], shown schematically on the left-hand side of figure 12. This amounts to carrying out experiments at several tumbler radii simultaneously. Each slice along the axial coordinate has a different flowing layer length $2L$.

Figure 12 shows that u_{surf} depends directly on the local flowing layer length for each tumbler cross section. In the cylinder, u_{surf} is constant with axial position with the exception of regions a few particle diameters away from the end wall, where there is a slight increase in velocity to compensate for slow flow regions due to frictional contact at the end wall [94]. This is different from heap flow in channels where the side-wall boundary flow thickness continually grows along the length of the channel resulting in the maximum velocity at its centre [51, 55]. In contrast, in rotating cylinders, the end-wall boundary flow is continuously reset at the beginning and end of the flowing layer as particles enter and exit it, localizing the impact of friction at the end walls and resulting in a nearly uniform surface velocity along most of the axial length of the cylinder when the axial length of the cylindrical tumbler is larger than the flowing layer length [94].

In a double cone, u_{surf} is at a maximum at the centre ($z = 0$) where the radius is largest, and decreases linearly towards the ends as the tumbler cross-sectional radius decreases. In a sphere, u_{surf} is a maximum at the centre of the sphere and decreases non-linearly toward the poles of the sphere. End-wall effects are not observed for these geometries, because the areas of the end walls are negligible.

The surface velocities can be plotted as a function of L for all three tumbler geometries, as shown in figure 13, including several different radii of cylindrical tumblers. (The range of values of the streamwise velocity for particular values of L reflects the high-velocity regions near the end walls in cylindrical tumblers.) The streamwise surface velocity, u_{surf}, is directly proportional to the half-length of the flowing layer, L. This result is consistent with dimensional arguments based on experiments in quasi-2d cylindrical tumblers [176].

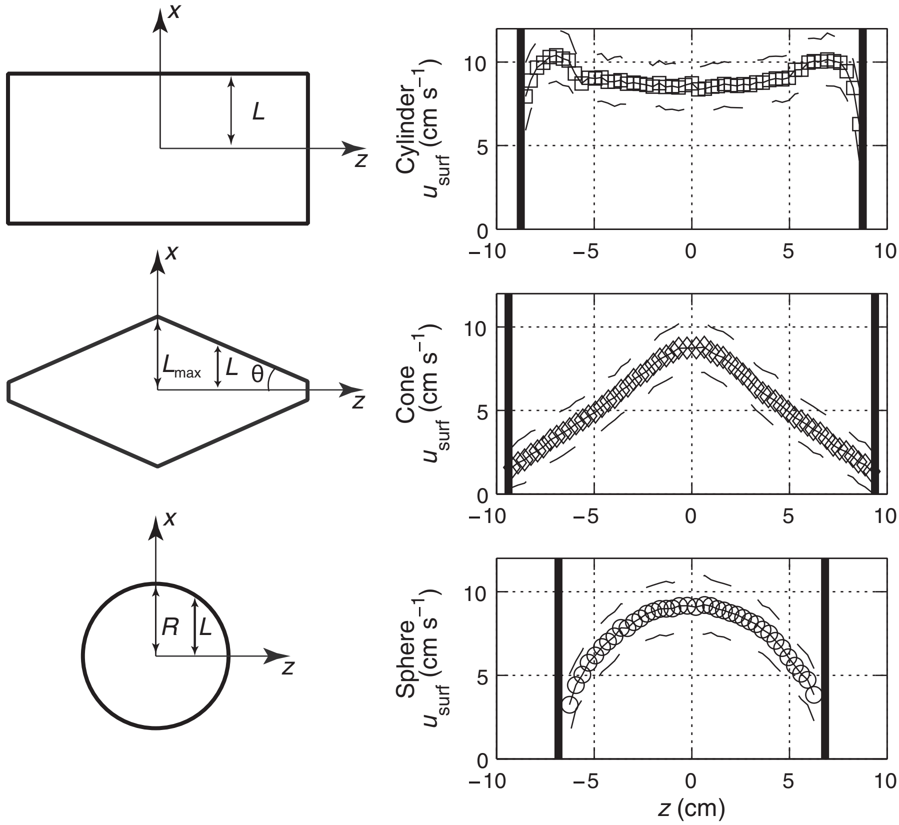

Figure 12. Surface velocity profiles for 2d + 1 DGS systems in 3d tumblers. Top: cylinder; middle: double cone; bottom: sphere. The rotation rate of all tumblers is 2.0 RPM. The maximum diameter of the tumblers is 136–140 mm. The tumblers are half-filled with 1.07 ± 0.04 mm black basalt glass particles. Reprinted with permission from [175]. © 2006 Cambridge University Press.

3. Continuum model

3.1. *Cross-sectional flow: 2d continuum model*

Consider a quasi-2d circular tumbler or a slice of a wholly 2d flow in a 3d geometry, such as a section in a sphere or a cone, as shown in figure 14. Flow is in the positive x direction. The mass balance in the flowing layer is given by

$$\frac{\partial(\rho\delta(x))}{\partial t}+\frac{\partial(\rho\bar{u}_x(x)\delta(x))}{\partial x}=\rho_{\mathrm{b}}v_y(x,\,-\delta(x)). \tag{1}$$

The right-hand side accounts for particles entering or leaving the element through the lower surface of the flowing layer from the fixed bed with velocity $v_y(x,\,-\delta(x))$. (Particles do not enter or leave through the top surface, so the normal velocity at the free surface is zero.) Assuming that the bulk density in the flowing layer, ρ, and the

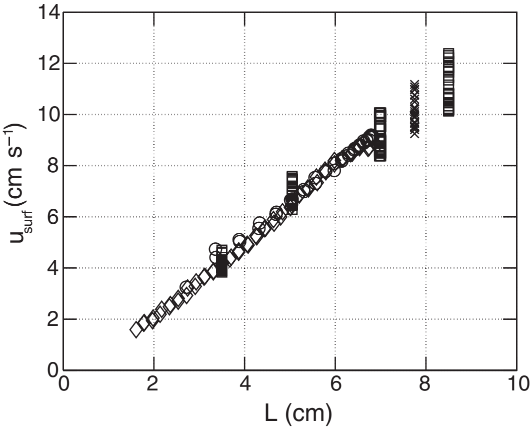

Figure 13. The surface velocity at $x = 0$, u_{surf}, is a linear function of L (half the flowing layer length) for all three tumbler geometries in figure 12 at the same rotation rate (2.0 RPM) for the same particle size (1.07 ± 0.04 mm black basalt glass particles). ◇, half-full double cone; ○, half-full sphere; □, half-full cylinder; ×, 25%-full cylinder with correction for the solid body rotation contribution to surface velocity. Reprinted with permission from [175]. © 2006 Cambridge University Press.

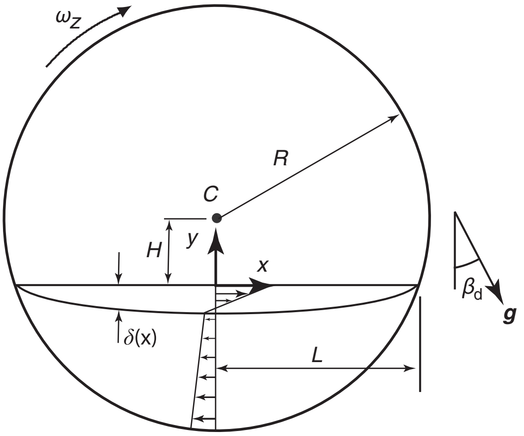

Figure 14. 2d circular tumbler of radius R rotated about its centre, C, at rotation rate, ω_z, where $\omega_z < 0$ for clockwise rotation as shown. The vertical position of the free surface relative to the axis of rotation is H. The distance between the centre of flowing layer and tumbler wall is L. The thickness of the flowing layer is $\delta(x)$.

bulk density in the fixed bed of solid body rotation, ρ_b, are similar and that the flow is pseudo-steady state, equation (1) becomes

$$\frac{\partial(\bar{u}_x(x)\delta(x))}{\partial x} = v_y(x, -\delta(x)). \tag{2}$$

We consider a circular tumbler, but the above equations and assumptions can be applied to any convex tumbler owing to the pseudo-steady state assumption: that is, the flow instantaneously adjusts to any changes in the length of the flowing layer. In figure 14, C is at the centroid of the tumbler, which in this case also corresponds to the axis of rotation and is parallel to the z-axis. The tumbler is oriented so that the x-axis is horizontal and the gravity vector is at angle $\beta_{\rm d}$ (the dynamic angle of repose) with respect to the y-axis. The position of the free surface with respect to the axis of rotation is H, which is negative if the tumbler is less than half full. The distance from the midlength of the free surface to the tumbler wall is $L \le R$. The thickness of the flowing layer is given by $\delta(x)$.

Two-dimensional solid body rotation in the fixed bed, $\boldsymbol{v}$, is given by

$$\boldsymbol{v} = (-\omega_z(H+y), \omega_z x), \tag{3}$$

where $\omega_z < 0$ so that the rotation is clockwise around the z-axis. Equation (2) can now be expressed as

$$\frac{\partial(\bar{u}_x(x)\delta(x))}{\partial x} = \omega_z x. \tag{4}$$

Equation (4) can be integrated with appropriate boundary conditions for the mass flux in the flowing layer determined from the geometry of the container. The streamwise velocity component, u_x, at the boundary between the flowing layer and the bed of solid body rotation equals the x-component of solid body rotation. (In utilizing this condition, the creeping velocity in the bed of solid body rotation [64, 65] is neglected.) As shown in figure 11 (see also [71]) and verified elsewhere [174, 177, 178], the dependence of the streamwise velocity on depth in the flowing layer is approximately linear. For the purposes of the model, we assume that the shear rate is constant, rather than depending on streamwise position ($\dot{\gamma} \neq \dot{\gamma}(x)$) (see [90, 153]). This assumption for the shear rate is one of several possible assumptions that can be made, as discussed below. So in the flowing layer, $0 \ge y \ge -\delta(x)$, the streamwise velocity at $y = -\delta(x)$ equals the x-component of solid body rotation given by equation (3) and then increases linearly with shear rate $\dot{\gamma}$ to a maximum at the free surface, $y = 0$. This is given by

$$u_x(x,y) = \dot{\gamma}(\delta(x)+y) - \omega_z(H+y). \tag{5}$$

Using the depth-averaged streamwise velocity, $\bar{u}_x(x) = (1/\delta(x))\int_{-\delta(x)}^{0} u_x(x,y)\,\mathrm{d}y$, the boundary condition is based on the mass flux at $x = -L$

$$\bar{u}_x(-L)\delta(-L) = \frac{\dot{\gamma}(\delta(-L))^2}{2} - \omega_z\left(H - \frac{\delta(-L)}{2}\right)\delta(-L). \tag{6}$$

Now $\delta(x)$ can be found by integrating equation (4) with the above boundary condition (6), so that

$$\delta(x) = \frac{\omega_z}{\dot{\gamma}+\omega_z}H \pm \left[\frac{\omega_z^2}{(\dot{\gamma}+\omega_z)^2}H^2 - \frac{\omega_z}{\dot{\gamma}+\omega_z}(L^2-x^2) + (\delta(-L))^2 - \frac{2\omega_z}{\dot{\gamma}+\omega_z}H\delta(-L)\right]^{1/2}. \tag{7}$$

From experiments [71, 175], $\dot{\gamma}/|\omega_z| \approx O(100)$. Furthermore, $H^2/L^2 \ll \dot{\gamma}/|\omega_z|$ where the flow is in the rolling or continuous-flow regime. The flowing layer is very thin $(\delta(x)^2/L^2) \ll 1$ and from experiments it is observed that $\delta(-L) = 0$. Thus, the equation for the flowing layer thickness, $\delta(x)$, simplifies to

$$\delta(x) = \sqrt{\frac{|\omega_z|}{\dot{\gamma}}}\sqrt{L^2 - x^2} \tag{8}$$

since $\delta(x) > 0$. The y-component of the velocity field in the flowing layer, $u_y(x, y)$, can be found from continuity within the layer, $\nabla \cdot \boldsymbol{u} = 0$, so that

$$u_y(x, y) = -\frac{\omega_z x y}{\delta(x)}. \tag{9}$$

Thus, a set of simple assumptions yields the shape of the flowing layer and the normal velocity. Furthermore, equations (5), (8) and (9) provide a complete description of the flow. For $H = 0$ (half-full tumbler), the second term on the right-hand side in equation (5) is typically neglected because $\dot{\gamma}/|\omega_z| \approx O(100)$. This results in a discontinuity at $y = -\delta(x)$, the effect of which is inconsequential. Finally, since this is a kinematical description of the flow, the acceleration of gravity and its orientation with respect to the free surface do not play a role in the expressions for the velocity and flowing layer thickness.

3.2. *Assumptions*

The development of the continuum framework depends on two basic assumptions. The first is that the streamwise velocity varies linearly with depth in the flowing layer, so that the shear rate, $\dot{\gamma}$, is constant with y at each streamwise position x. The second assumption relates to how the surface velocity varies with x. There are at least three different options for this assumption.

(A) The surface velocity is allowed to vary along the length of the flowing layer by assuming that the shear rate is constant, as is done here, leading to equation (5). Makse [153] used this assumption and took shear rate as a fitting parameter, while Khakhar *et al.* [90] derived the shear rate based on an analysis involving the solution of the momentum equation. The result is a surface velocity that has a maximum where the flowing layer thickness is maximum. This form of the model results in $\delta(x) \propto \sqrt{L^2 - x^2}$.

(B) The surface velocity is allowed to vary along the length of the flowing layer according to a boundary value approximation [152]. This approach, coupled with mass conservation and stress continuity at the interface between the flowing layer and the bed of solid body rotation leads to $\delta(x) \propto (L^2 - x^2)^{2/5}$.

(C) The surface velocity is assumed to be constant along the length of the flowing layer [18, 19, 86]. In this situation, the shear rate must vary with streamwise position, because the flowing layer thickness varies. This leads to $\delta(x) \propto (L^2 - x^2)$, a parabolic-shaped flowing layer.

The choice of which of the three assumptions to use is based on a balance of computational efficiency and model realism compared with experiments. Depending on tumbler geometry, there may be cases where the x-coordinate of a particle in the bed of solid body rotation is outside of the bounds of the flowing layer (for example, in a half-full rotating square as it approaches the diamond configuration). In this case, computing $\delta(x)$ for $|x| > L$ when using models derived from assumptions (A) or (B) is problematic. Therefore, conditions must be in place in the model implementation to require that $\delta(x) = 0$ when a particle is in solid body rotation and $|x| > L$. The model derived from assumption (C) does not require this because $\delta(x)$ is real for all x.

Assumption (A) is used here in spite of its computational drawbacks, because measurements of the streamwise surface velocity indicate that it reaches a maximum near the midlength of the flowing layer, and goes to zero at either streamwise end of the flowing layer [94, 175, 176] consistent with the result when assuming that the shear rate is constant. Assumption (B) is rarely used. However, it is important to note that any of the three assumptions yield similar results (e.g. Poincaré sections) when studying the overall dynamics of the flow [19, 87, 88, 90]. The determinant factors are the basic characteristic of the container, first, and the scaling with local flowing length, second. The details of the velocity field are unimportant in the structure of segregation patterns, Poincaré sections, etc.

3.3. *Deviations from symmetric flowing layer*

Assuming a constant shear rate (assumption (A)) results in a flowing layer that is symmetric about the y-axis ($\delta(x)$ is a maximum at the midlength of the flowing layer at $x = 0$). However, in the rolling regime, the flowing layer may be skewed or asymmetric [91, 94, 176]. A first principle model starting with the momentum balance yields an asymmetric layer [86, 90, 179]. The shear stress in the flowing layer at the interface with the bed of solid body rotation is [50]

$$\tau_{xy}|_{y=-\delta(x)} = -\rho\, d_p^2 f(\rho)(\dot{\gamma}(x))^2 - \rho g \delta(x) \cos\beta(x) \tan\beta_{\mathrm{s}}. \tag{10}$$

The first term on the right-hand side is the Bagnold stress [48] with $f(\rho) = c\delta/d_{\mathrm{p}}$, where c is a fitting parameter, typically having a value of $c \approx 1.5$ for 2d systems [90, 91]. The second term on the right-hand side is the Coulombic frictional stress, where β_{s} is the static angle of repose. $\beta(x)$ is the angle between horizontal and the boundary between the flowing layer and the fixed bed. The stress in equation (10) is balanced on the bed side of the interface by the static frictional stress,

$$\tau_{xy}|_{y=-\delta(x)} = -\rho g \delta(x) \cos\beta(x) \tan\beta_{\mathrm{d}}, \tag{11}$$

where β_{d} is the dynamic angle of repose. Using equations (10) and (11), it can be shown that

$$\dot{\gamma}(x) = \sqrt{\frac{g \cos\beta(x) \sin(\beta_{\mathrm{d}} - \beta_{\mathrm{s}})}{c d_{\mathrm{p}} \cos\beta_{\mathrm{d}} \cos\beta_{\mathrm{s}}}}. \tag{12}$$

Equation (12) makes it possible to model skewed velocity profiles where the angle between the bed–layer interface and horizontal varies with streamwise position. For very thin flowing layers where $\beta(x) \approx \beta_{\mathrm{d}}$, equation (12) yields a constant shear rate, consistent with the continuum model above. A result with similar dependence on g and d_{p}, $\dot{\gamma} = \sqrt{g \sin\beta_{\mathrm{d}}/d_{\mathrm{p}}}$, can also be obtained [180] simply by assuming that the shear rate is constant. The examples in this article are all generated using a flowing layer that is symmetric about the midpoint of the free surface, as generated by assumptions (A) or (C) in section 3.2.

3.4. *Time-periodic flows*

The equations for the continuum model were initially developed for circular tumblers. The streamlines in the thin flowing layer are nearly parallel to the free surface while particle paths in the fixed bed are semicircles concentric with the tumbler wall. When tumblers are non-circular, particle paths are harder to predict and this is where continuum models can provide substantial insight.

Changes in the length of the flowing layer in polygonal tumblers are easily handled by means of a pseudo-steady-state approximation that incorporates the instantaneous value for the half-length of the flowing layer, $L(t)$, in equation (8) for the flowing layer thickness. Thus, the flowing layer thickness varies with the tumbler orientation leading to a variation in the velocity in the flowing layer.

Complications arise when the distance between the centroid of the tumbler and the free surface, H, changes with time owing to the tumbler geometry so that $H = H(t)$. An example is a 25%-full square tumbler as shown in figure 15. For a square with side length S, $H = -0.25S$ when the flowing layer is parallel to a wall as shown in figure 15(a). However, when the square is in the diamond configuration, $H = -0.21S$ as shown in figure 15(b). Owing to the shape of the tumbler, H periodically varies with time, $H(t) = H(t + T)$. This is handled by using the pseudo-steady-state approximation that the flow instantaneously adjusts. The change in H is applied to the y-position of the points in the flowing layer. This may be thought of as adding $\mathrm{d}H/\mathrm{d}t$ to u_y in equation (9) (see [111]).

In half-full even-sided tumblers, the y-axis at the origin of the coordinate system in the flowing layer (located at the streamwise midlength of the free surface) always extends through the centroid of the tumbler. This is not always the case in even-sided tumblers at fill fractions that deviate from half full and in odd-sided tumblers of all fill fractions. For example, in the situation shown in figure 15, not only is H changing in time, but the midpoint of the free surface of the flowing layer is also moving with respect to the centroid of the tumbler.

This issue is more clearly illustrated in a triangular tumbler shown in figure 16. When the triangle is pointing up (figure 16(a)) or pointing down (figure 16(c), the y-axis of the coordinate system extends through the centroid of the tumbler. However, when the triangle is pointing to the side (figure 16(b)), the y-axis of the coordinate system, which is located at the midpoint of the flowing layer, is displaced in the streamwise direction from the centroid by a distance c. Although $\mathrm{d}H/\mathrm{d}t$ is included in the velocity equations to account for height changes, $\mathrm{d}c/\mathrm{d}t$ is not because it is typically small compared with the magnitude of the streamwise velocity, u_x (see [111]). Figure 16 also illustrates that for half-full odd-sided tumblers, the distance between the surface of the flow and the axis of rotation can change with tumbler orientation.

Time-periodic flow for the case of periodic modulation of the rotation rate, $\omega(t) = \omega(t + T)$, is also readily handled by means of a pseudo-steady-state approximation in the flow equations. As illustrated in figure 17, the thickness of the flowing

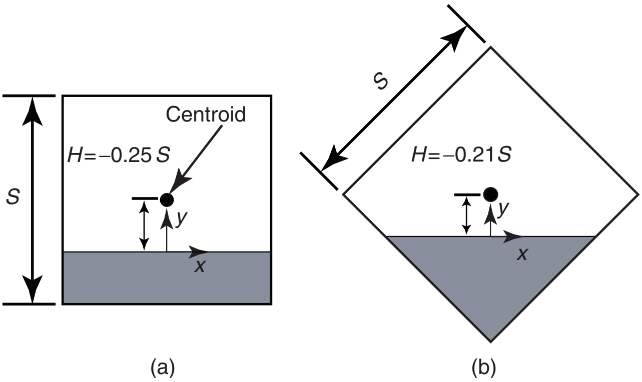

Figure 15. In a 25%-full square tumbler, H is a function of time depending on tumbler orientation. (a) When the square is in the upright configuration with the flowing layer parallel to a wall with length S, $H = -0.25S$. (b) When the square is in the diamond configuration with the flowing layer parallel to the diagonal, $H = -0.21S$.

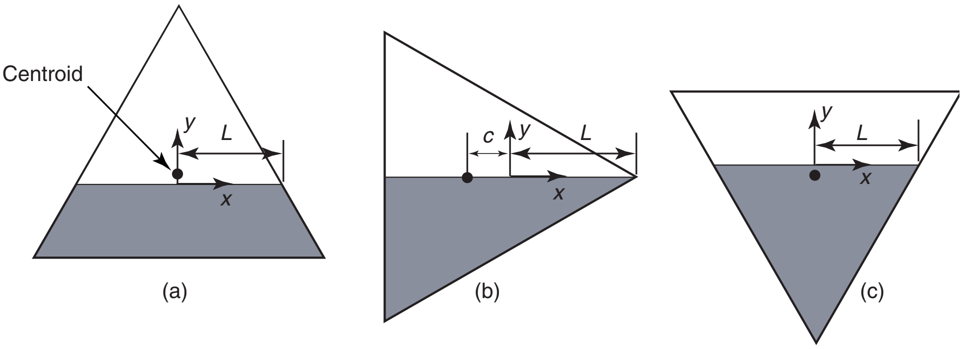

Figure 16. Half-full triangle at different orientations. Note that both the vertical orientation of the surface and the horizontal orientation of the origin of the coordinate system change with respect to the axis of rotation as the tumbler orientation changes.

layer $\delta(x)$ depends on the rotation rate, ω, according to equation (8). As the rotation rate increases, the flowing layer thickness increases. The velocity in the flowing layer also increases according to equations (5) and (9). Thus, a time-periodic modulation of the rotation rate results in time periodicity of the flow.

3.5. *2d + T flows*

3.5.1. Poincaré sections and time-periodic flow. Consider as an example steady flow in a quasi-2d circular tumbler (figure 2(a)) and time-periodic flow in a quasi-2d square tumbler (figure 4(b)). The character of these flows can be studied through the use of computational Poincaré sections [181]. The computational Poincaré sections for half-full tumblers generated in figures 18(a) and (c) are produced in

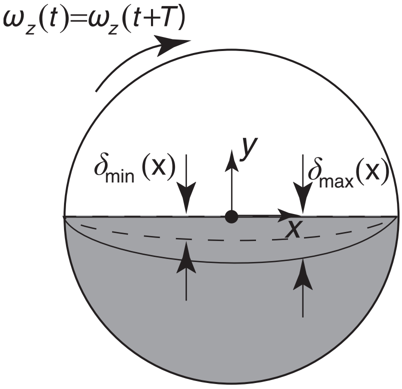

Figure 17. For 2d + T flow generated from time-periodic modulation of quasi-2d circular tumbler, the flowing layer thickness and velocity profile depend on the instantaneous value of the time-periodic rotation rate as given in equations (5), (8) and (9).

the following way. Points are initially seeded in the filled portion of the tumbler domain and these points are advected according to the 2d continuum model (equations (5), (8) and (9)) as the tumbler rotates clockwise.

For example, in the square tumbler (figure 18(c)), points are placed along one of the diagonals and advected according to the 2d continuum model. The positions of points are plotted every one-quarter revolution as the tumbler rotates clockwise. This periodicity is a result of the tumbler returning to the same rotational orientation every one-quarter revolution. In the case of the circle the flow is steady, so the period can be chosen arbitrarily. In figure 18(a), the points are plotted each one-half revolution.

The Poincaré section for the square (figure 18(c)) has more complicated features than those of the circle (figure 18(a)). In the square, the points do not travel on closed semicircular streamlines as they do for the circular tumbler. Instead, some points are confined to islands, while others are advected over much of the tumbler. There are also points that return exactly to their initial position after some number of periods, referred to as periodic points. The existence of periodic points is guaranteed by Brouwer's fixed point theorem [183, 184]. All that is required is that the flow occurs in a singly connected domain, such as in the circle or the square. If the system is viewed at two arbitrary times (t_1 and t_2), then at least one point viewed at t_1 is in exactly the same position at t_2 (see [185]).

Let us state a few definitions concerning periodic points. For details the reader should consult the book by Ottino [181]. Consider the flow as a mapping $\boldsymbol{\phi}(\boldsymbol{x})$, where a particle in position $\boldsymbol{x}_n$ gets mapped to $\boldsymbol{x}_{n+1}$, i.e. $\boldsymbol{x}_{n+1} = \boldsymbol{\phi}(\boldsymbol{x}_n)$. A particle beginning at position $\boldsymbol{p}$ is said to be of a period n if $\boldsymbol{p} = \boldsymbol{\phi}^n(\boldsymbol{p})$. In 2d preserving maps, these periodic points may be classified as *elliptic*, where the nearby linearized flow is a rotation, or *hyperbolic*, where the nearby linearized flow is contraction in one direction and stretching in the other. Elliptic points are the subject of the Kolmogorov–Arnold–Moser (KAM) theorem [186–188]. Ellipse-shaped rings such as those shown along the diagonals of the tumbler in figure 18(c), are characteristic of elliptic points.

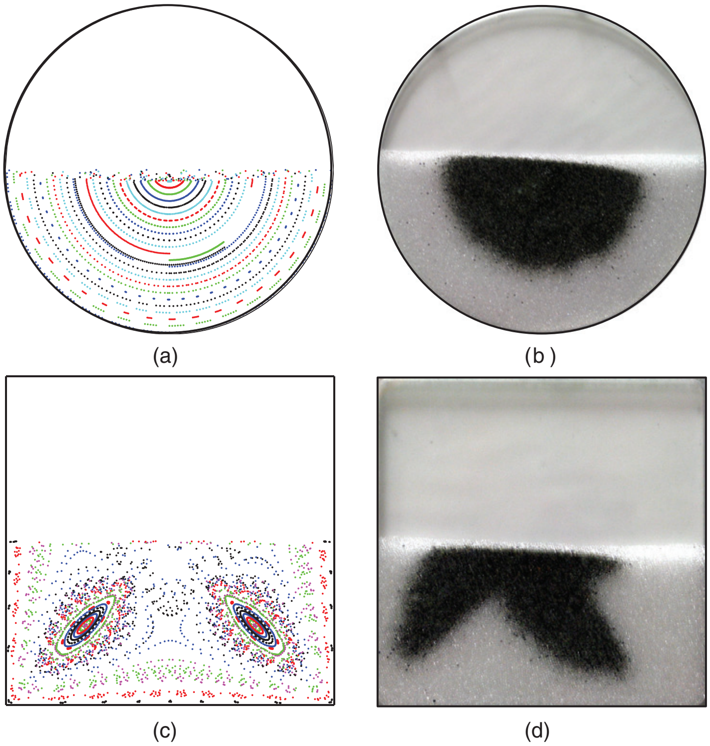

Figure 18. Application of continuum model to 2d systems. Rotation is clockwise in all figures. (a) Computational Poincaré section for a 2d circular tumbler. (b) S_2-DGS segregation experiment in a quasi-2d circular tumbler. (c) Computational Poincaré section in a 2d square tumbler. (d) S_2-DGS segregation experiment in a quasi-2d square tumbler. In both experiments, the large particles are 1.21 mm clear glass particles and the small particles are 0.29 mm painted black glass particles. Both tumblers are made of acrylic. The circular tumbler has a diameter of 222 mm. The square tumbler has a side length of 157 mm. Both tumblers are 6 mm thick. See online version for colour. Part (d) Reprinted with permission from [182]. © 2006 American Physical Society.

These rings are typically referred to as *KAM regions* or *islands*; KAM regions are invariant and serve as barriers to mixing. Material inside the rings cannot cross to the outside and material outside cannot cross to the inside [181, 189, 190]. Material in an island also undergoes a *twist* [181, 191]. In general, larger islands are characterized by lower-order elliptic points [185]. On the other hand, hyperbolic points characterize chaotic flow and are generally good for mixing.

3.5.2. Segregation patterns. Figure 18 shows a striking similarity between the patterns in the computationally derived Poincaré sections (figures 18(a) and (c)) and the segregation patterns from S_2-DGS experiments in quasi-2d tumblers (figures 18(b) and (d)). In the case of the half-full circular tumbler (figure 18(b)), the small black particles have segregated from the large particles to form a semicircular radial core as the tumbler rotates clockwise. In the half-full square tumbler rotating clockwise (figure 18(d)), the small black particles have segregated to form two lobes that stretch from the centre of the tumbler toward the bottom corners. These two lobes overlap approximately with the islands in the computational Poincaré section (figure 18(b)). This similarity between the location of the islands of the computational Poincaré section and the lobes of the experimental segregation patterns is particularly interesting because the continuum model used to produce the Poincaré sections (equations (5), (8) and (9)) contains no information about segregation. Although time-periodic flows generally enhance the mixing of monodisperse species by means of chaotic advection, particles varying in size or density still segregate into patterns clearly influenced by the underlying kinematics of the flow illustrated by the computational Poincaré sections.

The similarity between the pattern of the Poincaré section and the segregation pattern holds for a variety of tumbler shapes and particle concentrations [182]. Figure 19 shows the example of a half-full quasi-2d tumbler with a pentagonal cross section. The Poincaré section (figure 19(a)) shows complicated dynamics. There are two inner islands surrounded by five outer islands. At low small-particle concentration for a S_2-DGS (figure 19(b)), the small particles form a segregation pattern with two lobes that correspond to the two islands along the diagonals in the Poincaré section. When the small-particle concentration is increased (figure 19(c)), the small particles form a segregation pattern that is similar to the outline of the five island region. By using three different sizes of particles (figure 19(d)), it is possible to capture the shape of the inner two island regions and the outer five island regions at the same time.

3.5.3. Applications to LGSs. Segregation patterns in LGSs comprise lobes that coincide with the location of islands in computational Poincaré sections in the same manner as for DGSs [192]. Figure 20 shows a case where the time periodicity arises from a time-periodic modulation of the rotation rate of a quasi-2d circular tumbler. The rotation rate is modulated so that it reaches a maximum four times per revolution resulting in a lobed segregation pattern. The similarity of segregation patterns between the LGS (figure 20(a)) and the DGS (figure 20(b)) demonstrate the overlap in the physics of these two systems. Once again, the lobes of the segregation patterns shown in figures 20(a) and (b) correspond to the location of the islands in the computational Poincaré section shown in figure 20(c).

3.5.4. Relating segregation patterns and Poincaré sections. The underlying reason that computational Poincaré sections and segregation experiments capture the same patterns can be traced back to an analysis of the periodic points [182]. Islands (such as the two small islands along the diagonals in the lower half in figure 21(a)) are characterized by elliptic points. (There is a third island in the flowing layer that is much more difficult to see.) On the other hand, chaotic regions are characterized by hyperbolic points. In this case, a hyperbolic point is located in the lower half of the figure halfway between the two islands (figure 21(b)). There are also two hyperbolic points along the horizontal midline of the tumbler.

The character of the periodic points can be determined by computing the Jacobian, **J**, of the linearization of the mapping, $\boldsymbol{\phi}^n(\boldsymbol{x})$ [182]. In 2d systems, there are two eigenvalues, λ_1 and λ_2, and corresponding eigenvectors. The eigenvalues are found from the condition $\det(\mathbf{J}) = 1$ so $\lambda_1\lambda_2 = 1$. If $\lambda_{1,2} = A \pm \mathrm{i}B$ where $B \neq 0$, then

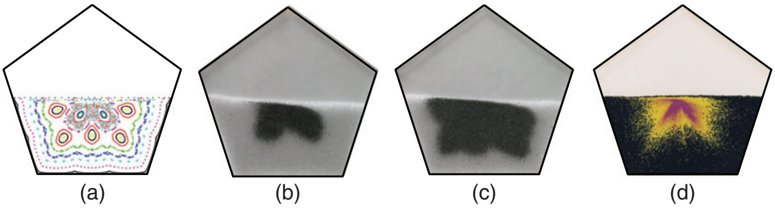

Figure 19. Experimental segregation patterns capture the patterns and location of islands in the computational Poincaré section in a half-full quasi-2d pentagonal tumbler. (a) Computational Poincaré section. (b) Segregation result for S_2-DGS with 10% by weight small particles. (c) Segregation result for S_2-DGS with 30% by weight small particles. (d) Three-phase segregation result for S_3-DGS (70% by weight large, 25% by weight medium and 5% by weight small particles). In (b) and (c) the large particles are 1.21 mm clear glass and the small particles are 0.29 mm painted black glass. In (d) the large particles are 1.19 mm painted black glass, the medium particles are 0.75 mm painted yellow glass and the small particles are 0.35 mm painted purple glass. The acrylic pentagonal tumbler has a side length of 141 mm and a thickness of 6 mm. Reprinted with permission from [182]. © 2006 American Physical Society.

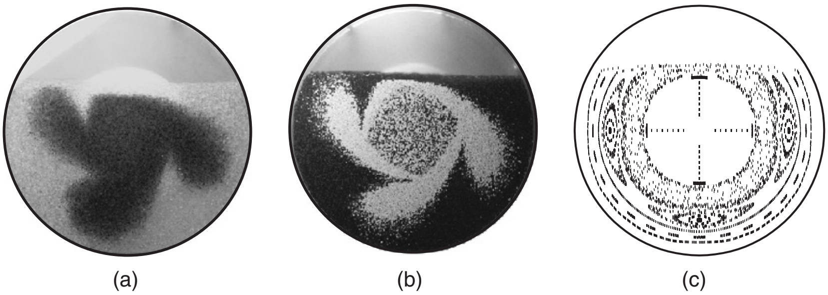

Figure 20. Segregation patterns of a S_2-system that develops in quasi-2d circular tumblers that are more than half-full and undergoing periodic forcing (varying the tumbler rotational speed at four times per tumbler rotation). Rotation of the tumbler is clockwise. (a) S_2-LGS, 0.8 mm clear glass particles and 0.3 mm painted black glass particles. (b) S_2-DGS, 1.2 mm painted blue glass particles and 0.8 mm white zirconium particles. (c) Poincaré section. In (a) and (b), the acrylic tumbler is 178 mm in diameter and 6.4 mm thick. Reprinted with permission from [192]. © 2005 Cambridge University Press.

the point is elliptic. If $\lambda_{1,2}$ are both real (imaginary component is equal to zero), not equal to 1, and are reciprocals of each other, then the point is hyperbolic. The eigenvalue with a modulus greater than 1 has an eigenvector that corresponds to the direction of stretching. The eigenvalue with a modulus less than one has an eigenvector that corresponds to the direction of compression. If $\lambda_{1,2} = \pm 1$, the point is said to be parabolic. Parabolic points correspond to steady shear flow such as that seen in quasi-2d circular tumblers rotated at a constant rate of rotation. Their influence can be seen in the Poincaré section shown in figure 18(a). In the half-full quasi-2d circular tumbler, there is a curve of parabolic points radially located approximately at half the radius of the tumbler. The shearing influence of

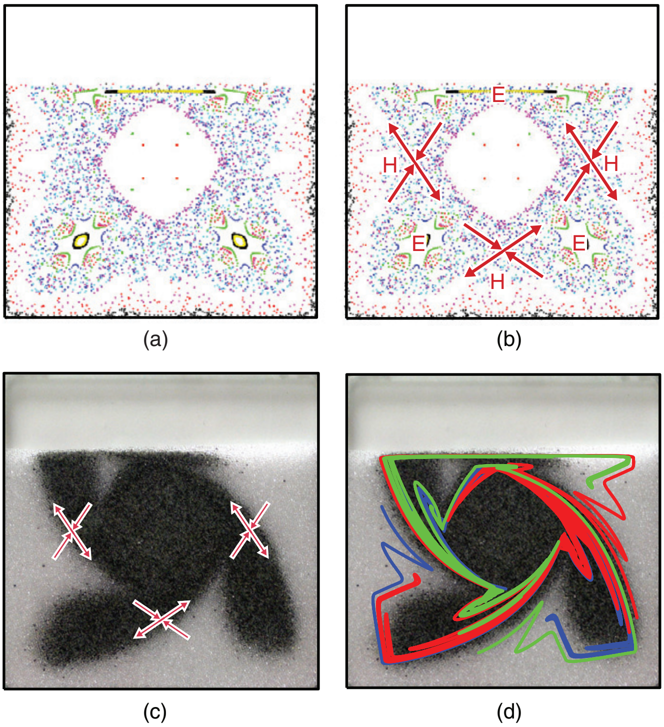

Figure 21. Square tumbler 75% full. (a) Poincaré section. (b) Poincaré section with periodic points labelled as either elliptic (E) or hyperbolic (H). Hyperbolic points have corresponding eigenvectors. (c) Quasi-2d S_2-DGS experiment with eigenvectors associated with hyperbolic points overlaid on the segregation pattern. Large particles are 1.21 mm clear glass. Small particles are 0.29 mm painted black glass. The acrylic square tumbler has a side length of 157 mm and a thickness of 6 mm. Note that the arms made up of smaller particles in the experiments (darker regions) correspond to the invariant regions in the Poincaré section. (d) Unstable manifold tracing from each of the hyperbolic points overlaid on the experimental results. Adapted with permission from [182]. © 2006 American Physical Society.

the parabolic points results in the points radially closer to the centre of the tumbler extending clockwise after each time period of flow with respect to a vertical line through the centre. This behaviour is seen in the curve of red points near the radial position at about half the radius of the tumbler in figure 18(a). This curve is generated by the gradual movement of the point each time period in the clockwise direction. The curve of points radially further away but still close to this half-way point (shown in green) is extending counterclockwise relative to a vertical midline.

The similarities between the computational Poincaré sections and the experimental segregation patterns can be explained through the dynamics associated with the hyperbolic points [182]. The eigenvector that corresponds to the direction of stretching is tangent to the unstable manifold, while the eigenvector that corresponds to the direction of compression is tangent to the stable manifold. The manifold can be traced by seeding many points around each of the hyperbolic points [193] and advecting them according to the continuum model (equations (5), (8) and (9)). As can be seen in figure 21(d), unstable manifolds trace out the same shape as the segregation pattern.

Thus, the lobes of the segregation pattern form due to the interplay of the tendency of bidisperse granular material to segregate based on size or density differences and the underlying dynamics of the time-periodic flow. Once particles segregate in the flowing layer, they flow as if they were monodisperse. The particles that are higher in the flowing layer (for S-systems, the large particles) are subject to the dynamics of the upper portion of the flowing layer, which corresponds to the outermost regions of the Poincaré section. The particles in the bottom of the flowing layer (for S-systems, the small particles) are subject to the dynamics of the lower portion of the flowing layer, which corresponds to the innermost regions of the Poincaré section. While the segregated small (or heavy) particles appear to mimic the islands characterized by elliptic points in Poincaré sections, they are also influenced by the dynamics of the chaotic regions characterized by hyperbolic points. The segregated lobes tend to stretch along the direction of the stretching eigenvectors associated with the hyperbolic points. Tracing of the unstable manifold (to which the stretching eigenvector is tangent) reveals the overall curvature of the segregation pattern as shown in figure 21(d).

4. Model for segregation: interpenetrating continua

Flows of polydisperse granular materials can be modelled using the continuum model presented in section 3.1 by incorporating a constitutive equation that includes a drift velocity for segregation and by assuming the different materials behave as interpenetrating continua [18, 111]. A few authors have proposed other models of segregation. Hsiau and Hunt [194] and Khakhar *et al.* [195] studied segregation of bidisperse granular materials using kinetic theory models for binary mixtures [196, 197]. Other models include those by Savage and Lun [113], which uses a percolation mechanism for size segregation, and by Dolgunin *et al.* [115, 116], who propose a phenomenological model for size and density segregation that depends on particle concentration and granular temperature.

4.1. *Constitutive model for segregation*

Consider a D_2-system of particles with the same diameter, d_p, but two different densities or masses, m_h and m_l (h for heavy, l for light) in a shear-like motion, as in the case of a flowing layer in a tumbler (figure 3(b)). In the simplest heuristic picture, one can imagine that buoyant forces act on each type of particle, so drift velocities relative to the mean flow are generated in the flowing layer. Light particles rise to the top of the flowing layer and heavy particles sink towards the bottom. The derivation developed here for a D-system follows Khakhar *et al.* [18], but the derivation is analogous for an S-system. The assumption is that large particles in an S-system behave in a similar manner to light particles in a D-system; small particles in an S-system behave like heavy particles in a D-system. Systems where size and density differences are both at play [66, 67] are difficult to handle because of the interplay between the buoyancy and percolation, so these systems are not considered here.

The velocity field in the flowing layer is dependent on the local concentration of heavy particles, f, where $f = 1/V\int_V n_h \, dV$, with n_h being the number of particles of mass m_h, and V being the size of a local control volume associated with a given position in the flowing layer such that $O(V) \gg O(d_p^3)$. The notation is the same as before except now velocities corresponding to each particle type are denoted with a subscript h or l for heavy or light. The dependence on position through the variables x and y is the same as with monodisperse particles, but now there is an additional parameter f (which is shown after a semicolon, because it is a parameter associated with the position (x, y), not an independent variable). The velocity of points that represent particles of each type is given by

$$\boldsymbol{u}_h(x, y; f) = \boldsymbol{u}(x, y) + \boldsymbol{q}_h(f) \tag{13}$$

and

$$\boldsymbol{u}_l(x, y; f) = \boldsymbol{u}(x, y) + \boldsymbol{q}_l(f), \tag{14}$$

where $\boldsymbol{q}_h$ and $\boldsymbol{q}_l$ are the segregation drift velocities, and $\boldsymbol{u}$ is given by equations (5) and (9). By describing the motion in this way, we are referring to *particles* in a continuum mechanics sense, much like fluid particles in the Lagrangian approach to fluid flow. In the continuum model, a point that which represents a particle of a given type (heavy or light) is simply advected according to the continuum model. There are no particle–particle interactions. Noting that the average velocity is $\boldsymbol{u} = f\boldsymbol{u}_h + (1-f)\boldsymbol{u}_l$, then

$$\boldsymbol{q}_l = -\boldsymbol{q}_h \frac{f}{1-f}. \tag{15}$$

The simplest assumption is that the drift velocity of the heavy particles is proportional to the buoyancy force arising from the different masses of the particles and proportional to $\boldsymbol{g}$ [18, 115, 116], so that

$$\boldsymbol{q}_h = C\boldsymbol{g}\left(\frac{m_h - m_l}{m_h}\right)(1-f), \tag{16}$$

where C is a coefficient. The dependence on $(1-f)$ reflects the drift velocity for heavy particles being dependent on the local concentration of light particles. Using equation (15), the drift velocity of the particles with mass m_l is

$$\boldsymbol{q}_l = -C\boldsymbol{g}\left(\frac{m_h - m_l}{m_h}\right)f. \tag{17}$$

The rate of change of volume of the phase space occupied by the two species is equal,

$$\nabla \cdot \boldsymbol{u}_h = \nabla \cdot \boldsymbol{u}_l = -C\boldsymbol{g}\left(\frac{m_h - m_l}{m_h}\right) \cdot \nabla f. \tag{18}$$

Thus, $\nabla \cdot \boldsymbol{u}_h \neq 0$ and $\nabla \cdot \boldsymbol{u}_l \neq 0$ until a steady state is reached where the particles are segregated into regions of the same type, $f = 1$ or $f = 0$ (so that $\nabla f = 0$, except at discontinuities between segregated regions). Once this has occurred, particles travel with the mean flow, but there is no segregation velocity.

This constitutive model for segregation is readily incorporated into the continuum model of section 3.1. As particles move according to the continuum model, they also drift upwards or downwards in the flowing layer owing to buoyancy effects according to the constitutive segregation model. The advantage of using a continuum model over a particle dynamics simulation is that not all of the particles need to be simulated. Furthermore, particle–particle interactions need not be considered. Rather, tracer points are seeded in the phase space and advected according to the equations of motion. Although the motions of particles are not determined from force balances, particle interactions by means of the local buoyancy are calculated for all points in the flowing layer at each timestep. The strength of the continuum model together with the constitutive segregation model is demonstrated in figure 22 for 2d + T flows in polygonal tumblers. The segregation pattern of the density difference driven model matches that of S_2-DGS experiments at a high level of detail including the shape and number of lobes, as well as the curvature and asymmetry of the lobes. This comparison illustrates the qualitative similarities between density segregation, which is driven by buoyancy, and size segregation, which is driven by percolation.

This constitutive model is quite possibly the simplest, although variations are possible. One option is to make the drift velocities vary with a power of f. While the transient behaviour may vary with changes in the power of f, previous work indicates that the long-time behaviour is nearly the same [111].

4.2. *Collisional diffusivity*

The importance of collisional diffusivity can be characterized in terms of the Péclet number, Pe, the ratio of the diffusive time scale to the advective time scale [18, 88]. The advective time scale comes from the characteristic length scale in the streamwise direction, L, divided by the characteristic streamwise velocity, the

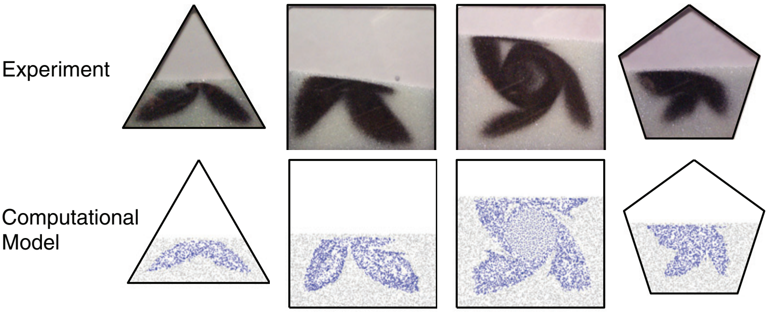

Figure 22. Examples of results from the computational segregation model compared with S_2-DGS experiments. The small black painted glass particles have a diameter of 0.30 mm. The large clear glass particles have a diameter of 0.85 mm. The triangular tumbler has a side length of 118 mm. The square tumblers have a side length of 157 mm. The pentagon has a side length of 68 mm. All tumblers are made of acrylic and are 6 mm thick. Posterboard inserts were used to produce the triangular and pentagonal cross sections. Figures not to scale. Adapted with permission from [111]. © 2006 American Physical Society.

depthwise-averaged streamwise velocity at the midlength $\bar{u}_x(0)$: $L/\bar{u}_x(0)$. The diffusive time scale in the direction normal to the flowing layer is $(\delta(0))^2/D_{\mathrm{coll}}$, so

$$\mathrm{Pe}_y = \frac{(\delta(0))^2 \bar{u}_x(0)}{L\, D_{\mathrm{coll}}}. \tag{19}$$

The diffusive time scale in the streamwise direction is the time it takes a particle to move diffusively half the length of the flowing layer L^2/D_{coll}, so

$$\mathrm{Pe}_x = \frac{L\bar{u}_x(0)}{D_{\mathrm{coll}}}. \tag{20}$$

The length scale for diffusive transport in the transverse direction for 3d tumblers is similar to that for streamwise transport, so $\mathrm{Pe}_z = \mathrm{Pe}_x$. Typically $\mathrm{Pe}_x \gg \mathrm{Pe}_y$ (see [18]).

Returning to the segregation model, the ***Cg*** term in (16) and (17) is a characteristic segregation velocity that is related to collisional diffusivity. The segregation velocity in the streamwise direction, Cg_x, is small compared with the advective velocity, so it can be neglected. The component normal to the streamwise direction can be expressed in terms of the collisional diffusivity of the particles, D_{coll}, as

$$C g_y = -\frac{4D_{\mathrm{coll}}}{d_{\mathrm{p}}}, \tag{21}$$

where the prefactor of '4' comes from a study using Monte Carlo simulations and particle dynamics simulations that showed that the dimensionless segregation velocity varies inversely with granular temperature [18, 19]. With this relationship, parameters including the prefactor in equation (21) were chosen so that the computational result using the continuum model matched experimental observations [18]. A scaling relation for collisional diffusivity from particle dynamics computations for shear flow [198] that has been confirmed experimentally [199] can be used for the collisional diffusivity:

$$D_{\mathrm{coll}} = g(\nu) d_{\mathrm{p}}^2 \dot{\gamma}, \tag{22}$$

where the prefactor $g(\nu)$ depends on the solids volume fraction, ν. For particles similar to the type considered here with a typical solids volume fraction, $\nu = 0.55$, $g(\nu) \approx 0.025$ [88]. Alternatively, the Péclet number can be estimated or specified, and equation (19) used to provide an estimate for D_{coll}.

4.3. *Computational considerations*

The constitutive model for segregation depends on the number fraction, f, which can be determined in several different ways. The *bin method* uses the fraction of the heavy particles within a cell or bin of a pre-defined grid. In the case of figure 23(a) where dark particles are heavy, $f = 5/7$. Of course, a weakness of this method is that the spatial resolution is constrained by the size of the bin. With the depth of the flowing layer being only $O(10)$ particles thick, it is difficult to obtain a meaningful estimate of the dependence of f on y. Furthermore, segregation does not depend on all of the particles surrounding an individual particle. For a heavy particle, segregation depends on how many light particles are below it; for a light particle, segregation depends on how many heavy particles are above it.

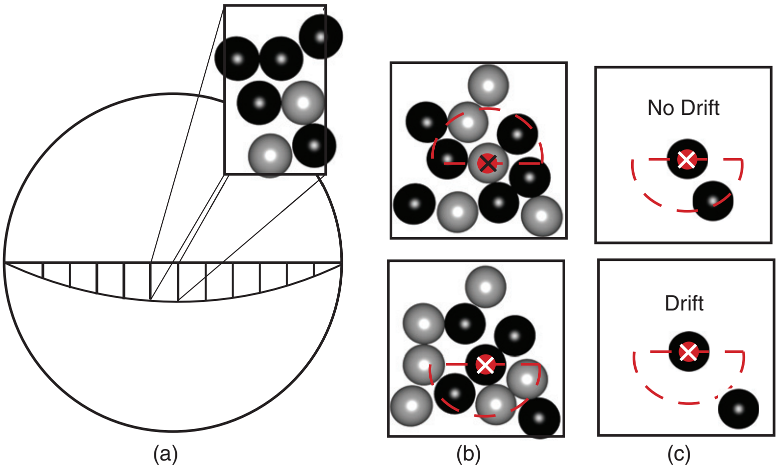

Figure 23. Illustration of the different methods of calculating *f*. (a) Bin method; (b) local concentration method; (c) bitwise operator method which is particularly useful in 3d applications. In all cases, *f* is computed at each timestep for points that represent particles in the flowing layer.

The *local concentration method* avoids these problems by considering particles within a given radius of an individual particle, either just above or just below it [111]. For a light particle, such as that labelled by a × at its centre in the upper portion of figure 23(b), only the concentration above that point is considered. In the illustration, $f = 2/3$. For a heavy particle, the concentration below that point is considered, as shown in the lower portion of figure 23(b), $f = 1/3$.

In the 3d case, the local concentration method can be computationally intensive. However, by taking advantage of the continuum viewpoint, only particles of one type need to be tracked by means of a bitwise operator that indicates whether a particle drifts or not. In the case of the upper portion of figure 23(c) there is at least one heavy particle within a prescribed radius below the labelled heavy particle, so the particle will not drift downwards. If a heavy particle has no other heavy particles as near neighbours below, as illustrated in the lower portion of figure 23(c), it drifts downwards. Particles that are not being tracked, in this example light particles, are not included, reducing computational time.

4.4. *Two-dimensional continuum model with segregation and diffusion*

The full 2d interpenetrating continua model for mixing and segregation of two types of particles (heavy and light) can be expressed using equations (13) and (14) with equations (16), (17) and (21) to yield the streamwise velocity for both heavy ($u_{x,\mathrm{h}}$) and light ($u_{x,\mathrm{l}}$) particles

$$u_{x,\mathrm{h}} = u_{x,\mathrm{l}} = \dot{\gamma}(\delta(x) + y) - \omega_z(H + y) + k_x, \tag{23}$$

the normal velocity for heavy particles

$$u_{y,\mathrm{h}} = -\frac{\omega_z xy}{\delta(x)} - 4\frac{D_{\mathrm{coll}}}{d_{\mathrm{p}}}\left(\frac{m_{\mathrm{h}} - m_{\mathrm{l}}}{m_{\mathrm{h}}}\right)(1-f) + k_y \tag{24}$$

and the normal velocity for light particles

$$u_{y,\mathrm{l}} = -\frac{\omega_z xy}{\delta(x)} + 4\frac{D_{\mathrm{coll}}}{d_{\mathrm{p}}}\left(\frac{m_{\mathrm{h}} - m_{\mathrm{l}}}{m_{\mathrm{h}}}\right)f + k_y. \tag{25}$$

Here k_x and k_y are white noise terms related to the collisional diffusivity, D_{coll}, that represent random diffusion in the x and y directions inherent in the flow, regardless of segregation drift velocities. The integrals of k_x and k_y over time Δt give sets of Gaussian random numbers with variance $2D_{\mathrm{coll}}\Delta t$ (see [88]). Diffusion in the streamwise direction k_x is typically neglected.

5. Three-dimensional continuum framework

The extension of the 2d model to 3d + T systems is conceptually straightforward. Consider rotations about the two axes (x_1 and x_3), $\boldsymbol{\omega} = (\omega_1, 0, \omega_3)$, as shown in figure 6 for ω_1 having a positive value and ω_3 having a negative value. There is a coordinate system x, y, z for the granular matter within the tumbler with unit vector, $\boldsymbol{k}$, along the instantaneous axis of rotation which is parallel to the z-axis, such that the rotation is clockwise when viewed along the z-axis (as is the case in figure 8) defined with respect to x_1, x_2, x_3 as

$$\boldsymbol{k} = \frac{(-\omega_1, 0, -\omega_3)}{\sqrt{\omega_1^2 + \omega_3^2}}. \tag{26}$$

The surface flow is assumed to adjust instantly so that the streamwise direction of the flow is orthogonal to $\boldsymbol{k}$ but at the dynamic angle of repose, β_{d}, with respect to the plane of axes x_1 and x_3, so the unit vector in the flow direction is

$$\boldsymbol{i} = \left(\frac{-\omega_3}{\sqrt{\omega_1^2 + \omega_3^2}}\cos\beta_{\mathrm{d}},\ -\sin\beta_{\mathrm{d}},\ \frac{\omega_1}{\sqrt{\omega_1^2 + \omega_3^2}}\cos\beta_{\mathrm{d}}\right). \tag{27}$$

The unit vector that is normal to the flowing free surface is

$$\boldsymbol{j} = \left(\frac{-\omega_3}{\sqrt{\omega_1^2 + \omega_3^2}}\sin\beta_{\mathrm{d}},\ \cos\beta_{\mathrm{d}},\ \frac{\omega_1}{\sqrt{\omega_1^2 + \omega_3^2}}\sin\beta_{\mathrm{d}}\right). \tag{28}$$

Note that if $\beta_{\mathrm{d}} = 0$, then $\boldsymbol{j} = (0, 1, 0)$ ($\boldsymbol{j}$ points along the x_2 direction). If $\omega_1 = 0$ and $\omega_3 < 0$, then $\boldsymbol{k} = (0, 0, 1)$ and $\boldsymbol{i} = (1, 0, 0)$, which is the situation for the 2d flow shown in figure 14. Finally, if, instead, $\omega_3 = 0$ and $\omega_1 > 0$, then $\boldsymbol{k} = (-1, 0, 0)$ and $\boldsymbol{i} = (0, 0, 1)$. This results in the $-x_1$ direction as the instantaneous axis of rotation and the x_3 direction as the streamwise direction.

Thus, the x direction is the instantaneous streamwise direction, the instantaneous transverse direction is along the z direction (parallel to the instantaneous axis of rotation) and the y direction is normal to the instantaneous flowing surface. The relationship between the coordinate axis system x_1, x_2, x_3 for rotation (with rotation about the x_1-axis and the x_3-axis, and gravity parallel to the x_2-axis) and the local instantaneous coordinate system x, y, z for the flow (with instantaneous rotation about the z-axis) is shown in figure 24.

Two-dimensional slices can be taken normal to the transverse z direction as shown in figure 25(a) for the example of a spherical tumbler. Thus, we consider circular slices shown in figure 25(b) that are identical to those for a 2d circular tumbler, figure 14, except that the flowing layer thickness δ is a function of z in addition to x, and the flowing layer length L is a function of z instead of being constant.

The circular slice of the spherical tumbler has a radius $r(z) = \sqrt{R^2 - z^2}$ where R is the radius of the sphere and the origin of the coordinates is at the centre of the sphere. Here C is on the instantaneous axis of rotation, which is parallel to the transverse direction in the spherical tumbler in figure 25(a). The position of the free surface with respect to the instantaneous axis of rotation is H. Of course, the above approach and assumptions can be applied to any tumbler geometry and fill fraction where the flowing layer is connected throughout operation. Convex tumbler geometries (such as spheres and cubes) always meet this requirement.

Since the velocity at the free surface in each cross section orthogonal to $\boldsymbol{k}$ is proportional to the local length of the flowing layer in the slice and because there is negligible transverse flow between slices [175], the mass balance in a differentially small element of the thin flowing layer for a slice in a 3d tumbler is identical to that for the 2d case (assuming that the bulk density in the bed of solid body rotation and the flowing layer are equal and that the pseudo-steady-state approximation holds). Thus,

$$\frac{\partial(\bar{u}_x(x,z)\delta(x,z))}{\partial x} = v_y(x, -\delta(x,z), z)), \tag{29}$$

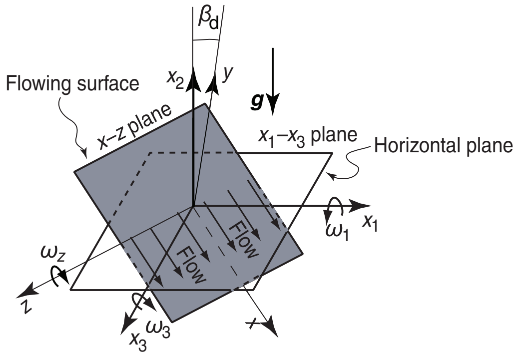

Figure 24. In the two-axis flows illustrated in figure 6, the free surface x–z plane is at the dynamic angle of repose, β_d with respect to the horizontal x_1–x_3 plane. Gravity $\boldsymbol{g}$ is orthogonal to the horizontal x_1–x_3 plane.

where the instantaneous coordinate system x, y, z is aligned with unit vectors $\boldsymbol{i}, \boldsymbol{j}, \boldsymbol{k}$.

Following a similar procedure to that for the 2d continuum model, it can be shown that

$$u_x(x, y, z) = \dot{\gamma}(\delta(x, z) + y) - \omega_z(H + y) \tag{30}$$

and

$$u_y(x, y, z) = -\frac{\omega_z x y}{\delta(x, z)}, \tag{31}$$

where

$$\delta(x, z) = \sqrt{\frac{|\omega_z|}{\dot{\gamma}}}\sqrt{(L(z))^2 - x^2} \tag{32}$$

and $L(z)$ is the distance between the midlength of the free surface and the tumbler wall in the direction of flow at the transverse position z.

Equations (30), (31) and (32) are identical to the 2d case (equations (5), (9) and (8)) except for the dependence on the position along the z direction. Again, the acceleration of gravity and its orientation with respect to the free surface do not play an explicit role in the model. Gravity drives the flow, but its orientation is of no consequence to the kinematical description of the velocity field.

Situations with rotation about all three axes can also be considered. In this case, the unit vector along the instantaneous axis of rotation would have a non-zero y component. However, at any instant in time, the free surface immediately adjusts so its normal vector is at angle β_d to the vertical direction x_2, and the transverse direction is horizontal and in the plane of flow. The transverse direction of the flow in the layer is not necessarily parallel to the instantaneous axis of rotation, because it can tilt out of the plane of the flow. Thus, the transverse direction is the horizontal projection of the instantaneous axis of rotation to the free surface. This is equivalent

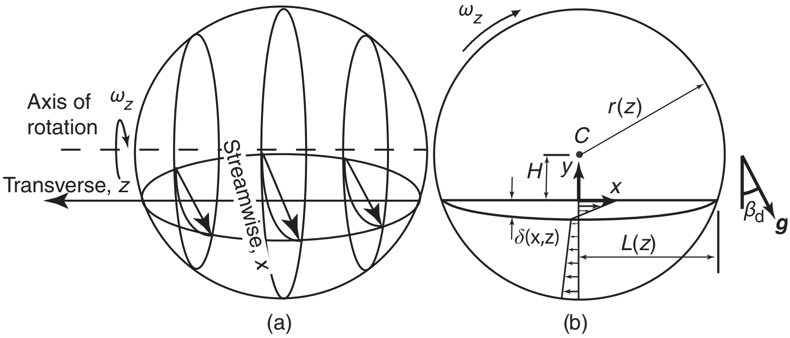

Figure 25. (a) 3d spherical tumbler of radius R with the transverse direction, z, parallel to the instantaneous axis of rotation, which is orthogonal to the streamwise direction x. (b) 2d slices can be taken along z. Each slice of radius $r(z)$ is rotated about C, which is on the instantaneous axis of rotation, at rotation rate ω_z, where $\omega_z < 0$ for clockwise rotation as shown. Vertical position of free surface relative to the axis of rotation is H. The distance between the centre of flowing layer and the tumbler wall is $L(z)$. The thickness of the flowing layer is $\delta(x, z)$.

to equation (26) for the definition of the unit vector along the axis of rotation in which the vertical component of rotation ω_2 is omitted. The streamwise direction x is orthogonal to z and at the dynamic angle of repose, β_d with respect to the horizontal x_1–x_3 plane according to equation (27). The outward normal y is found from the coordinate transformation of x_2 due to the dynamic angle of repose according to equation (28).

An example of this case is the rocking/rotating spherical tumbler studied by Gilchrist and Ottino [147]. In this case, a primary axis of rotation is rocked time periodically in and out of the horizontal x_1–x_3 plane. The flow was modelled in each 2d slice (as illustrated in figure 25) using assumption (C) of section 3.2, but similar results are obtained using the model adopted here (assumption (A) of section 3.2). In the model, L is a function of time due to the continual reorientation of the surface flow with respect to the tumbler axes.

The success of the continuum model is evident from comparison with experiments using two particle sizes shown in figure 26. In the case of a spherical tumbler rotated about a single axis with no rocking, a single segregated band forms at the transverse centre of the sphere orthogonal to the axis of rotation, analogous to the axial banding phenomenon in $2d+1$ cylindrical tumblers (figure 10). The appearance of the band as viewed from the bottom of the spherical tumbler is shown in part A of figure 26 (left-hand side). The resulting space–time plot of a narrow vertical strip of the image is also shown in part A of figure 26 (right-hand side). With no rocking the band stays centred in the tumbler over time. When the axis of rotation is rocked, time-periodic flow is induced resulting in the wavy space–time plot of the band of small particles, as shown in part B of figure 26.

The particle trajectories based on a continuum model of monodisperse particles with the same forcing as in part C of figure 26 show a remarkably similar instantaneous pattern and space–time plot by simply shading the trajectories near the centre portion of the tumbler. Similar results are obtained for a situation in which the rocking frequency and rotating frequency are not identical. In this case, spots of small particles appear twice per rotation in the experiments (part D of figure 26), which correspond to light areas in the continuum model (part E of figure 26).

One more study should be mentioned. Elperin and Vikhansky proposed a model for flow in an ellipsoidal tumbler that is rotated about a main axis that is also wobbled [200]. They showed that rotation of a 3d tumbler about its non-principal axis can enhance transport in the axial or spanwise direction. They later used level-set methods to define the free surface of flowing granular material for various 3d tumblers [201]. The rocking of a rotating cylindrical tumbler has also been studied experimentally [148–151, 202], but clearly much more work is needed in this area.

6. Applications to 3d + T systems

Here we consider the discrete two-axis motion of a 3d tumbler. This system is of particular interest because it serves to illustrate several analysis techniques that are useful to reveal the relationship between the dynamics of the underlying flow and segregation. As shown for the $2d+T$ case, the computational Poincaré sections

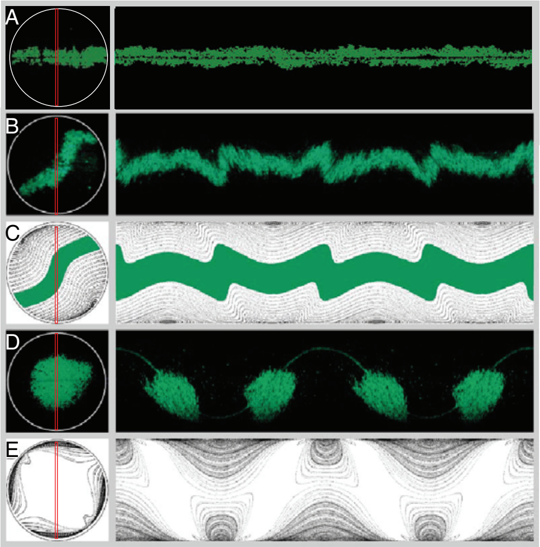

Figure 26. S_2-DGS experimental space–time plots (A, B and D) and computational continuum model space–time plots (C and E) of the bottom view of the spherical tumbler. Left: Static pictures of a bottom view of the spherical tumbler. Right: Space–time plots from experiment and continuum model. A vertical line of pixels (represented by the horizontal line in static images on left) are taken from each frame of consecutive pictures in time captured by a video camera to create the space–time plots. A, Experimental, no rocking. B, Experimental, ratio of rocking frequency to rotating frequency of 1.0 with rocking angle of $\pm 45^\circ$. C, Computational, same parameters as B. Centre trajectories are shaded for clarity. D, Experimental, ratio of rocking frequency to rotating frequency of 0.842 with rocking angle of $\pm 45^\circ$. E, Computational, similar parameters as D. Ratio of rocking frequency to rotating frequency of 0.957. Rocking angle of $\pm 45^\circ$. In the experiments, the large painted black glass particles are 2.0 mm in diameter and the small fluorescent particles are 0.8 mm in diameter. The acrylic spherical tumbler has a diameter of 136 mm. Reprinted with permission from [147]. © 2003 American Physical Society.

capture the time-periodic dynamics of the underlying flow. Poincaré sections are useful in revealing the structure of the flow, including where there is mixing and where there is not. The analysis has an analogue in 3d + T systems. However, there are few available theoretical tools and methods for analysing these systems, one of the few analyses being the flow skeleton concepts of MacKay [203] (see also [204]). The 2d + T systems benefit from ease of experimental visualization. In a 2d case, the effects of time-periodic rotation rates, tumbler geometry and segregation can be viewed easily. However, in the 3d case, the effects of these factors are not easily captured owing to the opacity of the granular material and the challenge in representing 3d systems in a 2d image. Even in fluids, where the interior of a 3d system is more easily viewed, the dynamics are much more complicated than for a 2d system; the flow around periodic points is considerably richer and there is no agreement as to the best way to visualize the internal structure of the flows (the steady 3d case is relatively simple; the 3d + T case is not) [204, 205].

The set of rotations and resulting flows shown in figure 27 lends itself to a symmetries analysis technique based on map algebra, which was first developed by Franjione and Ottino [191] in the early 1990s for 2d and spatially periodic fluid flows. With the exception of work by Galaktionov *et al.* [206] it has not been applied to mixing in 3d flows. Nevertheless further application and development of this technique can greatly aid in the understanding of 3d systems. In particular, it can reveal the placement of invariant regions of the flow and simplify considerably the numerical procedures needed to locate unmixed regions.

6.1. *Symmetries in time-periodic flows*

Map algebra techniques are ideally suited to the analysis of mixing generated by a series of piecewise actions. For illustration purposes, consider the two-axis motion of a three-dimensional tumbler geometry such as a sphere (figure 27) rotated discontinuously about each of the axes [112]. Consistent with the assumptions made earlier, there is no flow in the transverse direction allowing analysis of flow in 2d slices along the axis of rotation. In the case of a sphere, each cross-sectional slice is a circle (as shown in figure 27).

Specific details of the flow are not required for the application of the symmetries technique. Only the basic behaviour of the motion is needed, so the analysis applies to both the two-axis spherical tumbler and the two-axis cubical tumbler.

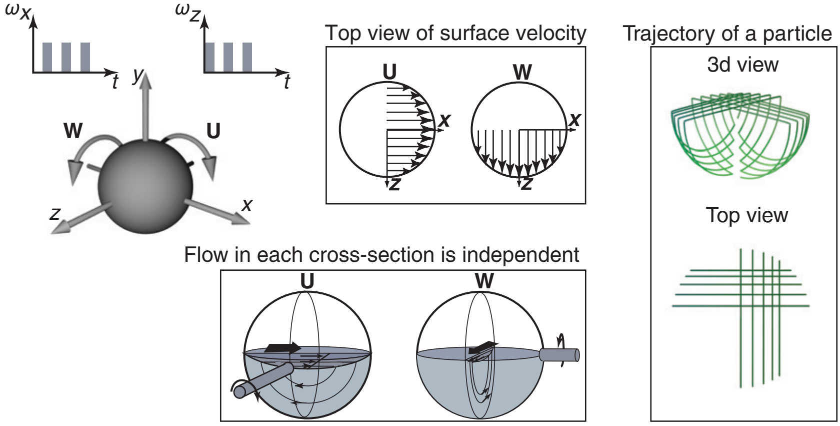

Figure 27. Rotation of a spherical tumbler on two independent axes of rotation. After rotating the tumbler from horizontal to the dynamic angle of repose, there is a rotation for a given time period about the z-axis that results in a surface flow in the positive x direction, $\mathbf{U}$. After this motion has stopped the tumbler is gently rotated in reverse by the dynamic angle of repose to bring the surface back into the horizontal plane. Then there is a rotation for the same time period about the x-axis resulting in a surface flow in the positive z direction, $\mathbf{W}$. Then the tumbler is gently rotated in reverse by the dynamic angle of repose to bring the surface back into the horizontal plane. This protocol can then be repeated for the desired number of periods. Flow in slices perpendicular to the axis of rotation are independent 2d flows. The right portion illustrates the trajectory of a particle seeded at $(0, -0.95R, 0)$ over five iterations of the two-axis protocol, $\mathbf{M} = \mathbf{WU}$. The distance of rotation on each axis is one-half rotation.

The symmetries technique is most easily explained by demonstrating its application to a particular tumbler rotation protocol, in this case a *two-axis protocol* (also known as the *biaxial protocol* [112]), a discrete mixing protocol where first the tumbler is rotated about one axis for a specified angle and then rotated at the same rate about a different axis for the same angle. In experiments, the surface always starts from horizontal and is rotated without causing flow by the dynamic angle of repose before applying the specified rotation. After the specified rotation, the tumbler is rotated backwards for the dynamic angle of repose in a manner that does not result in flow to return to horizontal before applying rotation around the other axis.

From this point on, we alter the notation for convenience to avoid carrying too many subindices. First, x_1 and x_3 labelling the axes about which rotation occurs in figure 6 are replaced with x and z as shown in figure 27. These axes remain in the horizontal plane. The resulting surface flows are **U** and **W**, respectively, as shown in figure 27. The first action results in flow in the layer in the positive x direction, **U**. The second action results in flow in the layer in the positive z direction, **W**. This alternating rotation protocol could be repeated in a time-periodic way, as indicated in the upper left portion of figure 27. Note that the dynamic angle of repose can be neglected if the tumbler is rotated gently from horizontal to the angle of repose before each action and back after each action, so that the particles do not flow. The trajectory of a particle over five periods of the two-axis protocol is shown in the right portion of figure 27.

For the example application of the symmetries technique, action **U** (one-half rotation about the z-axis) is followed by action **W** (one-half rotation about the x-axis). The composition can be expressed as a map, $\mathbf{M} = \mathbf{WU}$. The right-hand side of the map is read right to left. **M** is a representation of $\boldsymbol{x}_{n+1} = \boldsymbol{\phi}(\boldsymbol{x}_n)$, which is the solution to the velocity field described by the continuum model for **U** followed by **W** mapping the point $\boldsymbol{x}_n$ to $\boldsymbol{x}_{n+1}$. That is:

$$\boldsymbol{x}_{n+1} = \mathbf{M}\boldsymbol{x}_n. \tag{33}$$

Periodic points of period j correspond to the solution of

$$\boldsymbol{p} = \mathbf{M}^j\boldsymbol{p}. \tag{34}$$

In two dimensions, periodic points are elliptic (complex conjugate eigenvalues), hyperbolic (real eigenvalues) or parabolic (eigenvalues of ± 1). As we shall see, 3d flow presents far richer behaviour [207–210].

6.2. *Periodic point location*

An algebra of symmetries analysis reveals that the overall map **M** is two iterations of a fundamental map $\mathbf{M}_\mathrm{f}$. This fundamental map has a time-reversal symmetry (described in Appendix A) that indicates period-1 points lie in the $x = -z$ plane or in pairs reflected across it. We are interested in period-1 points because the lowest-order points tend to be associated with the largest islands and therefore have the most influence on the region of flow near them [185].

As an illustration, consider the application of the two-axis protocol to a spherical tumbler illustrated in figure 27. (A similar study of a cubical tumbler is described in Appendix B.) Insight into the nature of the period-1 points in a spherical tumbler can be obtained from an understanding of the period-1 points in a 2d circular tumbler. For a protocol where the period is arbitrarily set at one-half revolution and $\dot{\gamma} = 200|\mathrm{w}|$, there is a curve of parabolic period-1 points, shown in figure 28(a), at $r = 0.54R$ where R is the radius of the circular tumbler. For rotation of a sphere by one-half revolution about one axis, each cross-sectional slice of the sphere will have a corresponding curve of period-1 points. Combining these slices results in a surface of period-1 points. For a two-axis protocol, there are two of these surfaces that are orthogonal to each other, as shown in figure 28(b). The blue surface comprises period-1 points due to rotation about the z-axis. The yellow surface illustrates the surface of period-1 points due to rotation about the x-axis. Thus, for a two-axis protocol $\mathbf{M} = \mathbf{WU}$ with each action being a rotation of one-half revolution, curves of period-1 points will be at the intersections of these surfaces [112]. To be precise, these periodic points are period-$\frac{1}{2}$ points because they return to their initial location after one-half iteration of the map, $\mathbf{M}$. However, for simplicity, we refer to these periodic points as period-1 points, because they are also periodic after one iteration of the map, $\mathbf{M}$.

6.3. *Skeleton of 3d flow*

The skeleton of a steady 3d flow or a 3d + T flow resides in the identification of fixed points and cycles. There is significantly more richness in the structures in 3d flows than in 2d and 2d + T flows. The 2d flows cannot be chaotic but 2d + T can be. In 3d, chaos is possible in steady flows, and it often occurs in 3d + T flows. For examples of 3d chaotic fluid flows the reader may consult [204, 205]. Much has been written about the 3d case, although often without the restriction that the flow be volume preserving. An introduction to this topic can be found in the book by Hirsch and

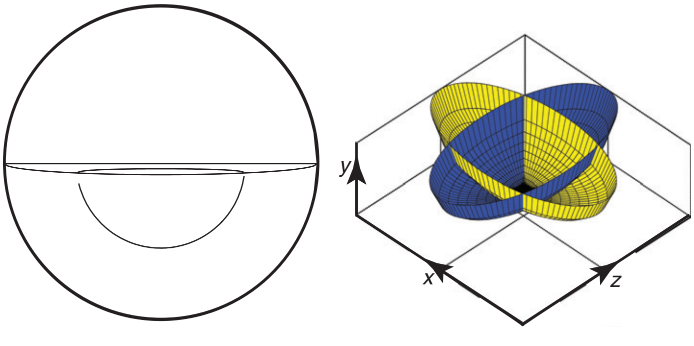

(a) (b)

Figure 28. Periodic point curves and surfaces. (a) Curve of period-1 parabolic points in a rotating 2d circular tumbler. The curve is continuous in both the bed of solid body rotation and the flowing layer. The discontinuity in the curve at the boundary of the bed of solid body rotation and the flowing layer is a result of computational challenges near the boundary. (b) Schematic of surfaces of period-1 parabolic points in rotating sphere. The blue surface is due to $\mathbf{U}$. The yellow surface is due to $\mathbf{W}$. These surfaces are only illustrations, not based on calculations like in (a). The surface in the flowing layer is not shown. This type of analysis was first made by Gilchrist [112]. See online version for colour.

Smale [207], in the series of books by Abraham and Shaw [211] and in the book by Ottino [181]. A classification of critical points in 3d systems is given in the article by Chong *et al.* [209] and an analysis of the skeleton of 3d systems is given by MacKay [203]. The 3d + T case is richer. Mathematically, the problem of 3d + T granular flows is identical to that of 3d + T fluid flows, although there are a few limit cases, such as a vanishingly thin layer in the case of granular flows, that bring about interesting mathematical consequences that have not been studied yet.

In what follows we present an example analysis of a flow in a spherical tumbler to give the reader a sense of the structure of chaotic 3d + T granular flows. The first step in the analysis involves the location of periodic points. Once a period-n point is located, its eigenvalues can be calculated from the Jacobian matrix of the linearized mapping of the flow around the point [206, 212, 213]. In the case of the two-axis protocol, the linearized mapping **M** is used to compute the Jacobian matrix, **J**, in an analogous manner to that for the 2d Jacobian matrix [182]. The eigenvalues are then calculated from $\det(\mathbf{J} - \lambda\mathbf{I}) = 0$, where **I** is the identity matrix. When the flow is 3d and volume preserving, there are three eigenvalues such that $\lambda_1\lambda_2\lambda_3 = 1$. Note that in the 2d + 1 case there is no flow in the transverse direction, so there will only be two non-zero eigenvalues such that $\lambda_1\lambda_2 = 1$.

With the eigenvalues and the Jacobian matrix in hand, the corresponding eigenvectors can be found. If one of the eigenvalues is equal to ±1, then its eigenvector points in the direction that characterizes shear flow and towards another periodic point. This eigenvector is tangent to a curve of periodic points much like the curve of parabolic points at $r = 0.54R$ in the 2d steady flow of a circular tumbler rotated at a constant rate. For the discrete two-axis protocol in a sphere of radius $R = 0.5$, the curve of period-1 points, each with one eigenvalue equal to one, are shown in figure 29. The positions of these period-1 points are located numerically as follows. A cube-shaped grid of points (three points on each edge separated by a small spacing) is seeded in the vicinity of an expected location of a period-1 point. These points are advected using the continuum model for one period of flow. A new grid with a smaller spacing is then constructed around the point that moved the smallest distance from its initial position, and the process continues until the point that returns to its initial position within some tolerance is identified. Using this approach, curves of period-1 points in the $x = z$ plane and the $x = -z$ plane are found, as predicted by the intersection of the surfaces in figure 28 and by the symmetries analysis technique. These curves are continuous and connected through the flowing layer (although it is computationally difficult to calculate points near the interface of the flowing layer and the fixed bed). Individual points represent the resolution of the calculations.

If the other two eigenvalues are complex conjugates, that is, $\lambda_{2,3} = A \pm \mathrm{i}B$ where $B \neq 0$, then the periodic point has a twist and 'elliptic' character. If these elliptic points lie on a curve, they should result in a tube-like structure, the 3d analogue of the ellipse-shaped rings in two dimensions such as the islands shown in figure 20(c). Points that are initially seeded in this tube-like region should remain trapped in this neighbourhood owing to the elliptic nature of the periodic points. If both eigenvalues are real (imaginary components are zero), not equal to one and reciprocals of each other, then the periodic point is 'hyperbolic' in nature. The character of the periodic points in figure 29 is emphasized through colour. The colour depends on the

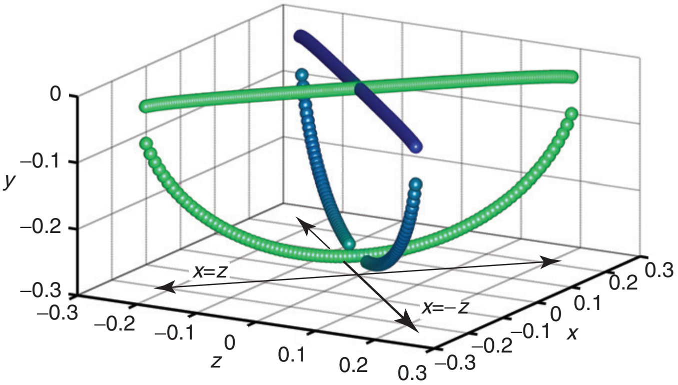

Figure 29. Period-1 points in a sphere rotated according to $\mathbf{M} = \mathbf{WU}$. In the model used to generate these results $\dot{\gamma} = 200|\omega|$. The colour depends on the magnitude of $|B|$, where $B = 0$ is represented by green and $B \neq 0$ is represented by blue. All of the points in the $x = z$ plane, both in the fixed bed (the lower curve) and in the flowing layer (the upper line), are hyperbolic, $B = 0$. The period-1 points in the $x = -z$ plane are elliptic, both in the fixed bed and in the flowing layer. Exceptions occur at the centre of the flowing layer, where the curve of period-1 points in the $x = -z$ plane intersects the curve of hyperbolic period-1 points in the $x = z$ plane and at the intersection of the two curves of period-1 points in the fixed bed. Here the period-1 points are parabolic. The magnitudes of B for the elliptic points in the bed are small compared with the magnitudes of B for elliptic points in the flowing layer, as indicated by their lighter blue colour. See online version for colour.

magnitude of the imaginary part, $|B|$, where hyperbolic ($|A| \neq 1$, $B = 0$) and parabolic ($|A| = 1$, $B = 0$) points are represented by green. Elliptic points ($B \neq 0$) are represented by blue.

6.4. *Three-dimensional Poincaré sections*

Visualization in 2d + T systems is accomplished by means of Poincaré sections [19, 87, 88]. Here the framework for 2d + T systems is expanded to a 3d stroboscopic map. Two approaches are considered.

The first approach involves seeding points (here along the $x = -z$ plane) at a particular radius and then plotting the location of the points after each iteration of the map, $\mathbf{M}$. Poincaré sections of curves of 19 points initially seeded at a constant radius in the $x = -z$ plane and then advected over 500 periods of flow are shown for the three different radii (where the radius of the spherical tumbler is $R = 0.5$) in figure 30. All of the points in each case remain on the hemispheres of constant radius on which they were initialized for all iterations. This is analogous to the flow occurring along closed streamlines in 2d circular tumblers. In the spherical tumbler, flow in the flowing layer occurs on closed streamlines first in the positive x direction due to $\mathbf{U}$ and then in the positive z direction due to $\mathbf{W}$. Thus, in the case of the two-axis sphere rotated for the same period of time on both axes, particles travel on constant radii hemispheres shown on the left-hand side of figure 30 that are formed by the intersections of the closed streamlines in each 2d circular slice along the axis of rotation.

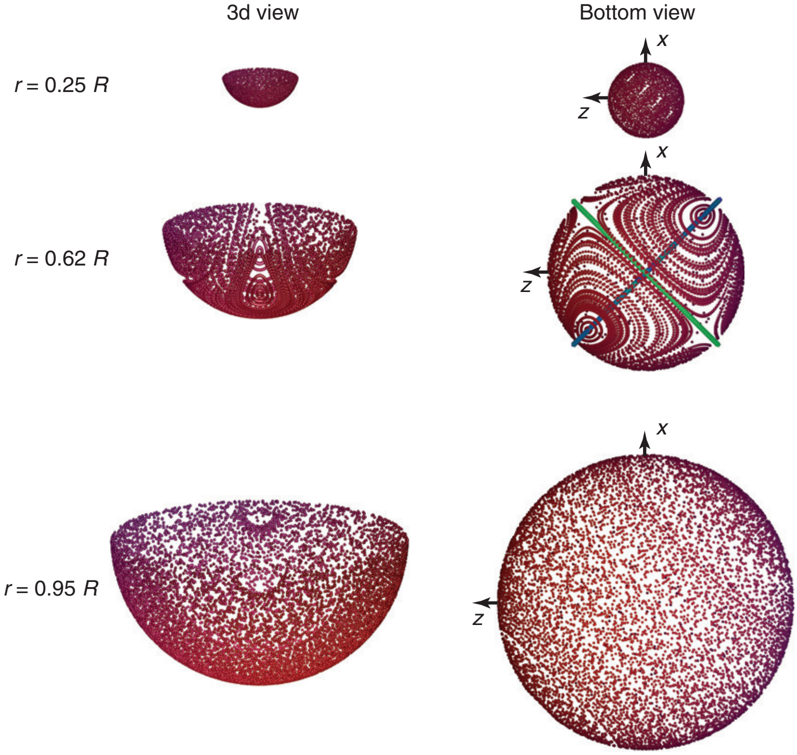

Figure 30. Poincaré sections for two-axis protocol in a spherical tumbler. In the model used to generate these results $\dot{\gamma} = 200|\omega|$. Left: 3d views show that points initially seeded to a hemisphere stay on that hemisphere. Right: Bottom views show $x = -z$ symmetry. Top: Points initially seeded at $r = 0.25R$ where R is the radius of the sphere. Middle: Points initially seeded at $r = 0.62R$. Bottom: Points initially seeded at $r = 0.95R$. The ellipse shaped rings in the upper right and lower left of the bottom view of the $r = 0.62R$ hemisphere correspond to the intersections of the curve of elliptical points (shown in figure 29) in the $x = -z$ plane with the $r = 0.62R$ hemisphere. This is analogous to the ellipse-shaped rings in the 2d + T case, such as those shown in figure 20(c). Likewise, the hyperbolic nature of the system in the upper left and lower right of the bottom view of the $r = 0.62R$ hemisphere reflect the curve of hyperbolic points in the $x = z$ plane interacting with points on the hemisphere. The pattern is symmetric about the $x = z$ plane and the $x = -z$ plane, as is expected from the symmetry of the curves of period-1 points in figure 29.

The seeded points interact with the curves of period-1 points resulting in patterns visible when viewing the bottom of the hemispherical Poincaré section for $r = 0.62R$ shown on the right-hand side of figure 30. Elliptic and hyperbolic behaviours are evident near the intersections of the hemisphere with the curves of period-1 points. Even though the dynamics are primarily governed by the period-1 point curves, patterns also occur in the Poincaré sections of the hemispheres that do not intersect the period-1 point curves, as shown for $r = 0.25R$ and $r = 0.95R$.

A second approach for visualizing the dynamics of the underlying flow is shown in figure 31. The idea is to identify chaotic and non-chaotic regions of the flow near the curves of period-1 points. Points are seeded in the middle of each quadrant of the lower half of the spherical tumbler as perpendicular square sheets. After a number of applications of **M**, only the points that have travelled a relatively small distance from their initial location after each iteration are retained in the plot.

In the upper right portion of figure 31, tubes of trapped points circulate around the curves of elliptic points indicating regions of poor mixing, much like the islands associated with elliptic points in 2d + T systems. The points in the lower right portion of figure 31 move away from the curve of hyperbolic points in the $x = z$ plane. These results are consistent with those in figure 30 for $r = 0.62R$, where points move away from the $x = z$ plane, and ellipse-shaped rings analogous to 2d islands form along the $x = -z$ plane.

6.5. *Comparison of the 3d continuum model with experiments*

The continuum model provides an alternative approach for the study of the dynamics in a spherical tumbler undergoing the two-axis protocol. For the results shown in figure 32, the two-axis protocol, **WU**, is applied with one full rotation on each axis. The shear rate is matched to that for the comparable experiment ($\dot{\gamma} = 50|\omega|$), so it is different from that used to obtain the computational results shown in figures 29–31. The hemisphere of interest in figure 32 is close to the tumbler wall ($r = 0.95R$). While the medium in the continuum model simulation is assumed to be monodisperse, in the experiment, two sizes of particles are used. The fluorescent yellow (they appear green in the figure) tracer particles are 1.94 ± 0.11 mm painted glass particles (density of $2.3\,\mathrm{g\,cm^{-3}}$), while the remaining particles are 1.07 ± 0.04 mm black basalt glass particles (density of $2.6\,\mathrm{g\,cm^{-3}}$). By using large tracer particles, segregation effects keep these particles in the uppermost portion of the flowing layer and thus on the outer most hemisphere when they are in the bed of solid body rotation (near the tumbler wall). This counters diffusive mixing between hemispheres that would normally occur as a result of the particles passing through the flowing layer, so that the advective mixing on hemispheres can be readily observed. Clearly, the continuum model simulation provides an accurate representation of the dynamics of the mixing, particularly when the simulation includes diffusion. The chaotic dynamics are evident in the stretching and folding of the ‘blob’ of fluorescent tracer particles as is evident after four periods of the protocol. Furthermore it is clear that the dynamics are restricted to hemispherical shells, as described in the previous section.

6.6. *Segregation modelling in three dimensions*

The segregation pattern for a bidisperse granular material is closely related to the underlying dynamics of the flow as described in section 3.5.4. The constitutive model for segregation can be extended to 3d systems and applied to both a spherical tumbler and a cubical tumbler rotated at its faces according to the two-axis protocol **M**.

In what follows, the advective motion is restricted to 2d slices perpendicular to the axis of rotation. The 3d segregation model is based on equations (23)–(25) for a 2d segregating flow consisting of two species h (heavy) and l (light). In a 3d geometry with streamwise direction x (for the example of **U**), assuming that the shear rate $\dot{\gamma}$ is

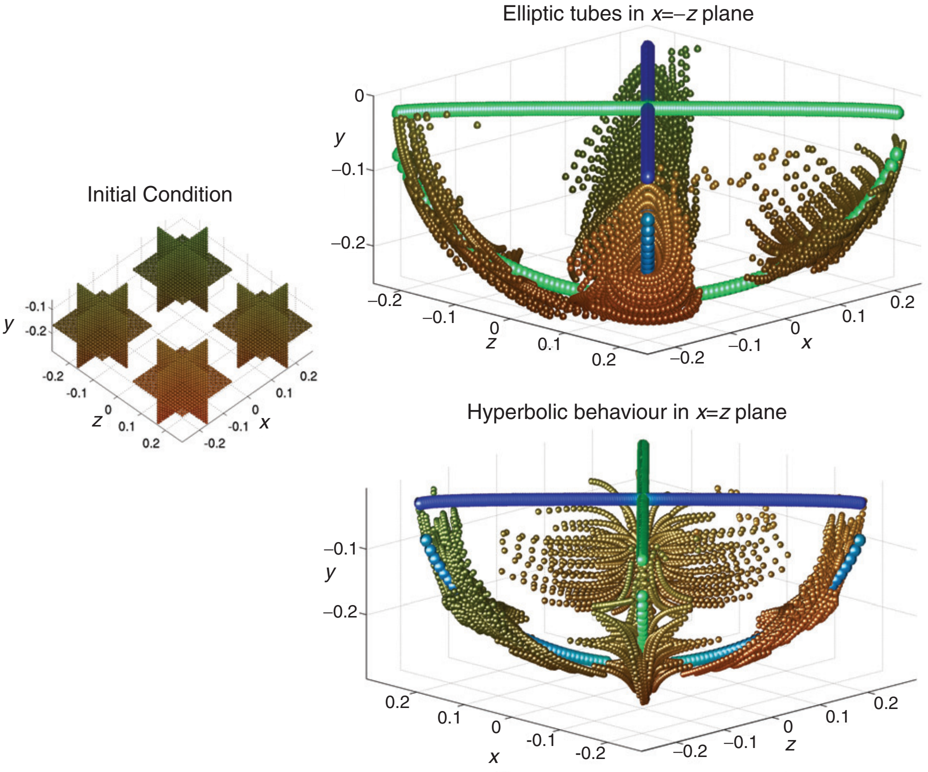

Figure 31. To visualize the dynamics of the chaotic flow, three orthogonal sheets of points are seeded in each quadrant of the lower half of the spherical tumbler (Initial condition). The position of a point after each of the 20 periods of **M** is recorded and the average distance between the positions is calculated. This is repeated for each of the points initially seeded in the tumbler system and the median of these averages is calculated. Sets of positions from the 20 iterations corresponding to each initial point are plotted only if the average distance between the positions is smaller than some threshold, in this case, smaller than half of the median of the average distances between points for all of the initial conditions. Upper right: Points that are trapped in tube-like regions around the ‘elliptic’ point curve in $x = -z$ plane. Lower right: Points reveal hyperbolic behaviour in the $x = z$ plane. In the model used to generate these results $\dot{\gamma} = 200|\omega|$.

constant and noting that the flowing layer thickness δ depends on the position along the transverse direction, z, the streamwise velocity of both heavy and light particles is

$$u_{x,\mathrm{h}} = u_{x,\mathrm{l}} = \dot{\gamma}(\delta(x,z) + y) - \omega_z(H + y) + k_x. \tag{35}$$

The normal velocity for heavy particles is

$$u_{y,\mathrm{h}} = -\frac{\omega_z x y}{\delta(x,z)} - 4\frac{D_{\mathrm{coll}}}{d_{\mathrm{p}}}\left(\frac{m_{\mathrm{h}} - m_{\mathrm{l}}}{m_{\mathrm{h}}}\right)(1 - f) + k_y, \tag{36}$$

and the normal velocity for light particles is

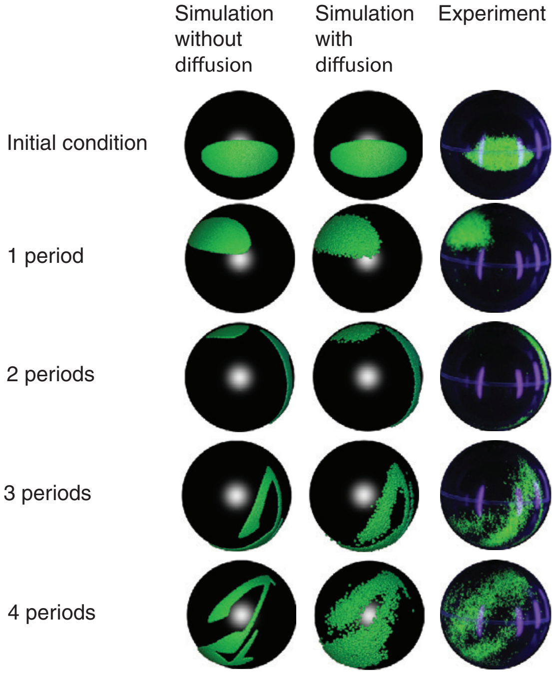

Figure 32. Comparison of a simulation using 3d continuum model without and with diffusion and an experiment. These figures were generated using the two-axis protocol **WU** where the rotation on each axis is one revolution. By tuning the shear rate in the model to match the experiment ($\dot{\gamma} = 50|\omega|$), the continuum model simulation captures the patterns observed experimentally. In both the simulation and experiment, fluorescent yellow (appear as green in the figure) coloured particles are seeded in a blob at the bottom of a half-full spherical tumbler. In all cases, the spherical tumbler is viewed from the bottom. The first column illustrates the evolution of the pattern over four periods of the two-axis protocol using the continuum model without diffusion. The second column illustrates the evolution of the pattern over four periods of the two-axis protocol using the continuum model with diffusion in the flowing layer in both the x and z directions. The third column shows the experimental result of a half-full sphere (diameter of 136 mm) containing 1.07 ± 0.04 mm black basalt glass particles and 1.94 ± 0.11 mm fluorescent yellow painted glass particles. The rotation rate is 2.0 RPM. Segregation effects keep the larger tracer particles near the tumbler walls and away from the interior of the bed. Thus, size differences negate diffusive motion of particles between hemispheres to capture the dynamics restricted to hemispheres, as shown in figure 30. See online version for colour.

$$u_{y,1} = -\frac{\omega_z xy}{\delta(x,z)} + 4\frac{D_{\mathrm{coll}}}{d_{\mathrm{p}}}\left(\frac{m_{\mathrm{h}} - m_{\mathrm{l}}}{m_{\mathrm{h}}}\right)f + k_y. \tag{37}$$

These equations are similar to those for 2d segregation, except that the instantaneous streamwise and transverse coordinates are used along with the rotation rate about the instantaneous axis of rotation, $\omega_z = -|\omega|$. In addition, the flowing layer thickness is a function of both x and z. The terms k_x and k_y are white noise terms that represent diffusion in the streamwise direction x and the upward normal direction y.

Since there is the possibility for diffusion along the transverse direction, an additional equation is included

$$u_{z,\mathrm{h}} = u_{z,1} = k_z \tag{38}$$

where k_z is a white noise term related to collisional diffusivity in the transverse direction analagous to k_x and k_y. Typically, diffusion in the transverse direction can be taken to be the same order of magnitude as the diffusion in the streamwise direction. Experimental measurements using particle tracking velocimetry indicate that fluctuations about the mean velocity in the surface flow in 3d tumblers are similar in both the streamwise and transverse directions [175]. Analogous equations for action **W** would interchange the roles of x and z in equations (35)–(38).

6.6.1. Two-axis spherical tumbler. The two-axis protocol serves as an example to demonstrate the application of the segregation model to a 3d system. Consider a half-full spherical tumbler with a ratio of tumbler diameter to particle diameter of 100 that contains 3.2×10^4 points representing heavy particles randomly seeded throughout the lower half of the tumbler as the initial condition. These particles were then advected according to equations (35)–(38). Light particles were not included in the simulation, and f was calculated using the bitwise operator method described in section 4.3.

For rotation about one axis, in this case, the z-axis (action **U**), the particles segregate into a core illustrated in figure 33(a). The core is largest at the centre of the sphere where the cross-sectional radius in the direction of flow is the largest. The core that forms after eight periods of the two-axis motion $\mathbf{M} = \mathbf{WU}$ has different symmetries than for one-axis motion as shown in figure 33(b). It is symmetric about the $x = z$ plane, although it is still roughly a radial core in terms of its general features.

6.6.2. Two-axis cubical tumbler. The two-axis cubical tumbler is more complicated than the spherical tumbler. (A detailed analysis of the underlying dynamics for a two-axis cubical tumbler is presented in Appendix B.) Recall that while in the 2d case, a circular tumbler results in a radial core of segregated small or dense particles (figure 18(b)), a square tumbler results in a core with two lobes that stretch along the diagonals (figure 18(d)). Likewise, in three dimensions, the two-axis cubical tumbler results in a more complicated segregation pattern.

In this case, 6.0×10^4 points representing heavy particles were initially seeded uniformly throughout the lower half of the cubical tumbler. After applying eight periods of the protocol $\mathbf{M} = \mathbf{WU}$, the heavy particles segregate into a three-lobed pattern, as shown in figure 34(a). These results can be compared with segregation experiments using a S_2-DGSs (dry) and a S_2-LGSs (liquid). As shown in figure 34, the computations and experiments agree in many respects. In all cases, three lobes are observed. There are two lobes in the positive z half-space, one above the z-axis and one below, and a single lobe in the negative z half-space of the cubical tumbler. Furthermore, in both the model and the experiments, a 'hole' containing fewer particles than the lobes is observed between the three lobes. Thus, the segregation model qualitatively predicts the nature of the segregation pattern.

The segregation pattern is produced by two effects. First, the particles segregate in the flowing layer with the small or dense particles sinking to the bottom portion

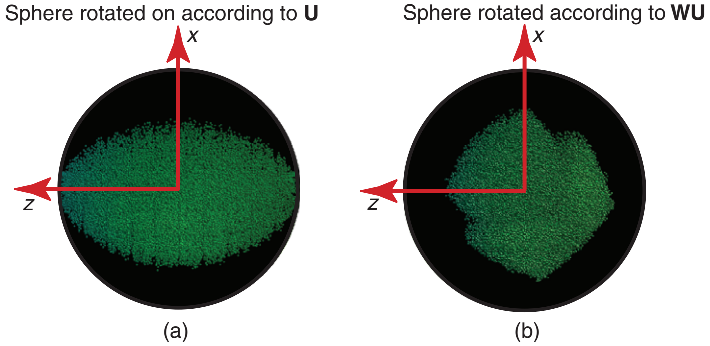

Figure 33. Example of the 3d segregation model applied to a spherical tumbler. Both figures are of the bottom view with the y-axis pointing into the page. (a) Segregation pattern of 3.2×10^4 points representing dense particles after four revolutions on the z-axis (eight periods of **U** where the time period is one-half revolution). (b) Segregation pattern of 3.2×10^4 points representing dense particles after four periods of the protocol $\mathbf{M} = \mathbf{WU}$. In the model used to generate these results $\dot{\gamma} = 200|\omega|$. The ratio of the spherical tumbler diameter to a particle diameter is set to 100/1.

of the layer. Second, the flowing layer length and thickness change with the rotational orientation of the tumbler geometry. The flow in the layer is thus time periodic owing to the time periodicity of the rotational orientation. These time periodic dynamics drive the shape of the unstable manifolds (described in Appendix B), which trace out different regions of the flow, one of which corresponds to the segregation pattern. The overlay of the unstable manifold after over 20 periods of the flow with the corresponding computational segregation pattern is shown in figure 35. Thus, the continuum model can be used to predict the segregation pattern by means of unstable manifold tracing even though the continuum model contains no information about particle properties or their tendency to segregate.

7. Concluding remarks

7.1. *Summary of elements*

In this article we have presented a dynamical systems approach for mixing and segregation of polydisperse granular materials in rotating tumblers. Tumbler geometry and rotational protocol combinations are seemingly limitless and, until recently, there has been no unified framework for studying how these parameters affect mixing and segregation. While the flow of granular materials in rotating tumblers can appear to be quite complicated owing to the nature of time-periodic forcing, non-circular tumbler geometry and multiple axes of rotation, there is one point of simplification. To a good approximation, all of the dynamics occur in a thin, rapidly flowing surface layer. With an understanding of the flow in this layer, the dynamics of the entire system can be studied. While the continuum model was originally developed for 2d and 2d + T systems, it can be adapted to 3d and 3d + T systems

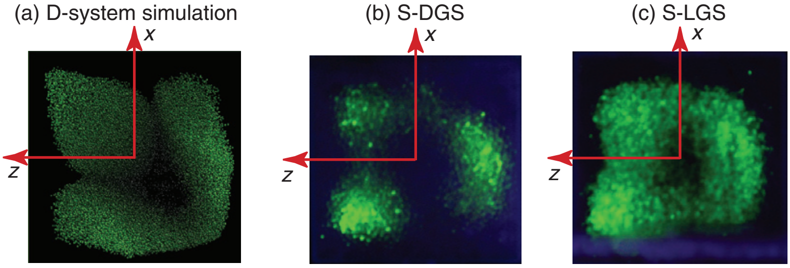

Figure 34. Comparison of simulation and experiments for segregation in a two-axis cubical tumbler. (a) Bottom view of D-system simulation of 6.0×10^4 points representing heavy particles after eight periods of the two-axis protocol. Here $\dot{\gamma} = 200|\omega|$. The ratio of the cube side length ratio to the diameter of a particle is set to 100/1. (b) Bottom view of the S_2-DGS experiment. (c) Bottom view of the S_2-LGS experiment. In (b) and (c), the cube has a side length of 100 mm. The cube is half filled with a 25% by volume small particle mixture. The experiments were run for several periods (20 or more, although a steady-state pattern developed within 8–10 periods). In both the S_2-DGS and S_2-LGS experiments, the small particles are 1.13 ± 0.07 mm painted fluorescent yellow (appears green under UV light) glass particles (bulk density 2.2 g cm^{-3}). The large particles are 3.03 ± 0.11 mm clear glass particles (bulk density 2.4 g cm^{-3}). The S_2-DGS experiment requires a larger concentration of small particles than that for the simulation, because the opacity of the granular material prevents the segregation pattern in the bed with a smaller concentration of small particles from being viewed. In the case of the S_2-LGS experiment, a 67% by weight sodium iodide solution is used to match the index of refraction of the large clear glass particles allowing a deeper view into the bed. See online version for colour.

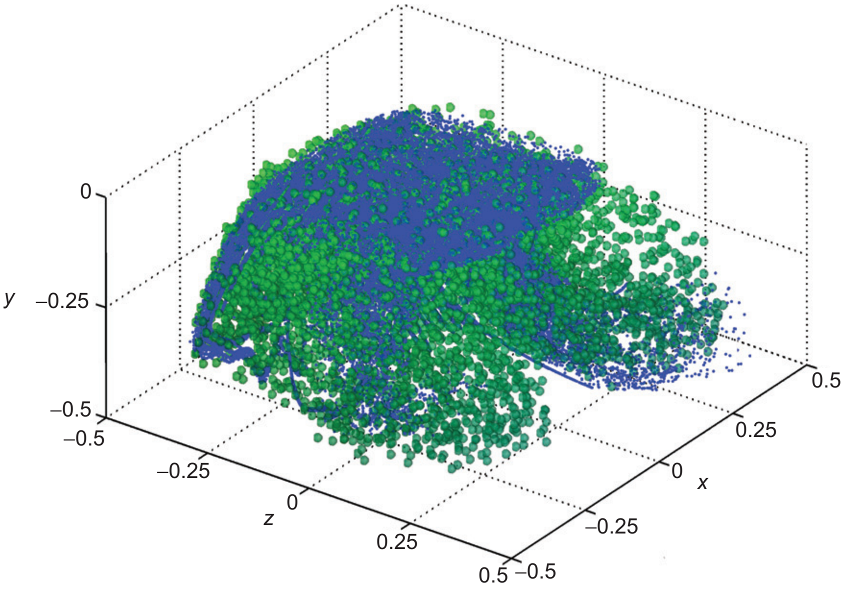

Figure 35. Overlay of unstable manifold tracing over 20 periods (shown in blue) with the segregation pattern from the computational model after eight periods (green spheres). Both results generated using $\dot{\gamma} = 200|\omega|$. See online version for colour.

by considering the flow in individual cross-sectional slices [175] as shown in figure 25(a). From this viewpoint, 3d flows are made up of slices of 2d flows. Thus, the tools and techniques developed for 2d systems, such as the constitutive equations for segregation, can be applied to 3d systems.

In 2d + T systems, the underlying dynamics as revealed through computational Poincaré sections can be related to segregation patterns through the hyperbolic points and their corresponding unstable manifolds [182]. This insight provides a template for studying the relationship between the underlying dynamics of flow in 3d + T flows and the resulting segregation patterns observed through both constitutive segregation modelling and experiments. While in 2d + T systems locating periodic points is relatively straightforward, the dynamics are considerably more complicated in 3d + T systems. The symmetries technique provides a method for identifying regions of interest of the underlying dynamics of the flow. By identifying how periodic points are arranged in the flow, we can expect to find corresponding regions of good and poor mixing as characterized by 'hyperbolic' points and 'elliptic' points. By numerically calculating the properties of the periodic points, regions of interest such as unstable manifolds can be located and related to segregation patterns.

7.2. *Outlook*

Granular materials display a remarkable range of behaviours. The review presented in the previous pages focuses on a thin slice: that of mixtures of granular materials placed in containers that mix and or segregate when acted on by a series of rotational motions. More specifically, the coverage is restricted to systems that operate when the surface flow is in the rolling regime and when particles are non-cohesive. It could be argued that such a set of physical systems and operational conditions is small and that the accompanying theory is narrow, in the sense that the framework cannot easily be extended to other physical situations.

Such a view may be naive and an analogy with classical fluid mechanics may be instructive. Let us state first that a complete solution of the Navier–Stokes equations is only possible in limited circumstances. This is true in the case of a single fluid and is manifestly clear in the case of two fluids where the number of problems amenable to analytical study is small. It is now regarded as natural that fluid mechanics evolved into branches, each corresponding to a set of approximations: potential flow for flow away from boundaries, where viscous terms are dropped altogether; boundary layer flow; inertia-less flow for vanishingly small Reynolds numbers when one is dealing with very viscous fluids or systems at small scales, and so on. Then we have the branches of fluid mechanics: lubrication theory, wave analysis in shallow waters and many more. It is trivial to find conditions where each of these descriptions breaks down.

There is, however, little doubt about the value and content of such descriptions and indeed there are many books written about the subtleties, consequences and insights embodied in each of these approximations. It is up to the user to determine the circumstances under which each theory may or may not be applied to the specific problem at hand.

A similar situation occurs here. We have a self-contained description of mixing in 2d and 3d containers acted on by means of a series of rotational motions. The central tenet of the framework is the recognition that the bulk of the granular flow in a rotated container is in solid body rotation and that the essential aspects of the surface flow are, in general terms, independent of the geometry of the container. The model assumes that the surface flow adjusts instantly so the streamwise direction of the flow is orthogonal to the instantaneous axis of rotation. The framework works if the flow surface, at any time in the history of the flow, is convex. This means that the set of all points containing all line segments between each pair of points at the perimeter of the flow surface lie within the flow surface itself. However, there may be cases where the framework applies even if the flow surface is not convex. What is needed is that during the flow history, the particle's flow path between the starting wall and the ending wall is uninterrupted by intrusions. Thus, a given container may be analysable in terms of the present framework depending on the nature of the forcing.

The framework based on these key experimental observations applies to both LGSs and DGSs when the particles differ in size and density only moderately. This corresponds to the physical situation where the flow affects segregation, but segregation does not affect flow to any significant extent. The body of evidence, based on computational results to date, is that under this set of conditions, the results (such as the location of regular and chaotic regions or the final segregation patterns) are relatively insensitive to details such as the exact shape of the flow region, etc.

Several improvements are possible and many areas of possible investigation can be identified. However, there are also conditions that fall clearly outside this framework. We discuss these issues below.

Under the category of improvements, from simple to complex, we may list the conditions leading to the relaxing of the need for convex flow surfaces, improvements in the constitutive relations for segregation and conditions under which we can add some degree of coupling between segregation and flow. As developed, the theory and framework assume that the flow affects segregation, but segregation does not affect flow. Particles of varying density flow in the streamwise direction as if they were monodisperse according to equation (5). However, they segregate in the normal direction based on an equation that treats the two particle types as interpenetrating continua that separate based on density. As such, improvements are in the spirit of adding inertia to the viscous flow solution around a sphere in classical fluid mechanics.

The complexities embodied in the flow of granular matter in 3d containers can be glimpsed by looking at limit cases. Even when reducing the problem to an extreme level of idealization, the mathematical problems are anything but simple. One such case is the flow in 3d containers, such as a sphere, when the flow region becomes infinitely thin and the speed infinitely fast [214]. This brings up only issues associated with the geometry and the nature of the trajectories in what essentially is a map of the sphere onto itself. The mathematics associated with such transformations raise several open questions at the present time. In fact, only recently have there been applications of results associated with linked twist maps [215] to fluid flows; the same machinery is applicable to granular flows [214]. The extension of these tools to three dimensions is far from trivial although it is tempting to refer to the flows of figures 27 and 39 as generalized linked twist maps [216]. Studies along this line of thinking may yield insight into complex issues arising with the geometry and shape of invariant cores for tumblers that are more than half full.

More work can be done with continuous protocols such as the rocking/rotating protocol [147]. Symmetry analyses have been applied to continuous flows, not just discrete flows [217]. Everything that has been done here for the discrete $3d + T$ systems such as the two-axis protocol can be applied to a continuous system.

There are also issues that have to do with the mathematical formulation of the problem itself. Consider equations (35)–(37) for segregation in three dimensions. The system is, qualitatively, dissipative and, as such, one could think in terms of attractors and even possible theorems that would indicate when such attractors may exist. This may yield insight into two kinds of problems and the end results they lead to: those starting from a mixed state and leading to unmixed state; and those starting from an unmixed state and leading, in general, to a partially mixed system coexisting with unmixed structures.

One should also note the physical issues that, at the moment, fall outside the framework. SD-systems, the most common in applications, represent a challenge and there are significant difficulties in dealing with these systems. In bidisperse S- or D-systems in a quasi-2d tumbler, materials of smaller size or higher density tend to radially segregate toward the centre of the granular bed, while materials of larger size or lower density tend to segregate at the outer edges of the granular bed. Of course, it seems logical that if the mixture consists of small–heavy particles and large–light beads, the smaller particles will sink to lower levels in the flowing layer ending up in the segregated core because of the combined effects of both percolation and buoyancy. One would expect that in this case, the rate at which segregation occurs and/or the extent of final segregation would be greater than the cases when only size or density of the particles drives the segregation. Conversely, for large–heavy particles and small–light particles, one might expect that segregation could be minimized or even eliminated altogether because the percolation and buoyancy mechanisms oppose one another. However, the actual situation is much richer than this simple analysis suggests [66, 67]. In fact, a variety of segregation patterns can occur when buoyancy and percolation act together. In some cases, the standard semicircular segregation pattern occurs, but in other cases a streaked pattern results. On the other hand, either mixing or segregation can occur when buoyancy and percolation oppose one another.

Another physical issue is coarsening. Coarsening occurs in $2d + 1$ systems (figure 10(b)), but recent experiments indicate that coarsening occurs in 2d systems as well (figure 36); radial streaks, such as those in figure 9(b), coarsen [218]. As shown in figure 36, four radial streaks form from an initially homogeneous 40% by volume mixture of 0.35 mm small painted black glass particles and 1.11 mm clear glass particles after 10 tumbler revolutions. The four streaks gradually coarsen to just one streak over the next 180 tumbler revolutions.

The physical situations covered by the present theory and framework are admittedly restricted. It is apparent that there are many open issues. Yet further theoretical and experimental work may open the mixing arts to rigorous analysis.

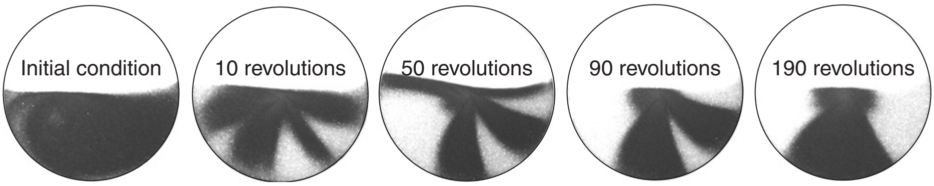

Figure 36. Example of radial streak coarsening. An initially homogeneous mixture of small 0.35 mm painted black glass particles and large 1.11 clear glass particles in a 55%-full quasi-2d circular tumbler quickly forms a radial streak pattern within 10 tumbler revolutions. The four radial streaks coarsen to just one streak over the next 180 tumbler revolutions. The tumbler is made of acrylic. The tumbler diameter is 200 mm and the thickness is 6 mm.

Acknowledgements

We gratefully acknowledge the support of the Office of Basic Energy Sciences of the Department of Energy, which funded much of our work described in this article. The first author also acknowledges support by a National Science Foundation Graduate Research Fellowship.

Appendix A: Symmetry concepts for 3d granular flows

The algebra of symmetries technique used in section 6 is based on the concepts outlined for fluid systems by Franjione and Ottino [191]. The analysis based on this technique reveals the arrangement of period-1 points in figure 29 and is described in appendix.

A1. *Definitions*

In this section we collect a few definitions before going into applications. An *action* is the consequence of a motion of the tumbler that causes the granular material to flow. Examples of actions are the operations **U** and **W** described earlier: **U** is one-half rotation of the tumbler about the z-axis where material flows in the layer in the x direction; **W** is one-half rotation of the tumbler about the x-axis where material flows in the layer in the z direction.

A *rotation* is a reorientation of the tumbler with respect to the axes (x, y, z) that does not result in flow. Viewing the tumbler from the top, **R** is one-quarter rotation about the y-axis in the clockwise direction. Thus, a point in the tumbler initially located at coordinate position (x, y, z) is relocated to position $(-z, y, x)$ upon action **R**.

A *reflection* is a transformation about some plane in three dimensions (or line in two dimensions). The reflection about the $z=0$ plane, $\mathbf{S}_{z=0}$, for a point (x, y, z) reflects that point to $(x, y, -z)$. The subscript on **S** simply labels the symmetry for bookkeeping. When a superscript is attached, this superscript is the number of times that the action, reflection or rotation is applied. For example, two applications of the reflection about the $z=0$ plane is expressed since $\mathbf{S}_{z=0}^2$. As $\mathbf{S}_{z=0}^2 = 1$, this is referred to as an *involution*.

A2. *Application example*

The two-axis protocol, shown in figure 27 for a spherical tumbler and figure B1 for a cubical tumbler, can be represented by successive applications of the action $\mathbf{M} = \mathbf{WU}$. The key to uncovering symmetries is to unravel the relationship between **U** and **W**. The treatment here follows that of Franjione and Ottino [191]. The flows due to **U** and **W** are rotationally symmetric to each other with rotations of $\pm\pi/2$ radians about the y-axis for both the spherical tumbler and the cubical tumbler. Thus, the result achieved by action **W** can be achieved by a counterclockwise rotation ($\mathbf{R}^{-1}$), followed by action **U**, followed by a clockwise rotation **R**. In terms of map algebra,

$$\mathbf{W} = \mathbf{RUR}^{-1}. \tag{A1}$$

Here **U** and **W** are also related to their inverses by means of a different rotational symmetry (a rotation of π radians), $\mathbf{R}^2$, about the y-axis. In the case of **U**, this is

$$\mathbf{U} = \mathbf{R}^2\mathbf{U}^{-1}\mathbf{R}^2. \tag{A2}$$

Thus, action **U** can be achieved by rotating the tumbler clockwise π radians about the y-axis, applying **U** in the reverse direction and then rotating the tumbler again clockwise π radians back to its original configuration.

Both actions **U** and **W** also have reflectional symmetry. Action **U** is symmetric to itself with respect to reflections across the $z=0$ plane. This symmetry can be expressed as

$$\mathbf{U} = \mathbf{S}_{z=0}\mathbf{U}\mathbf{S}_{z=0}. \tag{A3}$$

Here **W** has a similar reflectional symmetry across the $x=0$ plane.

The above relationships give insight into the overall map, **M**. Inserting the rotational symmetry given by equation (A1) into $\mathbf{M} = \mathbf{WU}$, gives

$$\mathbf{M} = \mathbf{RUR}^{-1}\mathbf{U}. \tag{A4}$$

Then using the reflectional symmetry from equation (A3) results in

$$\mathbf{M} = \mathbf{R}\mathbf{S}_{z=0}\mathbf{U}\mathbf{S}_{z=0}\mathbf{R}^{-1}\mathbf{U}. \tag{A5}$$

Now consider the meaning of the transformations $\mathbf{R}\mathbf{S}_{z=0}$ and $\mathbf{S}_{z=0}\mathbf{R}^{-1}$ by taking the point located at (x, y, z):

$$(x, y, z) \xrightarrow{\mathbf{S}_{z=0}} (x, y, -z) \xrightarrow{\mathbf{R}} (z, y, x)$$

and

$$(x, y, z) \xrightarrow{\mathbf{R}^{-1}} (z, y, -x) \xrightarrow{\mathbf{S}_{z=0}} (z, y, x).$$

Thus, $\mathbf{R}\mathbf{S}_{z=0} = \mathbf{S}_{z=0}\mathbf{R}^{-1}$. This suggests a new symmetry,

$$\mathbf{S}_1 = \mathbf{R}\mathbf{S}_{z=0} = \mathbf{S}_{z=0}\mathbf{R}^{-1}. \tag{A6}$$

Since $\mathbf{S}_1$ is the transformation $(x, y, z) \rightarrow (z, y, x)$, it represents a symmetry across the $x = z$ plane. Equation (A5) can now be expressed as

$$\mathbf{M} = \mathbf{S}_1\mathbf{U}\mathbf{S}_1\mathbf{U}. \tag{A7}$$

Thus, the overall map, $\mathbf{M}$, is the second iteration of a fundamental map ($\mathbf{M} = \mathbf{M}_\mathrm{f}^2$), where

$$\mathbf{M}_\mathrm{f} = \mathbf{S}_1\mathbf{U}. \tag{A8}$$

Now inserting equation (A2) into equation (A8):

$$\mathbf{M}_\mathrm{f} = \mathbf{S}_1\mathbf{R}^2\mathbf{U}^{-1}\mathbf{R}^2. \tag{A9}$$

Since $\mathbf{S}_1$ is an involution ($\mathbf{S}_1^2 = 1$), it can be inserted into equation (A9) to get

$$\mathbf{M}_\mathrm{f} = \mathbf{S}_1\mathbf{R}^2[\mathbf{U}^{-1}\mathbf{S}_1]\mathbf{S}_1\mathbf{R}^2. \tag{A10}$$

The term in brackets in equation (A10) is the inverse of the fundamental map, $\mathbf{M}_\mathrm{f}$. Further, $\mathbf{S}_1\mathbf{R}^2$ is a new symmetry:

$$(x, y, z) \xrightarrow{\mathbf{R}^2} (-x, y, -z) \xrightarrow{\mathbf{S}_1} (-z, y, -x).$$

This new symmetry $\mathbf{S}_2$ represents a reflection across the $x = -z$ plane, shown in figure A1. Using $\mathbf{S}_2$, equation (A10) becomes

$$\mathbf{M}_\mathrm{f} = \mathbf{S}_2\mathbf{M}_\mathrm{f}^{-1}\mathbf{S}_2. \tag{A11}$$

Thus, the fundamental map $\mathbf{M}_\mathrm{f}$ is symmetric to its inverse with respect to reflections across the $x = -z$ plane. This is referred to as a *time-reversal symmetry* [191]: $\mathbf{M}_\mathrm{f}^{-1}$ is the inverse of $\mathbf{M}_\mathrm{f}$, which is equivalent to applying the action in reverse (backwards in time). This means that all period-1 points (those that return to their initial position after one iteration of $\mathbf{M} = \mathbf{W}\mathbf{U}$) lie in this plane or in symmetric pairs reflected across it. This is a crucial insight that increases the efficiency of locating periodic points.

A3. *Other symmetries*

The above treatment can be generalized. There are many possibilities of different flows using two axes of rotation that involve protocols other than the repeating iterations of $\mathbf{W}\mathbf{U}$, which, noting the rotational symmetries of $\mathbf{U}$ and $\mathbf{W}$, can be expressed as $\mathbf{R}\mathbf{U}\mathbf{R}^{-1}\mathbf{U}$. In all, it can be shown that there are 16 different protocols that have repeating units $\mathbf{R}^a\mathbf{U}^b\mathbf{R}^c\mathbf{U}^d$, where a, b, c, d can have values of ± 1. Using the symmetries analysis technique, these 16 flows can be separated into two families as shown in figure A2. Further details are provided by Franjione and Ottino [191].

The members of each family are related by rotational and reflectional symmetries. One of these families is the set of flows that all have a fundamental map, $\mathbf{M}_\mathrm{f} = \mathbf{R}\mathbf{S}_{z=0}\mathbf{U}$, which has a time-reversal symmetry about the $x = -z$ plane. This means that the period-1 points in the system will be symmetric with respect to the $x = -z$ plane. The members of the other family all have a different fundamental map, $\mathbf{M}_\mathrm{f} = \mathbf{R}\mathbf{U}$, which has another time-reversal symmetry.

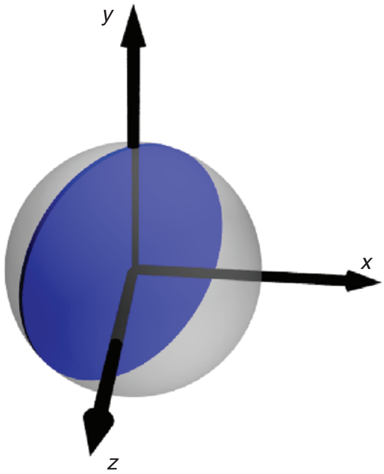

Figure A1. Illustration of the reflectional symmetry $\mathbf{S}_2$ of the fundamental map, $\mathbf{M}_f$, in a spherical tumbler.

Appendix B: Application example with a cubical tumbler

The procedure described for a spherical tumbler in section 6 can be applied to a half-full cubical tumbler rotated by the $\mathbf{M} = \mathbf{WU}$ protocol about axes through its faces, shown in figure B1. In this case, each cross-sectional slice for the flow is a square. The symmetries analysis is independent of tumbler geometry, since the general characteristics of the underlying flow are similar in both the spherical and cubical tumblers.

B1. *Skeleton of 3d flow in a cubical tumbler*

The position of period-1 points for the two-axis cubical tumbler can be found using the same methodology as used for the two-axis spherical tumbler, described in section 6.3. The resulting period-1 points are symmetric about the $x = -z$ plane, as shown in figure B2. The transition along the curve of period-1 points with a 'hyperbolic' character (green) to those with an 'elliptic' character (blue) is continuous, not abrupt. (Here, one period is one iteration of the map, $\mathbf{M}$.) Thus, moving along one of the curves, the transition of the imaginary part of the eigenvalue to zero is gradual. As predicted from the symmetry analysis, the period-1 points are symmetric about the $x = -z$ plane (the two individual points) or lie in the $x = -z$ plane (the five curves).

The two points in figure B2 that form a symmetric pair reflected across from each other across the $x = -z$ plane are related by the time-reversal symmetry. The period-1 point in the negative x, negative z corner in figure B2 has an eigenvalue that is real and greater than one (corresponding to a direction of stretching) and two eigenvalues that are complex conjugates. The other period-1 point has an eigenvalue that is real and less than one (corresponding to a direction of compression) and two

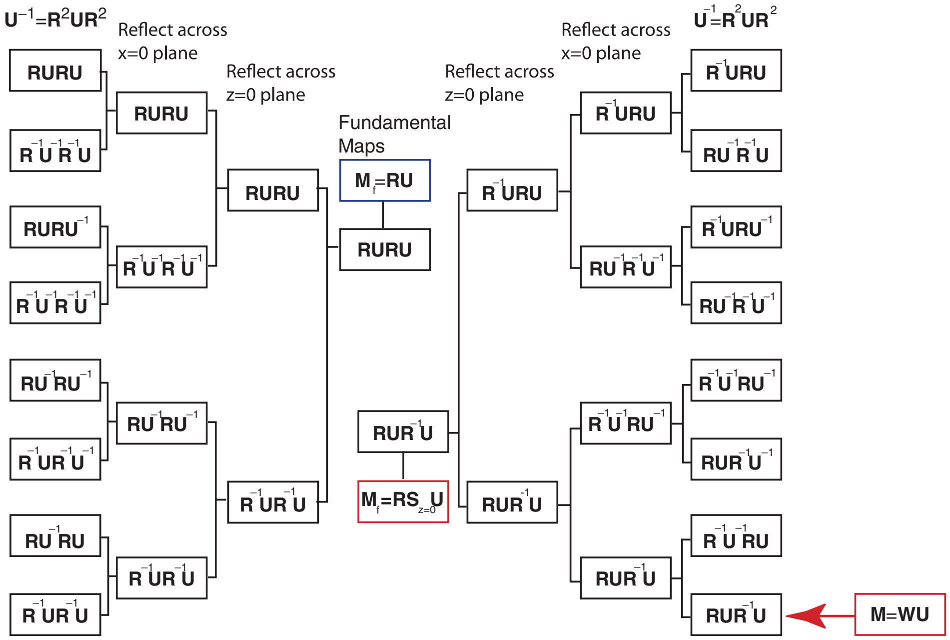

Figure A2. The 16 possible two-axis protocols $\mathbf{R}^a\mathbf{U}^b\mathbf{R}^c\mathbf{U}^d$ (where a, b, c and d can be ±1) can be separated into two families. The family of protocols in the right-most column has the fundamental map $\mathbf{M}_\mathrm{f} = \mathbf{RS}_{z=0}\mathbf{U}$ at the centre of the figure. Note that $\mathbf{M} = \mathbf{WU}$ is in this family, as noted at the bottom of the right-hand side. The family of protocols in the left-most column has the fundamental map $\mathbf{M}_\mathrm{f} = \mathbf{RU}$ noted at the centre of the figure. Labels at the top of each column indicate the symmetry relationship between pairs of protocols in that column that permit a pair of protocols to be represented by a single protocol in the next column towards the centre of the figure. For example, consider the pair of protocols at the top of the right column. The protocol $\mathbf{R}^{-1}\mathbf{URU}$ is identical to the protocol below it, $\mathbf{RU}^{-1}\mathbf{R}^{-1}\mathbf{U}$, by using the $\mathbf{R}^2$ rotational symmetry of $\mathbf{U}$ and $\mathbf{U}^{-1}$, ($\mathbf{U}^{-1} = \mathbf{R}^2\mathbf{UR}^2$). Thus, either one can be represented by $\mathbf{R}^{-1}\mathbf{URU}$ at the top of the second column from the right. This protocol is related to the protocol immediately below it in the second column, $\mathbf{RU}^{-1}\mathbf{R}^{-1}\mathbf{U}^{-1}$, by a reflection across the $x=0$ plane (as indicated at the top of the second column from the right). Continuing on to the third column from the right, these two protocols, $\mathbf{R}^{-1}\mathbf{URU}$ and $\mathbf{RUR}^{-1}\mathbf{U}$, are related by a reflection across the $z=0$ plane. This leads to the fundamental map $\mathbf{M}_\mathrm{f} = \mathbf{RS}_{z=0}\mathbf{U}$, which indicates time-reversal symmetry about the $x = -z$ plane.

eigenvalues that are complex conjugates. If the two-axis protocol were run backwards (first $\mathbf{W}$ backwards followed by $\mathbf{U}$ backwards, $\mathbf{M}^{-1} = \mathbf{U}^{-1}\mathbf{W}^{-1}$), then the stretching and compression characteristics of the two period-1 points for the two-axis protocol would be reversed, consistent with a time-reversal symmetry about the $x = -z$ plane. That is, what happens on one side of the plane of symmetry according to $\mathbf{M} = \mathbf{WU}$ will happen on the other side of the plane of symmetry according to $\mathbf{M}^{-1} = \mathbf{U}^{-1}\mathbf{W}^{-1}$.

The curves of period-1 points in figure B2 are not symmetric with respect to the $x = z$ plane. The only restriction on the location of the period-1 points according to the symmetries analysis is that they be symmetric with respect to the $x = -z$ plane.

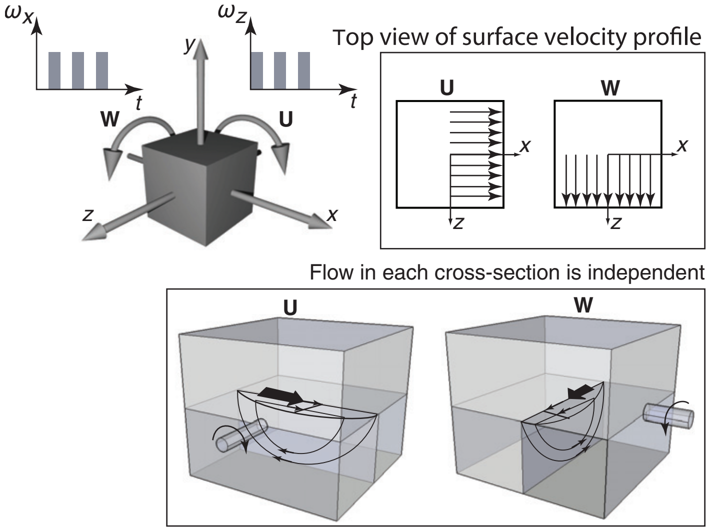

Figure B1. Rotation of a cubical tumbler at its faces on two independent axes of rotation: **U** results in flow in the layer in the positive x direction; **W** results in flow in the layer in the positive z direction. Flow in each cross section orthogonal to the axis of rotation is proportional to cross-sectional geometry.

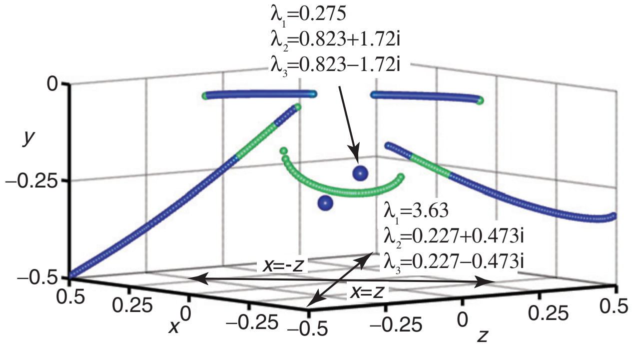

Figure B2. Location of period-1 points for a half-full cubical tumbler with a side length of one rotated by the mapping $\mathbf{M} = \mathbf{WU}$. In the model used to generate these results $\dot{\gamma} = 200|\omega|$. Hyperbolic points are represented by green spheres. Elliptic points are represented by blue spheres. See online version for colour.

By applying the flow protocol **UW** rather than $\mathbf{M} = \mathbf{WU}$, the $x = z$ asymmetry of the curves of points is reflected about the $x = z$ plane. The $x = -z$ symmetry is retained owing to the rotational symmetry relationship between **U** and **W** (equation (A1)). **UW** is equivalent to $\mathbf{URUR}^{-1}$, which is the inverse of $\mathbf{RU}^{-1}\mathbf{R}^{-1}\mathbf{U}^{-1}$ and part of the family of protocols that has a time-reversal symmetry about the $x = -z$ plane in figure A2.

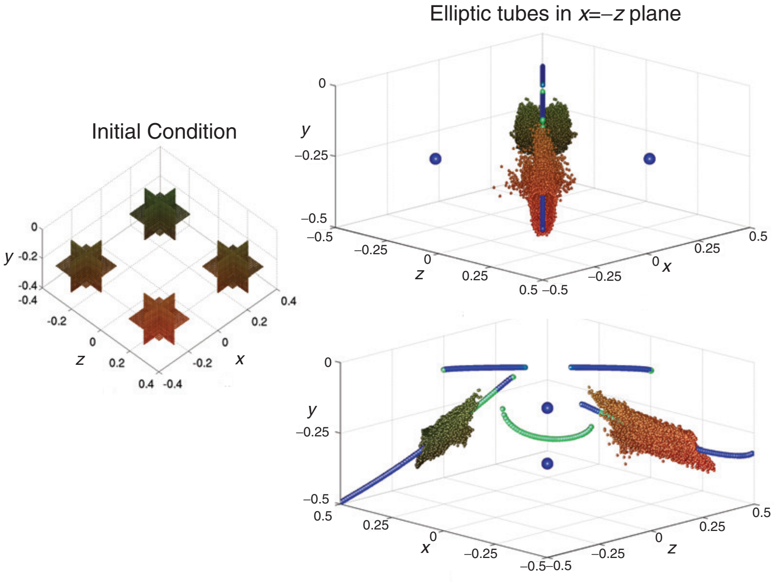

Figure B3. Points trapped in a region near their initial condition are plotted after 20 periods of **M** for the cubical tumbler. Left: Initial condition. Right: Points are trapped near the elliptic portion of the curve of period-1 points, as shown from two viewpoints. In the model used to generate these results $\dot{\gamma} = 200|\omega|$.

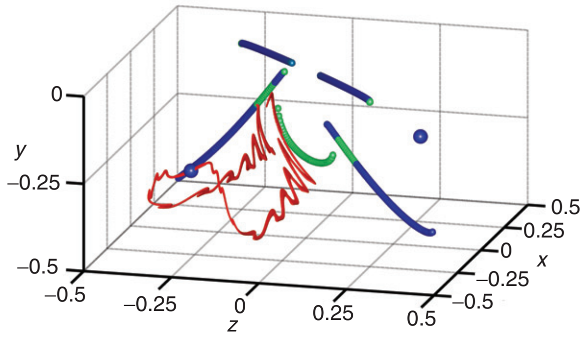

Figure B4. Unstable manifold trace from the period-1 point in the negative x, negative z corner after 12 periods as observed from two different viewpoints. 10^4 points were seeded at the surface of a small sphere of radius $0.01L$ surrounding the period-1 point, where L is half of the side length of the cube. In the model used to generate these results $\dot{\gamma} = 200|\omega|$.

In the case of the cubical tumbler, the visualization technique in figure 31 can be applied, as shown in figure B3. In this case, points that are trapped are isolated in tube-like regions around the elliptic portions of the curves in the $x = -z$ plane. Other points that explore larger regions of the domain of the flow are not shown. Viewing along the $x = -z$ plane in the upper right portion of figure B3, the reflectional symmetry across the $x=-z$ plane is evident. This agrees with the symmetries analysis technique that suggests that period-1 points should lie in the $x=-z$ plane or in pairs reflected across it.

B2. *Unstable manifold tracing*

Visualization of the dynamics of 2d + T flows is relatively straightforward. Elliptic points are surrounded by KAM surfaces, creating invariant regions of flow whereas hyperbolic points have associated stable and unstable manifolds [182]. The 3d + T case is conceptually similar, but visualization and identification of the flow structures is considerably harder. After one period of flow for a cubical tumbler rotated on two axes, a small sphere of points seeded in the flow near one of the isolated period-1 points stretches and deforms to form an ellipsoid. After three periods, points begin to curve away from the elliptic point and stretch in the $x=z$ direction. After just 12 periods of flow, the stretching and folding leads to the typical unstable manifold pile-up as it approaches the stable manifolds of the curve of period-1 points in the $x=-z$ plane, as shown in figure B4.

Over 20 periods of flow, the series of points quickly lose connectivity, an unavoidable situation in chaotic flows [219]. However, they trace out a pattern in the phase space that corresponds to the shape of the segregation pattern suggested in figure 34, as shown in figure 35. While the period-1 points are symmetric with respect to the $x=-z$ plane as predicted by the time-reversal symmetry of $\mathbf{M}_\mathrm{f}$, the unstable manifold trace travels from the isolated period-1 point in the negative x negative z corner towards the curve of period-1 points in the $x=z$ direction. As it continues, the unstable manifold traces out the boundary where segregated particles are found in the bed including all three lobes that are evident in the segregation pattern of figure 34. This is similar to the result observed for unstable manifold tracing in 2d + T flows [182] shown in figure 21(d).

References

[1] So much more to know. Science **309** 78 (2005).
[2] M.F. Gerstell, O. Aharonson and N. Schorghofer, Icarus **168** 122 (2004).
[3] A.H. Treiman, J. Geophys. Res. **108** 8031 (2003).
[4] T. Shinbrot, N.H. Duong, L. Kwan and M.M. Alvarez, Proc. Natl. Acad. Sci. USA **101** 8542 (2004).
[5] P.M. Schenk and M.H. Bulmer, Science **279** 1514 (1998).
[6] M.S. Robinson, P.C. Thomas, J. Veverka, S. Murchie and B. Carcich, Nature **413** 396 (2001).
[7] R.M. Iverson, Rev. Geophys. **35** 245 (1997).
[8] B.J. Ennis, J. Green and R. Davies, Chem. Eng. Prog. **90** 32 (1994).
[9] J.M. Ottino, Chem. Eng. Sci. **61** 4165 (2006).
[10] H.M. Jaeger, S.R. Nagel and R.P. Behringer, Phys. Today **49** 32 (1996).
[11] H.M. Jaeger, S.R. Nagel and R.P. Behringer, Rev. Mod. Phys. **68** 1259 (1996).
[12] L.P. Kadanoff, Rev. Mod. Phys. **71** 435 (1999).
[13] I.S. Aranson and L.S. Tsimring, Rev. Mod. Phys. **78** 641 (2006).
[14] J.M. Ottino and T. Shinbrot, Comparing extremes: mixing of fluids, mixing of solids, in *NATO Advanced Study Institute on Mixing: Chaos and Turbulence*, edited by H. Chaté, E. Villermaux and J.-M. Chomaz (Luwer Academic/Plenum, Cargèse, France, 1999), pp. 163.

[15] J.A. Drahun and J. Bridgwater, Powder Technol. **36** 39 (1983).
[16] A. Rosato, K.J. Strandburg, F. Prinz and R.H. Swendsen, Phys. Rev. Lett. **58** 1038 (1987).
[17] J.B. Knight, H.M. Jaeger and S.R. Nagel, Phys. Rev. Lett. **70** 3728 (1993).
[18] D.V. Khakhar, J.J. McCarthy and J.M. Ottino, Phys. Fluids **9** 3600 (1997).
[19] K.M. Hill, D.V. Khakhar, J.F. Gilchrist, J.J. McCarthy and J.M. Ottino, Proc. Natl. Acad. Sci. USA **96** 11701 (1999).
[20] J. Duran, *Sands, Powders, and Grains: An Introduction to the Physics of Granular Materials*, Partially Ordered Systems (Springer, New York, 2000).
[21] J.M. Ottino and D.V. Khakhar, Annu. Rev. Fluid Mech. **32** 55 (2000).
[22] G.H. Ristow, *Pattern Formation in Granular Materials*, Springer Tracts in Modern Physics, Vol. 164 (Springer, Berlin, 2000).
[23] M.E. Mobius, B.E. Lauderdale, S.R. Nagel and H.M. Jaeger, Nature **414** 270 (2001).
[24] A.P.J. Breu, H.M. Ensner, C.A. Kruelle and I. Rehberg, Phys. Rev. Lett. **90** 014302 (2003).
[25] L. Trujillo, M. Alam and H.J. Herrmann, Europhys. Lett. **64** 190 (2003).
[26] L. Trujillo and H.J. Herrmann, Granul. Matter **5** 85 (2003).
[27] L. Trujillo and H.J. Herrmann, Physica A **330** 519 (2003).
[28] T. Shinbrot and F.J. Muzzio, Phys. Rev. Lett. **81** 4365 (1998).
[29] T. Shinbrot, Nature **429** 352 (2004).
[30] D. Helbing, Rev. Mod. Phys. **73** 1067 (2001).
[31] S.B. Savage, Adv. Appl. Mech. **24** 289 (1984).
[32] S. Herminghaus, Adv. Phys. **54** 221 (2005).
[33] R. Jackson, Some mathematical and physical aspects of continuum models for the motion of granular materials, in *Theory of Dispersed Multiphase Flow*, edited by R. Meyer (Academic Press, New York, 1983), pp. 291.
[34] C.H. Rycroft, G.S. Grest, J.W. Landry and M.Z. Bazant, Phys. Rev. E **74** 021306 (2006).
[35] H.A. Janssen, Z. Ver. Dtsch. Ing. **39** 1045 (1895).
[36] M. Sperl, Granul. Matter **8** 59 (2006).
[37] C.S. Campbell, Powder Technol. **162** 208 (2006).
[38] C.S. Campbell, Annu. Rev. Fluid Mech. **22** 57 (1990).
[39] I. Goldhirsch, Annu. Rev. Fluid Mech. **35** 267 (2003).
[40] G.K. Batchelor, *An Introduction to Fluid Dynamics*, 1st Cambridge Mathematical Library edition (Cambridge University Press, Cambridge, 2000).
[41] L.D. Landau and E.M. Lifshitz, *Fluid Mechanics*, 2nd edition (Pergamon Press, Oxford, 1987).
[42] W.M. Deen, *Analysis of Transport Phenomena* (Oxford University Press, New York, 1998).
[43] J. Gollub, Phys. Today **56** 10 (2003).
[44] P.K. Haff, J. Fluid Mech. **134** 401 (1983).
[45] J.T. Jenkins, Rapid flows of granular materials, in *Non-classical Continuum Mechanics*, edited by R.J. Knops and A.A. Lacey, London Mathematical Society Lecture Note Series (Cambridge University Press, Cambridge, 1987), pp. 213.
[46] S. Ogawa, Multitemperature theory of granular materials, in *Proceedings of the U.S.–Japan Seminar on Continuum-Mechanical and Statistical Approaches in the Mechanics of Granular Materials*, edited by S.C. Cowin and M. Satake (Gakujutsu Bunken Fukyukai, Tokyo, Japan, 1978), pp. 208.
[47] S.B. Savage, Granular flows at high shear rates, in *Theory of Dispersed Multiphase Flow*, edited by R. Meyer (Academic Press, New York, 1982), pp. 339.
[48] R.A. Bagnold, Proc. R. Soc. London, Ser. A **225** 49 (1954).
[49] M.L. Hunt, R. Zenit, C.S. Campbell and C.E. Brennen, J. Fluid Mech. **452** 1 (2002).
[50] P.C. Johnson and R. Jackson, J. Fluid Mech. **176** 67 (1987).
[51] P. Jop, Y. Forterre and O. Pouliquen, Nature **441** 727 (2006).
[52] P. Mills, D. Loggia and M. Tixier, Europhys. Lett. **45** 733 (1999).
[53] L. Bocquet, W. Losert, D. Schalk, T.C. Lubensky and J.P. Gollub, Phys. Rev. E **65** 011307 (2002).

[54] W. Losert, L. Bocquet, T.C. Lubensky and J.P. Gollub, Phys. Rev. Lett. **85** 1428 (2000).
[55] P. Jop, Y. Forterre and O. Pouliquen, J. Fluid Mech. **541** 167 (2005).
[56] J.P. Bouchaud, M.E. Cates, J.R. Prakash and S.F. Edwards, J. Phys. I **4** 1383 (1994).
[57] J.P. Bouchaud, M.E. Cates, J.R. Prakash and S.F. Edwards, Phys. Rev. Lett. **74** 1982 (1995).
[58] T. Boutreux and E. Raphaël, Phys. Rev. E **58** 7645 (1998).
[59] T. Boutreux, E. Raphaël and P.G. de Gennes, Phys. Rev. E **58** 4692 (1998).
[60] I.S. Aranson and L.S. Tsimring, Phys. Rev. E **64** 020301 (2001).
[61] I.S. Aranson and L.S. Tsimring, Phys. Rev. E **65** 061303 (2002).
[62] D. Volfson, L.S. Tsimring and I.S. Aranson, Phys. Rev. E **68** 021301 (2003).
[63] D. Volfson, L.S. Tsimring and I.S. Aranson, Phys. Rev. Lett. **90** 254301 (2003).
[64] T.S. Komatsu, S. Inagaki, N. Nakagawa and S. Nasuno, Phys. Rev. Lett. **86** 1757 (2001).
[65] B.A. Socie, P. Umbanhowar, R.M. Lueptow, N. Jain and J.M. Ottino, Phys. Rev. E **71** 031304 (2005).
[66] N. Jain, J.M. Ottino and R.M. Lueptow, Phys. Rev. E **71** 051301 (2005).
[67] N. Jain, J.M. Ottino and R.M. Lueptow, Granul. Matter **7** 69 (2005).
[68] W.B. Russel, D.A. Saville and W.R. Schowalter, *Colloidal Dispersions*, Cambridge Monographs on Mechanics and Applied Mathematics (Cambridge University Press, Cambridge, 1989).
[69] J. Rajchenbach, Adv. Phys. **49** 229 (2000).
[70] P. Coussot and C. Ancey, Phys. Rev. E **59** 4445 (1999).
[71] N. Jain, J.M. Ottino and R.M. Lueptow, J. Fluid Mech. **508** 23 (2004).
[72] N. Mitarai and F. Nori, Adv. Phys. **55** 1 (2006).
[73] H.M. Li and J.J. McCarthy, Phys. Rev. Lett. **90** 184301 (2003).
[74] H.M. Li and J.J. McCarthy, Phys. Rev. E **71** 021305 (2005).
[75] A. Castellanos, Adv. Phys. **54** 263 (2005).
[76] N. Jain, D.V. Khakhar, R.M. Lueptow and J.M. Ottino, Phys. Rev. Lett. **86** 3771 (2001).
[77] M. Nakagawa, S.A. Altobelli, A. Caprihan, E. Fukushima and E.K. Jeong, Exp. Fluids **16** 54 (1993).
[78] G. Metcalfe and M. Shattuck, Physica A **233** 709 (1996).
[79] K.M. Hill, A. Caprihan and J. Kakalios, Phys. Rev. Lett. **78** 50 (1997).
[80] E. Fukushima, Annu. Rev. Fluid Mech. **31** 95 (1999).
[81] J.E. Maneval, K.M. Hill, B.E. Smith, A. Caprihan and E. Fukushima, Granul. Matter **7** 199 (2005).
[82] L.B. Wang, J.D. Frost and J.S. Lai, J. Comput. Civil Eng. **18** 28 (2004).
[83] G.D.R. MiDi, Eur. Phys. J. E **14** 341 (2004).
[84] F. Cantelaube and D. Bideau, Europhys. Lett. **30** 133 (1995).
[85] E. Clément, J. Rajchenbach and J. Duran, Europhys. Lett. **30** 7 (1995).
[86] D.V. Khakhar, J.J. McCarthy, T. Shinbrot and J.M. Ottino, Phys. Fluids **9** 31 (1997).
[87] K.M. Hill, J.F. Gilchrist, J.M. Ottino, D.V. Khakhar and J.J. McCarthy, Int. J. Bifurcat. Chaos **9** 1467 (1999).
[88] D.V. Khakhar, J.J. McCarthy, J.F. Gilchrist and J.M. Ottino, Chaos **9** 195 (1999).
[89] K.M. Hill, N. Jain and J.M. Ottino, Phys. Rev. E **64** 011302 (2001).
[90] D.V. Khakhar, A.V. Orpe and J.M. Ottino, Advances in Complex Systems **4** 407 (2001).
[91] A.V. Orpe and D.V. Khakhar, Phys. Rev. E **64** 031302 (2001).
[92] K.M. Hill, G. Gioia and V.V. Tota, Phys. Rev. Lett. **91** 064302 (2003).
[93] J. Rajchenbach, Phys. Rev. Lett. **65** 2221 (1990).
[94] N.A. Pohlman, J.M. Ottino and R.M. Lueptow, Phys. Rev. E **74** 031305 (2006).
[95] H. Henein, J.K. Brimacombe and A.P. Watkinson, Metall. Trans. B **14B** 191 (1983).
[96] J. Mellmann, Powder Technol. **118** 251 (2001).
[97] A. Brucks, T. Arndt, J.M. Ottino and R.M. Lueptow, Phys. Rev. E **75** 032301 (2007) under consideration.
[98] J.J. McCarthy, T. Shinbrot, G. Metcalfe, J.E. Wolf and J.M. Ottino, AIChE Journal **42** 3351 (1996).
[99] G. Metcalfe, T. Shinbrot, J.J. McCarthy and J.M. Ottino, Nature **374** 39 (1995).

[100] D. Désérable, SIAM J. Appl. Math. **62** 1414 (2002).
[101] D.V. Ktitarev and D.E. Wolf, Comput. Phys. Commun. **121** 303 (1999).
[102] P.Y. Lai, L.C. Jia and C.K. Chan, Phys. Rev. Lett. **79** 4994 (1997).
[103] H.A. Makse, P. Cizeau and H.E. Stanley, Phys. Rev. Lett. **78** 3298 (1997).
[104] H.A. Makse, S. Havlin, P.R. King and H.E. Stanley, Nature **386** 379 (1997).
[105] S.E. Cisar, R.M. Lueptow and J.M. Ottino, AIChE Journal **53** 1151 (2007).
[106] N.A. Pohlman, B.L. Severson, J.M. Ottino and R.M. Lueptow, Phys. Rev. E **73** 031304 (2006).
[107] C.M. Dury, G.H. Ristow, J.L. Moss and M. Nakagawa, Phys. Rev. E **57** 4491 (1998).
[108] K. Yamane, M. Nakagawa, S.A. Altobelli, T. Tanaka and Y. Tsuji, Phys. Fluids **10** 1419 (1998).
[109] R. Khosropour, E. Valachovic and B. Lincoln, Phys. Rev. E **62** 807 (2000).
[110] S.P. Klein and B.R. White, AIAA J. **28** 1701 (1990).
[111] S.E. Cisar, P.B. Umbanhowar and J.M. Ottino, Phys. Rev. E **74** 051305 (2006).
[112] J.F. Gilchrist, Geometric aspects of mixing and segregation in granular tumblers. PhD Thesis, Northwestern University (2003).
[113] S.B. Savage and C.K.K. Lun, J. Fluid Mech. **189** 311 (1988).
[114] N. Nityanand, B. Manley and H. Henein, Metall. Trans. B **17B** 247 (1986).
[115] V.N. Dolgunin and A.A. Ukolov, Powder Technol. **83** 95 (1995).
[116] V.N. Dolgunin, A.N. Kudy and A.A. Ukolov, Powder Technol. **96** 211 (1998).
[117] J.M.N.T. Gray and K. Hutter, Continuum Mech. Therm. **9** 341 (1997).
[118] A.R. Thornton, J.M.N.T. Gray and A.J. Hogg, J. Fluid Mech. **550** 1 (2006).
[119] D.V. Khakhar, A.V. Orpe and S.K. Hajra, Physica A **318** 129 (2003).
[120] N. Thomas, Phys. Rev. E **62** 961 (2000).
[121] J.M.N.T. Gray, M. Shearer and A.R. Thornton, Proc. R. Soc. A **462** 947 (2006).
[122] J.C. Williams, Powder Technol. **15** 245 (1976).
[123] D.C. Hong, P.V. Quinn and S. Luding, Phys. Rev. Lett. **86** 3423 (2001).
[124] J.A. Both and D.C. Hong, Phys. Rev. Lett. **88** 124301 (2002).
[125] D.V. Khakhar, A.V. Orpe and J.M. Ottino, Powder Technol. **116** 232 (2001).
[126] K.M. Hill, G. Gioia and D. Amaravadi, Phys. Rev. Lett. **93** 224301 (2004).
[127] K.M. Hill, G. Gioia, D. Amaravadi and C. Winter, Complexity **10** 79 (2005).
[128] I. Zuriguel, J.M.N.T. Gray, J. Peixinho and T. Mullin, Phys. Rev. E **73** 061302 (2006).
[129] H.A. Makse, R.C. Ball, H.E. Stanley and S. Warr, Phys. Rev. E **58** 3357 (1998).
[130] M. Alonso, M. Satoh and K. Miyanami, Powder Technol. **68** 145 (1991).
[131] S.K. Hajra and D.V. Khakhar, Phys. Rev. E **69** 031304 (2004).
[132] Y. Oyama, Scientific papers of the I.P.C.R. **37** 17 (1939).
[133] M.B. Donald and B. Roseman, British Chemical Engineering **7** 749 (1962).
[134] J. Bridgwater, N.W. Sharpe and D.C. Stocker, Trans. Inst. Chem. Eng. **47** T114 (1969).
[135] S. Dasgupta, D.V. Khakhar and S.K. Bhatia, Chem. Eng. Sci. **46** 1513 (1991).
[136] K.M. Hill and J. Kakalios, Phys. Rev. E **49** R3610 (1994).
[137] T. Elperin and A. Vikhansky, Phys. Rev. E **60** 1946 (1999).
[138] A. Alexander, F.J. Muzzio and T. Shinbrot, Granul. Matter **5** 171 (2004).
[139] O. Zik, D. Levine, S.G. Lipson, S. Shtrikman and J. Stavans, Phys. Rev. Lett. **73** 644 (1994).
[140] K.M. Hill, A. Caprihan and J. Kakalios, Phys. Rev. E **56** 4386 (1997).
[141] K. Choo, T.C.A. Molteno and S.W. Morris, Phys. Rev. Lett. **79** 2975 (1997).
[142] S.J. Fiedor and J.M. Ottino, Phys. Rev. Lett. **91** 244301 (2003).
[143] T. Arndt, T. Siegmann-Hegerfeld, S.J. Fiedor, J.M. Ottino and R.M. Lueptow, Phys. Rev. E **71** 011306 (2005).
[144] I.S. Aranson and L.S. Tsimring, Phys. Rev. Lett. **82** 4643 (1999).
[145] I.S. Aranson, L.S. Tsimring and V.M. Vinokur, Phys. Rev. E **60** 1975 (1999).
[146] N. Taberlet, M. Newey, P. Richard and W. Losert, J. Stat. Mech.-Theory E. P07013 (2006).
[147] J.F. Gilchrist and J.M. Ottino, Phys. Rev. E **68** 061303 (2003).
[148] C. Wightman, M. Moakher, F.J. Muzzio and O. Walton, AIChE Journal **44** 1266 (1998).

[149] C. Wightman, P.R. Mort, F.J. Muzzio, R.E. Riman and E.K. Gleason, Powder Technol. **84** 231 (1995).

[150] C. Wightman and F.J. Muzzio, Powder Technol. **98** 113 (1998).

[151] C. Wightman and F.J. Muzzio, Powder Technol. **98** 125 (1998).

[152] T. Elperin and A. Vikhansky, Europhys. Lett. **42** 619 (1998).

[153] H.A. Makse, Phys. Rev. Lett. **83** 3186 (1999).

[154] J.J. McCarthy, D.V. Khakhar and J.M. Ottino, Powder Technol. **109** 72 (2000).

[155] P. Bak, C. Tang and K. Wiesenfeld, Phys. Rev. Lett. **59** 381 (1987).

[156] D.V. Ktitarev and D.E. Wolf, Granul. Matter **1** 141 (1998).

[157] T. Yanagita, Phys. Rev. Lett. **82** 3488 (1999).

[158] T. Shinbrot, M. Zeggio and F.J. Muzzio, Powder Technol. **116** 224 (2001).

[159] C.M. Dury and G.H. Ristow, J. Phys. I **7** 737 (1997).

[160] C.M. Dury and G.H. Ristow, Phys. Fluids **11** 1387 (1999).

[161] J.J. McCarthy and J.M. Ottino, Powder Technol. **97** 91 (1998).

[162] G.H. Ristow, Europhys. Lett. **28** 97 (1994).

[163] C.M. Dury and G.H. Ristow, Europhys. Lett. **48** 60 (1999).

[164] D.C. Rapaport, Phys. Rev. E **65** 061306 (2002).

[165] S. Shoichi, Mod. Phys. Lett. B **12** 115 (1998).

[166] N. Taberlet, W. Losert and P. Richard, Europhys. Lett. **68** 522 (2004).

[167] K. Yamane, J. Mater. Res. **19** 623 (2004).

[168] F. Bertrand, L.A. Leclaire and G. Levecque, Chem. Eng. Sci. **60** 2517 (2005).

[169] M. Moakher, T. Shinbrot and F.J. Muzzio, Powder Technol. **109** 58 (2000).

[170] T. Shinbrot, A. Alexander, M. Moakher and F.J. Muzzio, Chaos **9** 611 (1999).

[171] O.S. Sudah, P.E. Arratia, A. Alexander and F.J. Muzzio, AIChE Journal **51** 836 (2005).

[172] S. Plimpton, J. Comput. Phys. **117** 1 (1995).

[173] A.V. Orpe and D.V. Khakhar, Phys. Rev. Lett. **93** 068001 (2004).

[174] N. Jain, J.M. Ottino and R.M. Lueptow, Phys. Fluids **14** 572 (2002).

[175] N.A. Pohlman, S.W. Meier, R.M. Lueptow and J.M. Ottino, J. Fluid Mech. **560** 355 (2006).

[176] A. Alexander, T. Shinbrot and F.J. Muzzio, Powder Technol. **126** 174 (2002).

[177] D. Bonamy, F. Daviaud and L. Laurent, Phys. Fluids **14** 1666 (2002).

[178] J. Rajchenbach, Phys. Rev. Lett. **90** 144302 (2003).

[179] D.V. Khakhar, A.V. Orpe, P. Andresén and J.M. Ottino, J. Fluid Mech. **441** 255 (2001).

[180] S. Douady, B. Andreotti and A. Daerr, Eur. Phys. J. B **11** 131 (1999).

[181] J.M. Ottino, *The Kinematics of Mixing: Stretching, Chaos, and Transport*, Cambridge Texts in Applied Mathematics (Cambridge University Press, Cambridge, 1989).

[182] S.W. Meier, S.E. Cisar, R.M. Lueptow and J.M. Ottino, Phys. Rev. E **74** 031310 (2006).

[183] M.A. Armstrong, *Basic Topology* (McGraw-Hill, London, 1979).

[184] R. Brown, *Topology: A Geometric Account of General Topology, Homotopy Types, and the Fundamental Groupoid*, edited by E. Horwood, revised, updated and expanded edition (Halsted Press, Chichester, 1988).

[185] J.M. Ottino, Phys. Fluids A—Fluid **3** 1417 (1991).

[186] V.I. Arnold, Russ. Math. Surv. **18** 85 (1963).

[187] A.N. Kolmogorov, The general theory of dynamical systems and classical mechanics, in *1954 Congress in Mathematics* (North-Holland, Amsterdam, 1954), pp. 315. (Translated as Appendix in R.H. Abraham and J.E. Marsden, *Foundations of Mechanics* (Benjamin Cummings, Reading, MA, 1978), pp. 741.)

[188] A.N. Kolmogorov, Dokl. Akad. Nauk SSSR **98** 527 (1954).

[189] R.C. Hilborn, *Chaos and Nonlinear Dynamics: An Introduction for Scientists and Engineers*, 2nd edition (Oxford University Press, Oxford, 2000).

[190] A.J. Lichtenberg and M.A. Lieberman, *Regular and Chaotic Dynamics*, 2nd edn, Applied Mathematical Sciences, Vol. 38 (Springer, New York, 1992).

[191] J.G. Franjione and J.M. Ottino, Phil. Trans. Roy. Soc. Lond. Math. Phys. Sci. **338** 301 (1992).

[192] S.J. Fiedor and J.M. Ottino, J. Fluid Mech. **533** 223 (2005).

[193] P.D. Swanson and J.M. Ottino, J. Fluid Mech. **213** 227 (1990).

[194] S.S. Hsiau and M.L. Hunt, Acta Mech. **114** 121 (1996).

[195] D.V. Khakhar, J.J. McCarthy and J.M. Ottino, Chaos **9** 594 (1999).

[196] M.L. de Haro, E.G.D. Cohen and J.M. Kincaid, J. Chem. Phys. **78** 2746 (1983).

[197] J.T. Jenkins and F. Mancini, Phys. Fluids A—Fluid **1** 2050 (1989).

[198] S.B. Savage, Disorder, diffusion and structure formation in granular flow, in *Disorder and Granular Media*, edited by D. Bideau and A. Hansen (Elsevier Science, Amsterdam, 1993), pp. 255.

[199] S.K. Hajra and D.V. Khakhar, Phys. Fluids **17** 013101 (2005).

[200] T. Elperin and A. Vikhansky, Phys. Rev. E **62** 4446 (2000).

[201] T. Elperin and A. Vikhansky, Physica A **303** 48 (2002).

[202] S.J. Fiedor, P. Umbanhowar and J.M. Ottino, Phys. Rev. E **73** 041303 (2006).

[203] R.S. MacKay, J. Nonlinear Sci. **4** 329 (1994).

[204] G.O. Fountain, D.V. Khakhar, I. Mezić and J.M. Ottino, J. Fluid Mech. **417** 265 (2000).

[205] G.O. Fountain, D.V. Khakhar and J.M. Ottino, Science **281** 683 (1998).

[206] O.S. Galaktionov, P.D. Anderson and G.W.M. Peters, Phys. Fluids **12** 469 (2000).

[207] M.W. Hirsch and S. Smale, *Differential Equations, Dynamical Systems, and Linear Algebra* (Academic Press, New York, 1974).

[208] R. Chella and J.M. Ottino, Arch. Ration. Mech. Anal. **90** 15 (1985).

[209] M.S. Chong, A.E. Perry and B.J. Cantwell, Phys. Fluids A **2** 765 (1990).

[210] I. Mezić and S. Wiggins, J. Nonlinear Sci. **4** 157 (1994).

[211] R.H. Abraham and C.D. Shaw, *Dynamics—The Geometry of Behavior*, Visual Mathematics Library, Vismath Books, Vol. 1 (Aerial Press, Santa Cruz, CA, 1982).

[212] T.S. Krasnopolskaya, V.V. Meleshko, G.W.M. Peters and H.E.H. Meijer, Eur. J. Mech. B—Fluid **18** 793 (1999).

[213] S. Wiggins, *Introduction to Applied Nonlinear Dynamical Systems and Chaos*, 2nd edition, Texts in Applied Mathematics, No. 2 (Springer, New York, 2003).

[214] R. Sturman, S.W. Meier, J.M. Ottino and S. Wiggins, Linked twist map formalism in two and three dimensions applied to mixing in tumbled granular flows, submitted.

[215] R. Sturman, J.M. Ottino and S. Wiggins, *The Mathematical Foundations of Mixing: The Linked Twist Map as a Paradigm in Applications: Micro to Macro, Fluids to Solids*, Cambridge Monographs on Applied and Computational Mathematics, No. 22 (Cambridge University Press, Cambridge, 2006).

[216] S. Wiggins, personal communication (2006).

[217] C.W. Leong and J.M. Ottino, J. Fluid Mech. **209** 463 (1989).

[218] S.W. Meier, D.A. Melani Barreiro, J.M. Ottino and R.M. Lueptow, Coarsening of granular segregation patterns in quasi-2d tumblers, submitted.

[219] J.G. Franjione and J.M. Ottino, Phys. Fluids **30** 3641 (1987).